

University of Windsor

Scholarship at UWindor

Electronic Theses and Dissertations

Theses, Dissertations, and Major Papers

1-1-2006

Finite element model of a double-stage helical gear reduction.

Sinisa Draca

University of Windsor

Follow this and additional works at: <https://scholar.uwindsor.ca/etd>

Recommended Citation

Draca, Sinisa, "Finite element model of a double-stage helical gear reduction." (2006). *Electronic Theses and Dissertations*. 7076.

<https://scholar.uwindsor.ca/etd/7076>

This online database contains the full-text of PhD dissertations and Masters' theses of University of Windsor students from 1954 forward. These documents are made available for personal study and research purposes only, in accordance with the Canadian Copyright Act and the Creative Commons license—CC BY-NC-ND (Attribution, Non-Commercial, No Derivative Works). Under this license, works must always be attributed to the copyright holder (original author), cannot be used for any commercial purposes, and may not be altered. Any other use would require the permission of the copyright holder. Students may inquire about withdrawing their dissertation and/or thesis from this database. For additional inquiries, please contact the repository administrator via email (scholarship@uwindsor.ca) or by telephone at 519-253-3000ext. 3208.

FINITE ELEMENT MODEL OF A DOUBLE-STAGE HELICAL GEAR REDUCTION

by
Siniša Drača

A Thesis

Submitted to the Faculty of Graduate Studies and Research
through Mechanical Engineering
in Partial Fulfillment of the Requirements for
the Degree of Master of Applied Science at the
University of Windsor

Windsor, Ontario, Canada

2006

© 2006 Siniša Drača



Library and
Archives Canada

Bibliothèque et
Archives Canada

Published Heritage
Branch

Direction du
Patrimoine de l'édition

395 Wellington Street
Ottawa ON K1A 0N4
Canada

395, rue Wellington
Ottawa ON K1A 0N4
Canada

Your file Votre référence

ISBN: 978-0-494-35937-2

Our file Notre référence

ISBN: 978-0-494-35937-2

NOTICE:

The author has granted a non-exclusive license allowing Library and Archives Canada to reproduce, publish, archive, preserve, conserve, communicate to the public by telecommunication or on the Internet, loan, distribute and sell theses worldwide, for commercial or non-commercial purposes, in microform, paper, electronic and/or any other formats.

The author retains copyright ownership and moral rights in this thesis. Neither the thesis nor substantial extracts from it may be printed or otherwise reproduced without the author's permission.

AVIS:

L'auteur a accordé une licence non exclusive permettant à la Bibliothèque et Archives Canada de reproduire, publier, archiver, sauvegarder, conserver, transmettre au public par télécommunication ou par l'Internet, prêter, distribuer et vendre des thèses partout dans le monde, à des fins commerciales ou autres, sur support microforme, papier, électronique et/ou autres formats.

L'auteur conserve la propriété du droit d'auteur et des droits moraux qui protègent cette thèse. Ni la thèse ni des extraits substantiels de celle-ci ne doivent être imprimés ou autrement reproduits sans son autorisation.

In compliance with the Canadian Privacy Act some supporting forms may have been removed from this thesis.

Conformément à la loi canadienne sur la protection de la vie privée, quelques formulaires secondaires ont été enlevés de cette thèse.

While these forms may be included in the document page count, their removal does not represent any loss of content from the thesis.

Bien que ces formulaires aient inclus dans la pagination, il n'y aura aucun contenu manquant.


Canada

Abstract

The primary goal of this research involves the description and creation of an analytical finite element model of a double-stage helical gear reduction. This model is used to gain additional insight into the vibration generation that results from helical gear meshing action. The model is also used to perform a limited number of parametric studies. The principal results from a 3D ANSYS partial helical gear model are the static transmission error and torsional mesh stiffness. These two outputs are used as the main inputs into a finite element analytical MATLAB model. In MATLAB, the finite element modelling approach is combined with the torsional-translational gear dynamic model to obtain an overall system model. Output shaft angle has negligible effect on the system's dynamic transmission errors and bearing forces (amplitudes and natural frequencies) while the shaft element length, bearing stiffness and gear positioning effects are significant.

To my wife Carmella for all her love and support.

Acknowledgements

I would like to thank Dr. B.P. Minaker and Dr. P.R. Frise for their supervision and support. Special thanks to Dr G.L. Rohrauer.

I would also like to thank my lab colleagues Nathan Nantais, Edward Oh, and Rob Rieveley for their comments and suggestions with respect to my work.

I am grateful to the University of Windsor and AUTO21 for their financial assistance.

Table of Contents

Abstract	iii
Dedication	iv
Acknowledgements	v
List of Tables	viii
List of Figures	ix
List of Abbreviations	xi
Notation	xii
1 Introduction	1
1.1 Motivation	1
1.2 Background	2
1.3 Literature Review	3
1.3.1 Transmission Error	3
1.3.2 Mesh Stiffness	4
1.3.3 Gear Dynamic Models	5
1.3.4 Gear Contact in ANSYS	10
1.4 Thesis and Research Outline	11
2 Contact Model in ANSYS	13
2.1 Contact Problem Overview	13
2.2 ANSYS Contact	13
2.3 ANSYS Contact Model Validation	18
2.4 Helical Gear Pair Contact	26

3 Analytical Finite Element Model	37
3.1 Gearbox Model Layout	37
3.2 Finite Element Shaft Model	39
3.3 Gear Mesh Model	42
3.4 Load Vector	46
3.5 Bearing Model	49
3.6 Overall System Assembly	49
3.6.1 Coordinate Transformation	49
3.6.2 Finite Element Model Assembly Procedure	51
3.7 Solution Methodology	54
3.7.1 Modal Summation	57
4 Results and Discussion	62
4.1 Free Response	65
4.2 Forced Response	70
4.2.1 Benchmark Model Response	71
4.2.2 Output Shaft Angle Effects	73
4.2.3 Shaft Length Effects	76
4.2.4 Bearing Stiffness Effects	80
4.2.5 Gear Pair Relative Position Effects	83
4.3 Discussion	88
5 Conclusions and Future Work	90
5.1 Summary	90
5.2 Conclusions	91
5.3 Future Work	92
References	93
Appendix A Involute Profile and Helix Macro ANSYS Code	96
Appendix B Beam Element Stiffness Matrix	99
Vita Auctoris	101

List of Tables

2.1	Steel cylinder properties	19
2.2	Helical gear properties	27
3.1	Connectivity table	53
4.1	Benchmark model specifications	64
4.2	Gearbox components with equivalent ANSYS elements	65
4.3	First 10 natural frequency results with their mode shapes	67

List of Figures

1.1	Loaded transmission error	4
1.2	SDOF torsional compliant gear tooth model	6
1.3	MDOF gear dynamic model	7
2.1	Contact detection location at GAUSS points	15
2.2	Parallel axis cylinder contact	20
2.3	2D Von Mises ANSYS stress plot for two cylinders	21
2.4	2D ANSYS and theoretical displacements	22
2.5	2D ANSYS and theoretical surface contact pressures	22
2.6	2D ANSYS and theoretical stress distribution along y axis	23
2.7	3D ANSYS cylinder contact model	24
2.8	2D ANSYS, 3D ANSYS, and theoretical displacements	24
2.9	2D ANSYS, 3D ANSYS, and theoretical surface contact pressures	25
2.10	2D ANSYS, 3D ANSYS, and theoretical stress distribution along y axis	25
2.11	Single gear tooth profile nomenclature	28
2.12	3D partial helical gear pair mesh	31
2.13	Transmission error as a function of pinion position	32
2.14	Torsional mesh stiffness as a function of pinion position	33
2.15	Transmission error as a function of pinion position with constant torque	33
2.16	Torsional mesh stiffness as a function of pinion position with constant torque	34
2.17	Spur and helical gear mesh stiffness comparison	35
2.18	Spur and helical gear pair mesh stiffness harmonics	36
2.19	Spur and helical gear pair TE harmonics	36
3.1	Gearbox layout	38
3.2	Finite element representation of the gearbox	39
3.3	3D Beam element	40
3.4	3D helical gear pair model	43

3.5	Shaft position angle definition	48
3.6	Phase angle definition	48
3.7	Local and global coordinate frames	52
3.8	Spring elements	52
4.1	Benchmark gearbox finite element model	63
4.2	3D ANSYS gearbox model	66
4.3	Second mode shape in ANSYS	68
4.4	First four natural frequencies of the torsional model	69
4.5	MATLAB and ANSYS frequency response for gear 1 node	70
4.6	Frequency response at gear 1 node due to multi-mesh excitation	71
4.7	Dynamic transmission errors for the benchmark model	72
4.8	Dynamic forces on bearing 6 for the benchmark model	72
4.9	Output shaft position angle α_{34} definition	73
4.10	Gear pair 1-2 dynamic transmission error for varied output shaft angle . . .	74
4.11	Gear pair 3-4 dynamic transmission error for varied output shaft angle . . .	75
4.12	Radial dynamic force on bearing 6 for varied output shaft angle	75
4.13	Axial dynamic force on bearing 6 for varied output shaft angle.	76
4.14	Gear pair 1-2 dynamic transmission error for varied element length	77
4.15	Gear pair 3-4 dynamic transmission error for varied element length	78
4.16	Radial dynamic force on bearing 6 for varied element length	78
4.17	Axial dynamic force on bearing 6 for varied element length	79
4.18	Gear pair 1-2 dynamic transmission error for varied bearing stiffness coefficient	81
4.19	Gear pair 3-4 dynamic transmission error for varied bearing stiffness coefficient	81
4.20	Radial dynamic force on bearing 6 for varied bearing stiffness coefficient . .	82
4.21	Axial dynamic force on bearing 6 for varied bearing stiffness coefficient . . .	82
4.22	Gearbox model layout	83
4.23	Gear pair 1-2 dynamic transmission error for varied gear pair position . . .	84
4.24	Gear pair 3-4 dynamic transmission error for varied gear pair position . . .	85
4.25	Radial dynamic force on bearing 6 for varied gear pair position	86
4.26	Axial dynamic force on bearing 6 for varied gear pair position	87

List of Abbreviations

Abbreviation	Description
<hr/>	
AGMA	American Gear Manufacturers Association
ANSYS	Analysis of Systems
APDL	ANSYS Parametric Design Language
CAD	Computer Aided Design
CW	Clockwise
CCW	Counterclockwise
DOF	Degrees of Freedom
DTE	Dynamic Transmission Error
FRF	Frequency Response Function
GDM	Gear Dynamic Models
HEV	Hybrid Electric Vehicle
LH	Left Handed
MATLAB	Matrix Laboratory
MDOF	Multi-Degrees of Freedom
RH	Right Handed
SDOF	Single Degree of Freedom
STE	Static Transmission Error
TE	Transmission Error

Notation

The notation throughout this work is used to denote mathematical types. The notations for specific entities are listed below.

Label	Description
A	cross-sectional area
A_{S_x} and A_{S_y}	net shear effective area in x and y directions, respectively
a_d	addendum in transverse plane
b	contact area half-width
$[C]$	damping matrix
d	diameter of a cylinder
d_e	dedendum in transverse plane
\det	determinant of a matrix
diag	a diagonal matrix
E	modulus of elasticity
e	≈ 2.718282
e_{ij}	static gear transmission error of gear pair ij
$\tilde{e}_{(i)(i+1)r}$	r -th harmonic amplitude
F	compressive force
\vec{F} and \vec{f}	force vector in global and local coordinates, respectively
$\vec{F}_{(i)(i+1)}$	extended force vector
G	modulus of rigidity
$[I]$	identity matrix
I_i and I_j	moment of inertia of gears i and j , respectively
I_x and I_y	moment of inertia about x and y axis, respectively

Label	Description
<hr/>	
J	polar moment of inertia
J_i and J_j	polar moment of inertia of gears i and j , respectively
j	imaginary number
$[K]$	stiffness matrix
$[k]$	element stiffness matrix in local coordinates
$[k_b]$	bearing stiffness matrix
$[k_g]$	stiffness matrix of gear pair ij
k_l	lateral stiffness
k_{ij}	mesh stiffness of gear pair ij
$[k_s]$	stiffness matrix of a beam element
k_t	shaft torsional stiffness
k_x, k_y , and k_z	bearing stiffness in x , y , and z directions, respectively
$k_{\theta x}$ and $k_{\theta y}$	bearing stiffness about x and y directions, respectively
l	length of a shaft element
l_c	length of a cylinder
$[M]$	mass matrix
$[M_s]$	modal mass matrix
$[m]$	element mass matrix in local coordinates
$[m_g]$	gear mass matrix
m_i and m_j	mass of gears i and j , respectively
$[m_s]$	mass matrix of a beam element
m_t	transverse module
N	number of gear teeth
N_s	number of shafts
o	cutter offset
$p_{ij}(t)$	relative displacement of gear mesh ij
p_{max}	maximum pressure
Q	addendum modification coefficient
q	total number of degrees of freedom
R	total number of transmission error harmonics
r	transmission error harmonic

Label	Description
r_b	radius of a shaft element
r_{bi} and r_{bj}	base circle radius of gears i and j , respectively
r_h	gear hub radius
r_p	pitch radius
r_t	tip radius of a cutter
r_x and r_y	radius of gyration about x and y axis, respectively
s	mode number
$[T]$	transformation matrix
superscript T	matrix transpose
T_i and T_j	torque applied to gears i and j , respectively
t	time
w	gear face width
\vec{X} and \vec{x}	element displacement vector in global and local coordinates, respectively
$\ddot{\vec{X}}$ and $\ddot{\vec{x}}$	element acceleration vector in global and local coordinates, respectively
\vec{X}_{ab}	element displacement vector
x_a , y_a , and z_a	displacement of node a in x , y , and z directions, respectively
x_b , y_b , and z_b	displacement of node b in x , y , and z directions, respectively
x_i , y_i , and z_i	displacement of gear i in x , y , and z directions, respectively
x_j , y_j , and z_j	displacement of gear j in x , y , and z directions, respectively
\ddot{x}_i , \ddot{y}_i , and \ddot{z}_i	acceleration of gear i in x , y , and z directions, respectively
\ddot{x}_j , \ddot{y}_j , and \ddot{z}_j	acceleration of gear j in x , y , and z directions, respectively
α_{ij}	relative angular position of gear pair ij
β_{ij}	helix angle of gear pair ij
$\Gamma_{(i)(i+1)r}$	r -th harmonic phase angle
γ	phase angle
δ	approach displacement
δ_v	virtual displacement
ϵ	addendum coefficient
ζ_s	modal damping value
η	dedendum coefficient
θ_{xa} , θ_{ya} , and θ_{za}	angular displacement of node a about x , y , and z axis, respectively

Label	Description
$\theta_{xb}, \theta_{yb}, \text{ and } \theta_{zb}$	angular displacement of node b about $x, y, \text{ and } z$ axis, respectively
$\theta_i \text{ and } \theta_j$	angular displacement of gears i and j , respectively
θ_l	angular displacement of a load
θ_{pm}	angular displacement of a prime mover
$\theta_{xi}, \theta_{yi}, \text{ and } \theta_{zi}$	angular displacement of gear i about $x, y, \text{ and } z$ axis, respectively
$\theta_{xj}, \theta_{yj}, \text{ and } \theta_{zj}$	angular displacement of gear j about $x, y, \text{ and } z$ axis, respectively
$\ddot{\theta}_{xi}, \ddot{\theta}_{yi}, \text{ and } \ddot{\theta}_{zi}$	angular acceleration of gear i about $x, y, \text{ and } z$ axis, respectively
$\ddot{\theta}_{xj}, \ddot{\theta}_{yj}, \text{ and } \ddot{\theta}_{zj}$	angular acceleration of gear j about $x, y, \text{ and } z$ axis, respectively
λ	eigenvalue
ν	Poisson's ratio
$\Pi_{(i)(i+1)}$	phase angle difference between the $e_{(i)(i+1)}(t)$ and $e_{12}(t)$
π	≈ 3.141593
ρ	density
ϱ	tip radius coefficient
$\sigma_x, \sigma_y, \text{ and } \sigma_z$	stress in $x, y, \text{ and } z$ directions, respectively
ς	bearing stiffness coefficient
τ	3x3 direction cosine sub-matrix
$[\Phi]$	mass normalized modal matrix
$\vec{\Phi}_s$	modal vector
ϕ_t	transverse pressure angle
ϕ_{ij}	transverse pressure angle of gear pair ij
$\phi_x \text{ and } \phi_y$	shear deformation parameter in x and y directions, respectively
χ	gear tip relief
$[\Psi]$	modal matrix
ψ_{ij}	plane of action angular position of a gear pair ij
$[\Omega]$	receptance matrix
ω	vibrating frequency
$\omega_{(i)(i+1)}$	gear mesh frequency
ω_s	natural frequency associated with $\vec{\Phi}_s$ modal vector
superscript -1	matrix inverse

Chapter 1

Introduction

1.1 Motivation

When given the task of designing a gear reduction, a design engineer's first reference is the American Gear Manufacturers Association (AGMA) manual[1]. There are two fundamental stress equations given in the manual. One is used for bending, and the other for contact stress calculations. If the stresses on gear teeth are the only concern in the gear reduction system, then the AGMA approach is sufficient. However, in addition to low stress requirements, there may also be low noise and vibration requirements. Due to an infinite number of possible gear reduction layouts, simple closed form equations used to determine vibration levels do not exist. There are general guidelines that should be followed when a low level of vibration is desired. Typically, an increase in gear size and contact ratio (the average number of teeth in contact) results in reduced vibration levels. For many years now, researchers have been developing finite element models capable of capturing dynamic behaviour of gearbox systems. A number of models have been experimentally verified, while a portion, mainly new advanced models, still need experimental verification. Despite the fact that a number of models have been developed, the gear dynamic area is still relatively new, and will require more research as the demand for quiet running gear systems increases.

A gearbox model similar to the benchmark gearbox model presented in this thesis was designed to be used in a Hybrid Electric Vehicle (HEV) application. The actual HEV gearbox could not be modelled and analyzed here due to the lack of computing resources, mainly an ANSYS (Analysis of Systems) license restriction. Without loss of generality, a

simplified gearbox system is modelled and analyzed for the purpose of research presented in this thesis.

1.2 Background

Gears, in their simplest arrangements, are used to transmit power between two parallel shafts. It is important for the angular velocity of the two shafts to remain constant during the power transmission. In theory, it is possible to achieve this conjugate action by the use of the involute profiles. The majority of gear tooth profiles are designed as being involute, thus ensuring conjugate action. This profile works in theory, but in practice there are a number of different factors that require gear tooth profile to deviate from the perfect involute. When the gears are in service, they are usually required to transmit load which causes gear teeth to deflect and deviate from the involute. In addition, when a contact between the two mating gear teeth is made, a local deformation at the point of contact occurs. Also, gear manufacturers are not capable of manufacturing a perfect involute profile. The involute profile is derived from the base circle causing the tooth portion below the base circle to be non-involute. To prevent this tooth portion from coming into contact with the tip of the mating tooth, thus causing non-conjugate action, root and tip reliefs are applied to all gear teeth. All of the above factors contribute to the phenomenon called gear Transmission Error (TE).

In simple terms, the TE is the deviation from the constant angular velocity during meshing action of the two mating gears. All of the above mentioned factors contribute to the gear transmission error with varying degrees of influence. A high TE is certain to cause excessive noise and vibration problems. In general, helical gears produce less TE when compared to spur gears due to higher contact ratio of helical gears. Also, the engagement of the helical gear teeth starts as a point and then gradually converts into a line of contact. When the higher contact ratio is combined with the gradual teeth engagement, one can see why the helical gears are the obvious choice when low vibration and noise power transmission is required.

In the past, to manufacture gearboxes with low levels of noise and vibration meant a significant amount of time spent designing, manufacturing and then testing the gearbox systems. With the computing power available today, it is possible to model and analyze gears and gear-trains, during the design phase, thus determining the effects of different gear parameters on the gear TE and gear train dynamics before they are built.

1.3 Literature Review

Two very important terms, TE and mesh stiffness, in gear dynamics are discussed first. Subsection 1.3.3 gives a classification of gear dynamic models, followed by the review of a recently published work in gear dynamics. Next, the ANSYS approach to gear contact is discussed, also by a review of recently published work in that field.

1.3.1 Transmission Error

Transmission error is found to be one of the main vibration sources in the gear mesh. The TE is described as the difference in the actual output gear position and the position it would occupy if the mating gear teeth profiles were perfectly conjugate. It is usually expressed in angular units or as a linear displacement along the line of action. The two equations are

$$e_{ij} = \theta_j - \frac{N_i}{N_j} \theta_i \quad (1.3.1)$$

for angular units, and

$$e_{ij} = r_{bj} \left(\theta_j - \frac{N_i}{N_j} \theta_i \right) \quad (1.3.2)$$

for linear displacement along the line of action, where

e_{ij} = static gear transmission error of gear pair ij ,

θ_i and θ_j = angular displacement of gears i and j , respectively,

N_i and N_j = number of teeth of gears i and j , respectively, and

r_{bj} = base circle radius of gear j .

Figure 1.1 illustrates the loaded TE for a single gear pair. Furthermore, the TE is typically divided into two categories: manufactured TE and loaded TE. Manufactured TE is caused by the manufacturing inaccuracies and usually results in an excessive amount of material

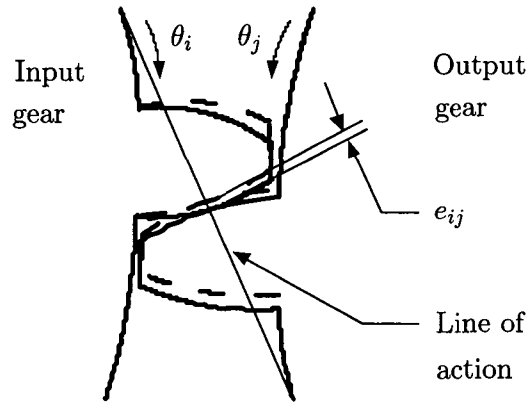


Figure 1.1: *Loaded transmission error.* A solid line represents unloaded conjugate gear teeth, while the dashed line represents loaded gear teeth. θ_i and θ_j are angular displacements of gears i and j , respectively. e_{ij} is the static transmission error of gear pair ij .

on one of the gears in a gear pair. As a result of this, manufactured TE has a positive value. On the other hand, the loaded TE is obtained by applying the load to the gear pair. In this scenario, the changes in tooth deflection are causing the output gear to lag behind the input gear, and the negative value for loaded TE is obtained. The total amount of TE is then the sum of the above two. With intentional tooth modification and precise manufacturing it is possible to introduce a desired amount of manufacturing TE so that the total TE is significantly reduced. This usually works in the case of steady state load systems.

If the TE is measured during static conditions (low shaft speed), it is commonly referred to as the Static Transmission Error (STE). In contrast, if the same measurement is made during dynamic conditions, it is the Dynamic Transmission Error (DTE) that is being measured. Dynamic transmission error is usually larger in magnitude when compared to the STE due to the system's dynamic effects.

1.3.2 Mesh Stiffness

The ratio between the force acting along the line of action and the tooth displacement along the same line is defined as the mesh stiffness. The engaged gear pair mesh stiffness is divided into two main parts: a component due to local Hertzian contact deformation and a component due to the tooth bending deflection. Local contact deflections are small

when compared to those originating from tooth bending deflections. For a single tooth pair in contact, the mesh stiffness remains relatively constant due to the fact that the loss of stiffness in one tooth is compensated by the gain in stiffness of the mating tooth (as the gears rotate the point of contact moves up along a tooth and moves down along the mating tooth).

As the gears rotate, the number of teeth in contact varies, and as a consequence, the effective length of the line of contact is changing, causing variations in mesh stiffness. For low contact ratio spur gears, these variations are largely due to the load transfer occurring over a single tooth and a double tooth pair. In the case of a helical gear pair mesh, the change in total length of line of contact is small due to large contact ratios (usually between two and three) and as a result, mesh stiffness variations are significantly smaller when compared with those of spur gears. As a consequence, a majority of helical Gear Dynamic Models (GDM) treat mesh stiffness as constant and its time averaged value is used. In spur GDM this is not the case, and the Linear Time Variant (LTV) mesh stiffness function is employed.

1.3.3 Gear Dynamic Models

Ozguven and Houser[21] offered a thorough summary of GDM from their early days up to the 1980s. Planetary gear systems were not covered in this review of gear dynamic models. Their findings will be summarized and briefly presented here. The goal of this review is not to refer to a specific model, but to offer general ideas on different types of models that have been developed and implemented. For more detail on a specific model, and its function, one should consult Ozguven and Houser[21]. Gear dynamic models are grouped as follows:

- Simple Dynamic Factor Models

These are the first gear dynamic models developed. The main goal of these models is the determination of the dynamic factor used in the gear stress analysis formulae.

- Models with Tooth Compliance

Tooth elasticity is the only source of energy storage in the system, while the gear blanks, shafts and bearings are assumed to be perfectly rigid. As a consequence, the systems are

usually modelled as Single Degree of Freedom (SDOF) mass-spring systems. In translational models, forced vibration of a gear tooth is studied, while in the torsional models, torsional vibrations of gears in mesh are considered. The transmission error excitation is represented by a relative displacement excitation at the mesh. Figure 1.2 represents an example of a typical SDOF torsional compliant gear tooth model.

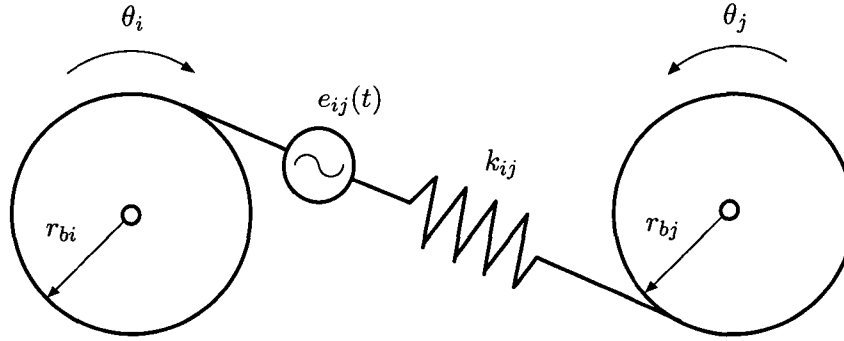


Figure 1.2: (Figure 3 in Ozguven and Houser[21]) *SDOF torsional compliant gear tooth model*. Tooth elasticity is the only energy storage source. Shafts, bearings and gear blanks are assumed to be rigid. TE displacement represents the main excitation to the system. θ_i and θ_j are angular displacements of gears i and j , respectively. r_{bi} and r_{bj} are base circle radii for gears i and j , respectively. e_{ij} is the gear pair ij static gear transmission error, and k_{ij} is the gear pair ij mesh stiffness.

• Models for Gear Dynamics

The above mentioned SDOF models provided results that are in close agreement with experimental studies. However, the close agreement between the model and experimental results was obtained using experimental conditions that closely reflected assumptions made in analytical models. For a majority of real world type gear systems, these assumptions could not be justified; therefore a need for a more general modelling approach emerged. These newly developed Multi Degrees of Freedom (MDOF) models now included shaft and bearing flexibilities, and in some cases housing flexibilities. Some models assumed time invariant mesh stiffness and linear analysis while the others incorporated tooth separation, backlash, and non-linear analysis. A torsional-translational example model of a single stage gear reduction with the prime mover and the load is shown in Figure 1.3.

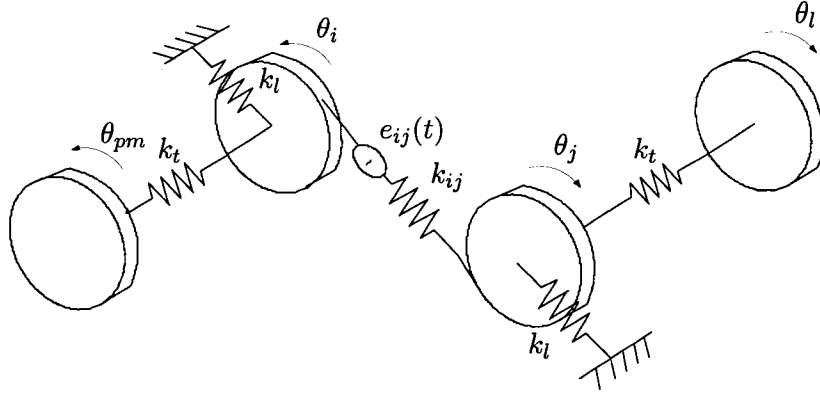


Figure 1.3: (Figure 4 in Ozguven and Houser[21]) *MDOF gear dynamic model*. These models included shaft, bearing, and in some cases, housing flexibilities. In addition, some of these models also included tooth separation and backlash phenomena. k_l represents the combined shaft and bearing lateral stiffness and k_t is the shaft torsional stiffness. θ_l and θ_{pm} are load and prime mover angular displacements, respectively.

- Models for Geared Rotor Dynamics

Geared rotor dynamics models concentrate more on shaft whirling effects rather than on gear dynamic effects. Shafts are allowed to vibrate in two perpendicular lateral directions, and torsional vibration of the system is typically considered. A clear distinction between these and the previous class of models is not present in a number of different cases because some models in the previous section included coupled lateral vibration of a gear shaft system.

- Models for Torsional Vibrations

By neglecting the flexibility in gear teeth and modelling of shafts as torsional springs, a number of these models have been developed and used for natural frequency studies of multiple gear mesh systems. Some researchers have used them for gear dynamic studies.

A limited number of the above models have been used for natural frequency and mode shape analysis. A significantly larger portion have used some form of excitation (TE), and the system's dynamic response in the time or frequency domain have been studied.

Next, a review of papers published in the area of gear dynamics is presented. Each paper is summarized in terms of the type of analytical model used, assumptions made in those models, and the main findings obtained from the models.

A dynamic analysis of a multi-shaft helical gear system is offered in Kahraman et al.[15]. In this model, a TE was obtained from the gear contact software developed at the Ohio State University lab. The TE was then used as the main input to the analytical finite model. A finite element model of the shafts was combined with 3D discrete helical gear pairs. To verify the model, a single-stage helical gear reduction model was compared against experimental results. The model gave good correlation with the experimental results. Once verified, the model was then used to analyze a double-stage helical gear reduction. A number of different parametric studies were then performed with the model. It was concluded that due to a large number of parameters interacting with one another, general design guidelines influencing the dynamic behaviour could not be identified.

In Kahraman et al.[16], a simple finite element model was developed to investigate the dynamic behaviour of a spur gear rotor system. Rigid disks connected by a spring and damper were used to model the gear mesh. The model did not consider tooth separation effects. Natural frequencies and corresponding mode shapes, and forced response of the system to the geometric eccentricities, mass unbalances, and gear transmission error were the main model outcomes. A small number of parametric studies with respect to shaft and bearing compliances were also performed. It was concluded that lowering bearing stiffness values in turn lowered natural frequencies. When compliant shafts were considered in the model, the increase in bearing stiffness above a certain value did not cause a significant change in gear mesh natural frequencies.

Choi et al.[12] investigated the rotordynamics of a 28 MW helical geared system turboset that included a steam turbine, a single helical gear pair, and a generator. This particular system experienced severe coupled torsional, lateral, and axial vibrations. To identify the cause of the vibrations and to solve the issue, a six degrees of freedom (DOF) per node gear dynamic model was developed. Shafts were modelled as rigid nodes connected with springs and a gear mesh was modelled by linear springs acting normally between the two engaged gear teeth. The system's response due to turbine and generator unbalances was investigated first. The results showed some coupled vibrations due to both unbalances, but

not severe vibrations. Next, the effect of the STE excitation on the system's response was modelled. It is this excitation that resulted in excessive coupled vibrations of the system. To reduce the vibrations, a design modification that included a change of the couplings and bearings was implemented. A significant reduction in turbine vibrations, as well as in gear dynamic forces, was achieved as a result of the design modification.

An experimental validation of the finite element code used to simulate dynamic tooth loading in geared rotor systems is given in Baud and Vexlex[7]. For this purpose, both spur and helical gear reductions with flexible shafts and hydrostatic bearings were considered. The gear pair was modelled by two rigid cylinders linked with a series of springs. The shafts were modelled by the use of a two node finite element. Lumped parameter translational and rotational springs were used to model bearings and couplings. Both a normal contact algorithm and a time step integration scheme were used to obtain the forced response of the system. It was found that the bearing and shaft flexibilities could not be ignored in either static or dynamic models. Also, the gear blank flexibilities contribute significantly to the torsional gear mesh stiffness and should not be ignored.

Singh and Vinayak[26] extended the multi-body dynamic model of torsional-translational rigid gear bodies to include compliant gear bodies in these models. First, a new mesh stiffness expression for compliant gear bodies was developed. Then, the new mesh stiffness formulation was combined with the multi-body dynamics framework in order to obtain a complete model of multi-mesh geared systems with compliant gear bodies. As a result, a set of non-linear differential equations with time varying coefficients was formed. The solution of governing equations was possible through direct time domain integration, but was not feasible due to the large number of DOF. Following this, linearization and additional simplifications were used to obtain linear and time invariant equations of motion. A limited number of experimental forced response studies of gear subsystems were compared against this new model with satisfactory results. To fully validate the compliant gear body model presented here, a full scale experimental study of the multi-mesh geared system is still pending.

1.3.4 Gear Contact in ANSYS

In this section, a number of different ANSYS gear contact models are summarized. The goal here is to review the current gear contact algorithms, and to summarize the main findings resulting from these models.

Wei[31] developed both 2D and 3D partial tooth ANSYS models of spur gears in mesh. Contact stresses were obtained from a 2D model while bending stresses were obtained from both 2D and 3D models. The results were compared with the theoretical results calculated from AGMA standards. The results agreed well with each other (within 9 %). It was also concluded that 2D and 3D models produced equally good results. For the transmission error estimation, both the 2D and 3D models were attempted. Due to the fact that whole gear bodies were modelled to obtain the TE, the number of nodes became excessive, and as a result, the 3D model became unfeasible.

Wang[29] used both 2D and 3D ANSYS spur gear contact models to perform a number of different parametric studies. The numerical models were formed over complete mesh cycles, providing detailed information over hand-over regions in spur gears. Hand-over region is defined as the region where the number of engaged teeth pair alternates between the two integer values. A major portion of this study was concerned with the tooth profile modification and its influences on the TE and torsional mesh stiffness. Wang pointed out that when a numerical analysis involves non-linear factors (contact), one should not rely on 2D models for accurate results.

In Barone et al.[6] partial face gear drives were modelled in a 3D Computer Aided Design (CAD) system and then analyzed in ANSYS. To simulate different gear meshing positions, a macro was written that rotated the model into a desired angular position, applied boundary conditions, and solved the model. The effect of the misalignment and tooth profile modification on the contact path, load sharing, and the arc of action was investigated. Pinion root relief yielded lower contact pressures because edge contact was avoided. On the other hand, it resulted in lower load sharing and higher root stresses. In

contrast, gear misalignment produced higher contact stresses and pinion root stresses, but lower TE.

Siriachi[27] used a numerical approach to develop theoretical models to predict the effect of gear tooth damage on TE, torsional mesh stiffness, and load sharing ratio. A new strategy for determination of the appropriate value of the penalty parameter, as the gears rotate through the mesh cycle, was also developed. In addition, an ANSYS macro that defined the torsional mesh stiffness for both fractured and nonfractured teeth was developed. Similar macros were also written for the load sharing ratio and the TE.

Wang and Howard[30] outlined methods for developing an accurate ANSYS contact model of high contact ratio spur gears. The method included adaptive meshing and element size selection, depending on the solution accuracy criteria. Hand-over regions of high contact spur gears were clearly identified in the results for STE, combined torsional mesh stiffness, load sharing ratio, and the tooth stress over the mesh cycle. The existence of hand-over regions indicated the existence of contact outside the normal path of contact due to the gear material elasticity. The hand-over phenomenon is one of the primary reasons behind tooth profile modifications. Four cases of tooth profile modifications were then investigated. These four different modifications were classified as short, long, longer, and optimal tooth reliefs. As the length of the tooth profile modification was increased, the contact ratio of the gears decreased, resulting in greater variations in the TE, mesh stiffness, and root stresses. This trend was true for lightly loaded gears. As soon as the load was increased, the engaged gear pair contact switched back to high contact ratio, but this time resulting in high contact stresses at the relief starting point. Optimal tooth relief length was found to be between the short and long profile modification length.

1.4 Thesis and Research Outline

The research presented here has three objectives. First, development of an ANSYS partial helical gear mesh model from which the STE excitation and mesh stiffness values for a given set of gear parameters could be obtained. The second objective is the creation of an

analytical finite element model of a double-stage helical gear reduction. The last objective encompasses a limited number of parametric studies with the model.

In Chapter 2, a validation of contact model in ANSYS is performed via the use of two cylinder models in contact. Both 2D and 3D models are developed. The finite element results are then compared against theoretical results. Following this, partial helical gears are modelled, meshed, and contact between the gear pair is established. The main results from the 3D ANSYS partial gear model include the STE and torsional mesh stiffness. These two outputs are then used as the main inputs into a finite element analytical MATLAB (Matrix Laboratory) model.

In Chapter 3, the finite element analytical modelling approach is combined with the torsional-translational gear dynamic model in order to obtain an overall system model. Each of the elements making up the system is modelled in terms of their stiffness and mass matrices. The system model contains a finite element model of shaft structures combined with a 3D discrete model of helical gear pairs. Flexible bearings are included in the model as well, but the housing is assumed to be rigid. The modal summation technique used for forced response of the system is explained. In addition to the MATLAB model, an ANSYS model of the benchmark gearbox system is built for natural frequency result verification, and also to assist in visualizing the mode shapes associated with the natural frequencies.

In Chapter 4, the results for the free and forced system's response are presented and discussed. The influence of a number of different parameters on system's dynamics is also given. More specifically, the effect of the output shaft angle, element length, bearing stiffness, and gear pairs relative position on the DTE and bearing force are provided.

Chapter 5 summarizes the main findings of the research. Also, recommendations for future work are included.

Chapter 2

Contact Model in ANSYS

2.1 Contact Problem Overview

It is generally accepted that the structural analysis of any mechanical assembly could possibly undergo three types of non-linear behaviour. These include: material non-linearity (e.g. plasticity), geometric non-linearity (large strains, large deflections) and boundary non-linearity (contact). Contact non-linearity will be examined closely, because the gear teeth in mesh are behaving in this fashion. Contact is considered as a “changing status” type of non-linearity. Depending on whether the contact is open or closed, and if closed, sticking or sliding, the system’s stiffness changes accordingly. In addition, the area over which contact occurs is typically not known at the beginning of analysis.

2.2 ANSYS Contact

This section describes an approach employed in ANSYS for dealing with surface-to-surface contact problems. The intent here is to introduce the basic principles behind the surface-to-surface contact analysis and not to replace a comprehensive edition of an ANSYS tutorial.

Before every structural analysis in ANSYS, the user has a choice of performing the analysis using either the “p” or the “h” method. The h-method was introduced in 1970 and since then it has been considered a common approach employed in solving finite element analysis problems. Linear or quadratic (lower order) displacement assumptions are used in combination with a fine element mesh in areas where the displacements are expected to be non-linear. In other words, a non-linear solution is a combination of a number of linear

solutions. In this case, the error between the theoretical displacement and the finite element solution is controlled by varying the number of elements in the non-linear regions.

The p-method was introduced in the 1990s. Displacements are calculated by manipulating the polynomial level of the element shape functions, which are used to approximate the real solution to the user's desired accuracy. As a consequence, the p-method can automatically improve results for any mesh. When compared to the h-method, the p-method is able to produce desirable results without the rigorous mesh controls. Also, the error estimates offered are more precise and can be calculated locally and globally (point stress rather than strain energy). On the other hand, when using the p-method, the solution may not converge, or may converge slowly, depending on the desired accuracy level. These results should be carefully reviewed.

The choice of preferred method depends on the desired result. For example, if displacements are needed, then the h-method with the relatively coarse mesh is sufficient. To obtain local stresses, the p-method could produce more accurate and faster results. In this thesis, the h-method is employed due to the following reasons:

- Proper contact detection between the two surfaces requires fine mesh in contact regions.
- P-method elements do not support the volume sweeping operation needed for the helical gear creation.
- The displacement results (STE) are required while the stress results are not the objective of this study.

ANSYS classifies contact problems into two types: rigid-to-flexible and flexible-to-flexible. In the first case, one contacting surface is treated as rigid, while the other one is flexible. Metal forming problems fall into this category. The flexible-to-flexible contact approach is applied when both contacting surfaces are considered deformable. ANSYS further divides contact applications into three models:

- Node-to-node: Used to model point to point contact applications. In this model setup, the location of contact has to be known beforehand and a small amount of relative sliding is allowed.

- Node-to-surface: Used to model point to surface contact applications. The exact area of contact does not have to be known beforehand. It allows for small or large amount of relative sliding.

- Surface-to-surface: Used to model surface to surface contact applications. The contact pair is formed by a “contact surface” and a “target surface”.

For a contact pair to be established one surface has to be designated as a contact surface and the other one has to be designated a target surface. ANSYS defines the contact surface as a set of discrete (GAUSS) points, while the target surface is defined as a continuous surface (Figure 2.1). As a consequence, contact elements are not allowed to penetrate the target surface while the target surface is allowed to penetrate the contact surface between the GAUSS points.

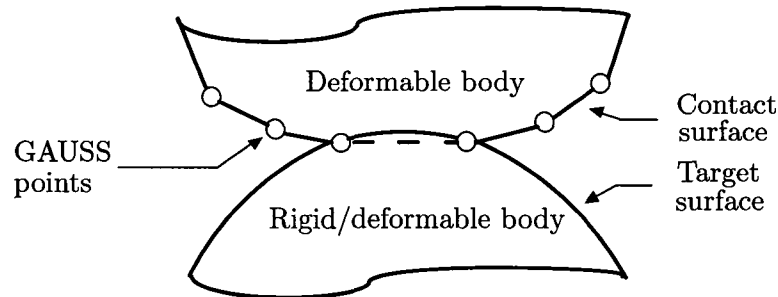


Figure 2.1: (Figure 9.11 in ANSYS[5]) *Contact detection location at GAUSS points.* Target surface is allowed to penetrate contact surface between the GAUSS points. For flexible-to-rigid type of contact, the flexible surface is always chosen as the contact surface. If flexible-to-flexible contact is required, ANSYS provides a set of guidelines that should be followed when assigning contact and target surfaces.

If rigid-to-flexible contact is acquired, the flexible surface is always chosen as the contact surface. In the case of flexible-to-flexible contact analysis, the following guidelines should be followed when creating a contact surface pair:

- If a convex surface is expected to come into contact with a flat or concave surface, the flat/concave surface should be designated as the target surface.
- If one surface has a fine surface mesh, and the other has a coarse mesh, the fine mesh surface should be designated as the contact surface.
- If one surface is stiffer than the other, the softer surface should be the contact surface.
- If higher-order elements lie beneath one of the external surfaces, and lower-order elements lie underneath the other surface, the surface with the underlying higher-order elements should be the contact surface.

Once the contact and target surfaces have been chosen, ANSYS offers five options of enforcing the compatibility between the contacting surfaces:

- **Penalty Method:** This approach positions a spring between the two contacting surfaces. The spring stiffness is referred to as the “contact stiffness”. When two surfaces are apart the spring is inactive, but when two surfaces begin to interpenetrate the spring becomes active. The spring then deflects until the equilibrium is reached.
- **Pure Lagrange Multiplier Method:** When contact is closed, zero penetration is enforced. When sticking occurs, zero slip condition is enforced. No contact stiffness value is required for this approach.
- **Augmented Lagrangian Method:** The default option when surface-to-surface contact is performed. It is an iterative series of penalty methods. In the first series of iteration, penalty stiffness is used to enforce contact compatibility. Once the equilibrium is reached, the penetration tolerance is checked, and then contact pressure is augmented to continue the iterations.
- **Pure Lagrange Multiplier Method and Penalty Method:** This method is a combination of the Pure Lagrange Multiplier method and the Penalty method. A zero penetration is enforced, while a small amount of slip is allowed when sticking occurs. The use of chattering control parameters is required.

- Internal Multipoint Constraint (MPC): The program builds MPC equations internally based on contact kinematics.

Initial contact status is a very important parameter that needs to be properly defined before the model is submitted for solving. The system stiffness matrix will become singular if a rigid body mode (open contact) is detected. The three most common ways to adjust the contact initial conditions in ANSYS are:

- Initial Contact Closure (ICONT): A band is created around the target surface. Any contact points that are contained within the band are then shifted onto the target surface. Only small adjustments are recommended.

- Initial allowable penetration range (PMAX and PMIN): In this case, the target surface is physically moved into the contact surface. ANSYS uses 20 iterations to bring the target surface within the range specified by the PMIN and PMAX. If not successful, the analysis proceeds with the original contact geometry.

- Use of real constant CNOF to specify contact surface offset: Moves the entire contact surface towards the target surface. ANSYS automatically provides a CNOF value based on the user's choice of either initial gap closure or the initial penetration minimization.

All three techniques described above could be employed independently, or in combination with each other depending on the nature of the problem. Friction options in ANSYS include: static coefficient of friction, cohesion value, the ratio of static to dynamic friction, and a decay coefficient. The cohesion value allows the user to setup an initial friction coefficient value that results in sliding resistance, even if there is no normal load. The decay coefficient allows the user to control the transition between the static and dynamic friction based on the relative velocities of the two contacting surfaces. Once the contact pairs are defined with appropriate options, the contact solution phase can be executed. Based on previous experiences, the load application should begin with a fraction of the total load and then increase gradually. Also the CNCHECK command should be issued to check the initial contact status before proceeding with the solution.

To solve non-linear problems, ANSYS uses the Newton-Raphson method. Instead of applying the load in one step, the load is broken down and applied in a series of load increments. In addition, each increment is divided into smaller load steps. This is done in order to improve the convergence characteristics of the algorithm. If convergence difficulties are experienced, the NLHIST command should be issued to monitor contact information during the solution.

2.3 ANSYS Contact Model Validation

There are a number of ANSYS university licenses available for use. They all have a different number of maximum nodes available to them. A university intermediate license was available for use in this thesis work. The node limit for this license is 32000 nodes. When solving contact problems for displacement, it is crucial to have a fine mesh at contact surfaces for proper contact detection. If stress results are the objective of the contact model, then a fine mesh below the contacting surfaces has to be provided, in addition to the fine mesh of the contacting surfaces. If the contact model is built as a 3D model, and stress effects are sought after, meaning a fine mesh below the contacting surfaces is required, the number of nodes quickly reaches its limit and the model becomes unusable. To avoid the above mentioned issue, many researchers choose a 2D modelling approach to represent 3D models, or partial 3D models are utilized.

To verify a 3D ANSYS contact model for use in gear analysis, an analytical solution for two semi-cylinders in contact is compared with the results from ANSYS. The main objective is the determination of the mesh size needed at contact areas to obtain valid displacement results from ANSYS. In this case, the main objective is not stress results, as that would require a finer mesh below the surface of the two cylinders that would exceed the number of allowed nodes. The semi-cylinders with the properties given in Table 2.1 were analyzed. Friction is not included in any of the ANSYS models (cylinder and gear models) developed in this thesis.

Table 2.1: *Steel cylinder properties.* Cylinders with the properties given here are used to validate both 2D and 3D ANSYS contact models.

Parameter	Notation(Units)	Cylinder 1	Cylinder 2
diameter	$d(mm)$	50	50
length	$l_c(mm)$	15	15
modulus of elasticity	$E(GPa)$	207	207
Poisson's ratio	ν	0.292	0.292

The theoretical approach is described first. The solution to the contact problem was first given by Hertz in 1881[9]. When two cylinders are brought together in point or line contact, and then loaded, local deformation occurs. As a result, the point or line of contact turns into the rectangular area of contact of width $2b$ and length l_c (Figure 2.2). All normal stresses are compressive in nature. A maximum shear stress equal to $0.304p_{max}$ occurs at a depth of $0.786b$. The half-width b is given by the following formula

$$b = \sqrt{\frac{2F \frac{(1-\nu_1^2)}{E_1} + \frac{(1-\nu_2^2)}{E_2}}{\pi l_c \left(\frac{1}{d_1} + \frac{1}{d_2} \right)}}, \quad (2.3.1)$$

where

b = contact area half-width,

F = compressive force,

ν_1 and ν_2 = Poisson's ratio of cylinders 1 and 2, respectively,

E_1 and E_2 = modulus of elasticity of cylinders 1 and 2, respectively,

π = constant,

l_c = cylinder length, and

d_1 and d_2 = diameter of cylinders 1 and 2, respectively.

The maximum pressure (p_{max}) is obtained as

$$p_{max} = \frac{2F}{\pi b l_c}. \quad (2.3.2)$$

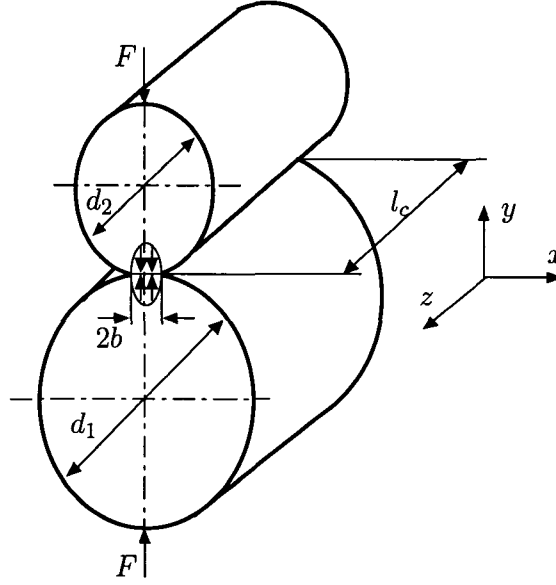


Figure 2.2: *Parallel axis cylinder contact.* Under a compressive load, the line of contact turns into the rectangular area of contact of width $2b$ and length l_c . Maximum shear stress occurs at a depth of $0.786b$.

If both cylinders have the same material properties, then the approach displacement (δ) is calculated as

$$\delta = \frac{2 F}{\pi l_c} \left(\frac{1 - \nu^2}{E} \right) \left[\frac{2}{3} + \ln \left(\frac{d_1}{b} \right) + \ln \left(\frac{d_2}{b} \right) \right]. \quad (2.3.3)$$

Once the above parameters are calculated, the stresses along y axis are obtained as

$$\sigma_x = -p_{max} \left(\frac{1 + 2 \frac{y^2}{b^2}}{\sqrt{1 + \frac{y^2}{b^2}}} - 2 \left| \frac{y}{b} \right| \right), \quad (2.3.4)$$

$$\sigma_y = \frac{-p_{max}}{\sqrt{1 + \frac{y^2}{b^2}}}, \text{ and} \quad (2.3.5)$$

$$\sigma_z = -2\nu p_{max} \left(\sqrt{1 + \frac{y^2}{b^2}} - \left| \frac{y}{b} \right| \right), \quad (2.3.6)$$

where

σ_x , σ_y , and σ_z = stress in x , y , and z directions.

Next, a 2D ANSYS contact cylinder model was built with a fine mesh capable of capturing proper stress distribution below contacting surfaces. 2D PLANE82 plane strain

elements were used to mesh the geometry. The applied load was incremented from 1000 N to 10000 N in increments of 1000 N . Figure 2.3 shows the *von Mises* stress distribution under 5000 N of compressive load applied to the cylinders. Stress units are MPa and displacement units are mm . Figure 2.4 shows displacement results for both a 2D ANSYS

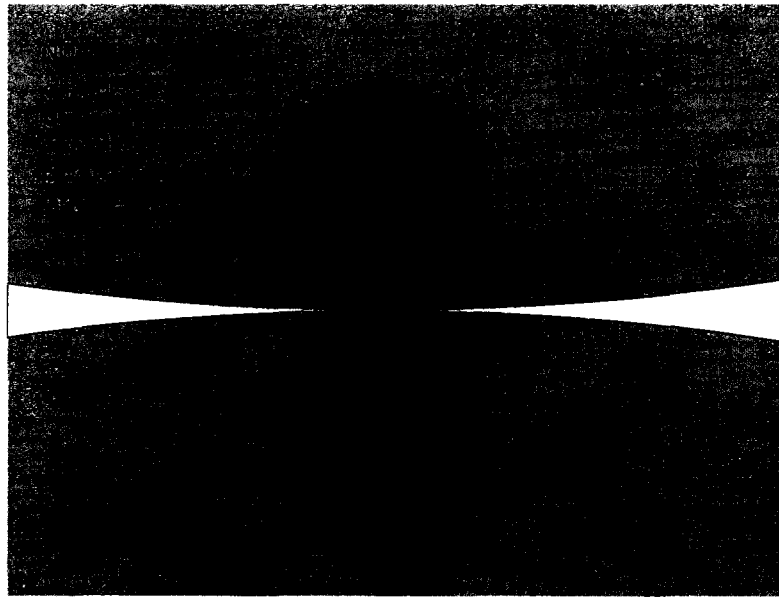


Figure 2.3: 2D ANSYS *Von Mises* stress plot for two cylinders. Compressive load of 5000 N applied to two contacting steel cylinders results in a maximum stress of 546 MPa . Elliptical stress distribution below contacting surfaces is also shown.

model, and a theoretical model. The ANSYS results agree well with the theoretical results. Surface pressure results are plotted in Figure 2.5. The theoretical stress in the x direction along the y axis is compared to the 2D model stress in Figure 2.6. Results for the y and z directions have the same degree of correlation and are not shown here for clarity purposes. In conclusion, a 2D model shows extremely good correlation with theoretical results in all three aspects (displacement, surface pressure, and stress distribution) considered.

Next, the 3D ANSYS model was built. The volume sweep option was used to mesh the 3D model. The side area was meshed first with 1.5 mm elements. After this, a two level mesh refinement was applied near contact areas. The contact wizard was then used

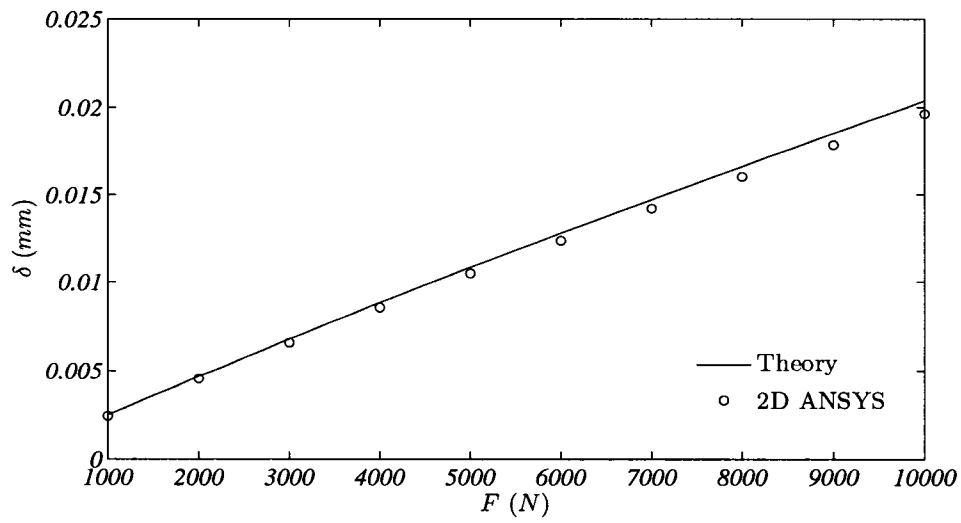


Figure 2.4: 2D ANSYS and theoretical displacements.

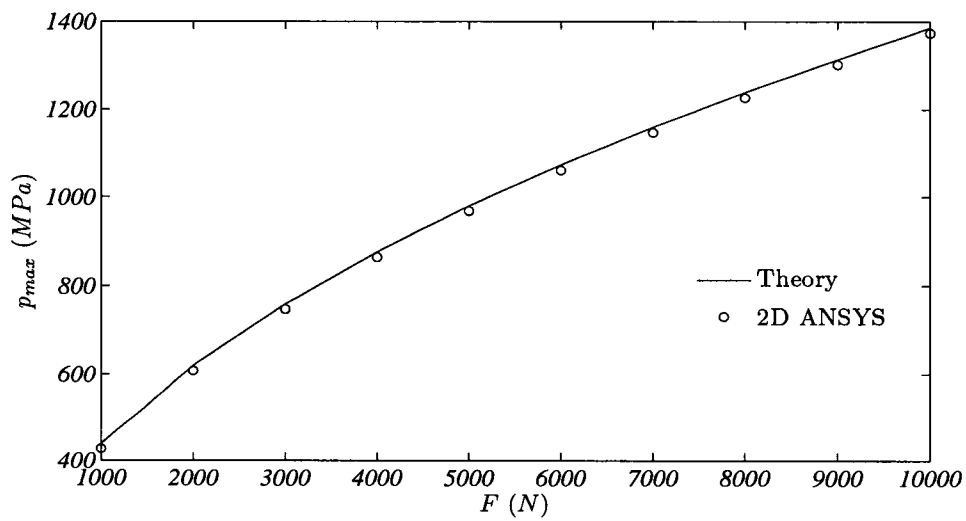


Figure 2.5: 2D ANSYS and theoretical surface contact pressures.

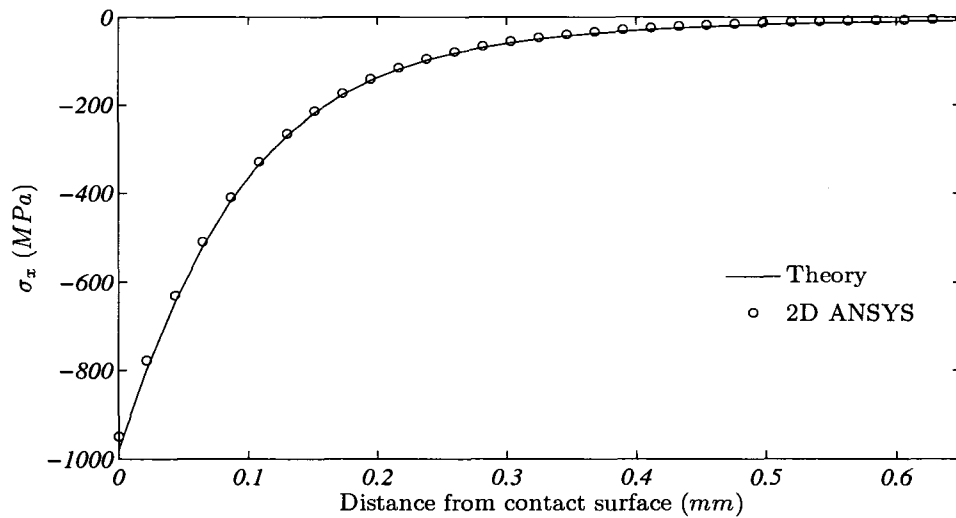


Figure 2.6: 2D ANSYS and theoretical stress distribution along y axis.

to establish the contact between the two cylinders. To initiate the contact, and to enable convergence, an automatic initial gap adjustment option was used. Figure 2.7 shows a meshed finite element model. Again, the applied load was incremented from 1000 N to 10000 N in increments of 1000 N . Figure 2.8 shows the displacement results obtained from Hertzian contact theory and both ANSYS models. Both ANSYS results agree within 2 % of the theoretical results. Next plot, Figure 2.9 shows the comparison of maximum contact pressure results obtained from the same models. Again, there is a good correlation between the two results (within 3 %). Theoretical stress in the x direction along the y axis is compared with both 2D and 3D model stresses in Figure 2.10. The 3D model produces non-correlated results due to relatively coarse mesh size. Results for the y and z directions for the 3D model show the same degree of non-correlation as the one for the x direction, and are not shown here for clarity purposes. As mentioned earlier, the highest shear stress between the two parallel contacting cylinders occurs at a distance of $0.786b$ below the contacting surfaces. Depending on the load applied to the cylinders, the half-width b changes and consequently, the location of the maximum shear stress zone changes. For example, for a 1000 N applied load, the maximum shear stress occurs at 0.076 mm below the surface, while for 5000 N , the maximum shear load occurs at 0.170 mm below

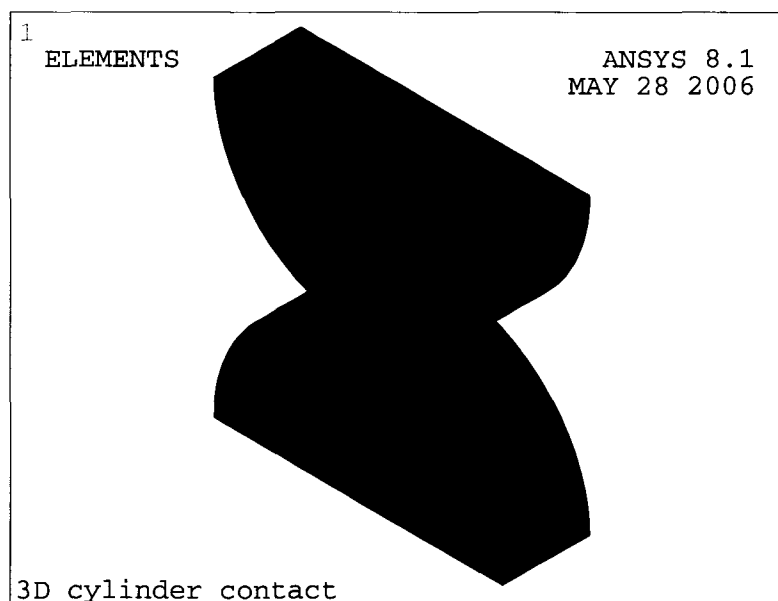


Figure 2.7: 3D ANSYS steel cylinder contact model. Half cylinders were modelled due to symmetry. The volume sweep option with SOLID95 brick finite elements was used to mesh the 3D model. The model contains 29000 nodes.

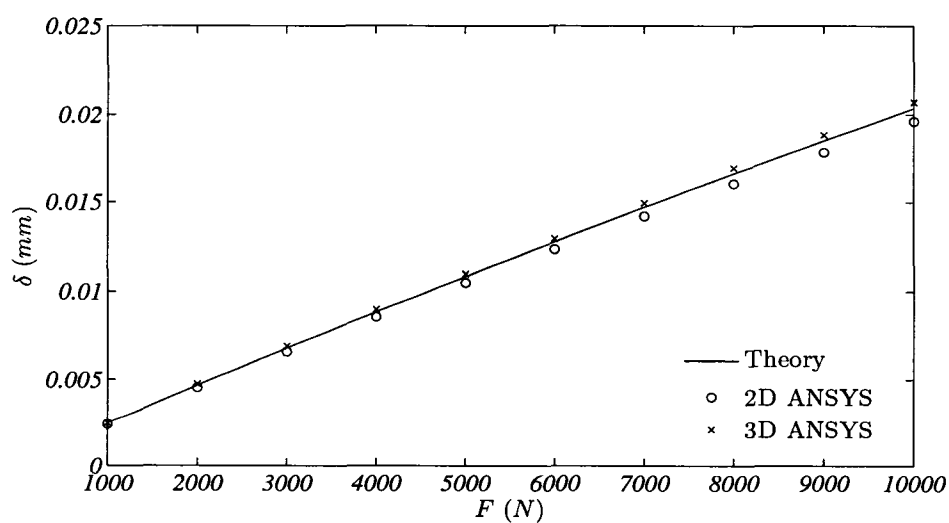


Figure 2.8: 2D ANSYS, 3D ANSYS, and theoretical displacements. Both ANSYS model results agree well with the theoretical Hertzian displacement results.

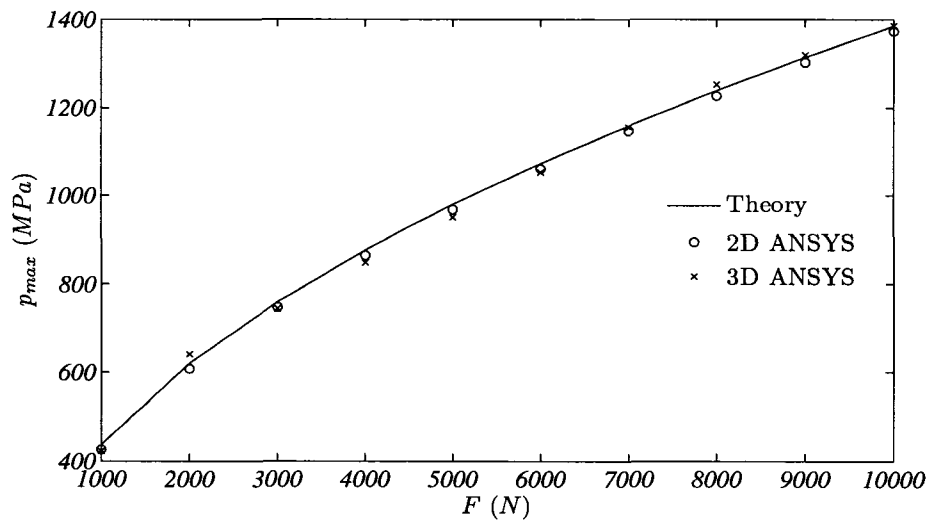


Figure 2.9: 2D ANSYS, 3D ANSYS, and theoretical surface contact pressures.

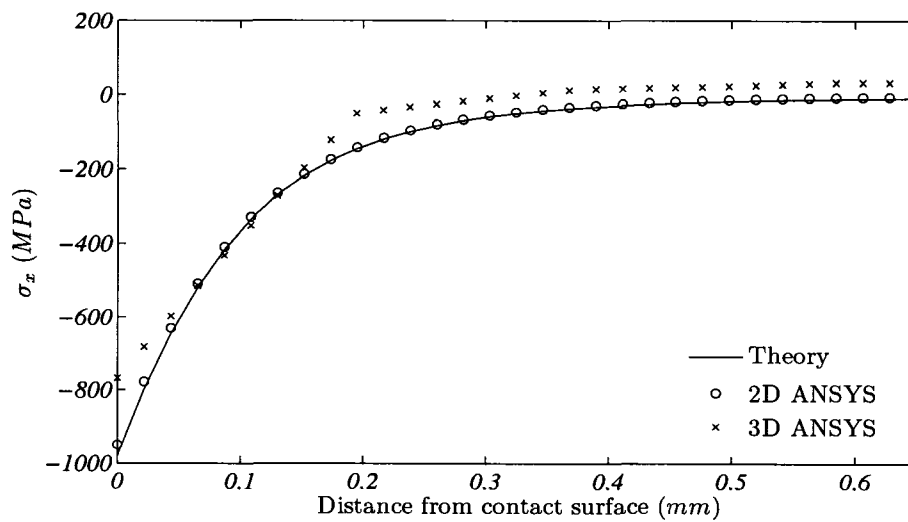


Figure 2.10: 2D ANSYS, 3D ANSYS, and theoretical stress distribution along y axis. 2D ANSYS model results agree well with the theoretical Hertzian stress results. 3D ANSYS model fails to accurately predict stress distribution due to a coarse mesh.

the surface. The development of a 3D model with fine mesh that is capable of capturing proper stress distribution is not needed for the purpose of this research.

As shown above, when performing any type of a computer modelling, one has to understand the theory behind the phenomenon being modelled. Otherwise, the results obtained could be misleading and potentially dangerous if blindly relied upon. Even though the 3D model showed good correlation with the more refined 2D model in displacement and contact surface pressure estimations, it failed in showing accurate stress distribution below the contacting surfaces. When analyzing parts that come into contact, the area just below the surface is the most critical area as far as the parts failure is concerned. If contact pressure and displacements of contacting parts are of interest, the 3D model developed here is a valid one and can be used to accurately predict both.

2.4 Helical Gear Pair Contact

In Section 2.3, a 3D ANSYS contact model of two cylinders proved its validity, if used for displacement purposes. The fine mesh at the contacting surfaces is sufficient only for displacement studies. In this section, a partial 3D helical gear mesh model is developed with the TE and mesh stiffness being the main objectives of the model. In addition, a limited number of parametric studies on a given gear pair is performed.

The gear pair with the properties given in Table 2.2 was chosen as the base model for the investigation. It is common for helical gear properties to be given in terms of normal parameters rather than transverse ones. Normal plane gear parameters are usually defined for helical gear manufacturing purposes. The reason they are given here in terms of their transverse properties is because the transverse plane was used as the base plane for the involute gear profile creation in a 3D ANSYS gear model. The true involute geometry of a helical gear is in the plane of rotation (transverse plane). A helix angle is used to relate the normal plane parameters to the transverse plane parameters. Once a single involute gear tooth profile was created in the transverse plane, it was then copied a desired number of times to create a partial gear tooth profile ready for extrusion along the helical curve.

Table 2.2: *Helical gear properties.* The helical gear pair with the properties given in this table was chosen as the base model for modelling purposes. LH and RH abbreviations in this table stand for Left and Right Handed helix angle, respectively.

Parameter	Notation(Units)	Gear i	Gear j
number of teeth	N	30	60
transverse module	$m_t(mm)$	2	2
transverse pressure angle	$\phi_t(degrees)$	20	20
helix angle	$\beta(degrees)$	15 LH	15 RH
face width	$w(mm)$	15	15
hub radius	$r_h(mm)$	12.5	12.5
tip relief	$\chi(mm)$	0.5	0.5
modulus of elasticity	$E(GPa)$	207	207
Poisson's ratio	ν	0.292	0.292

To create the tooth profile that is conjugate with the counterpart basic rack, a set of mathematical relationships is developed by Wang[29] and is presented here. The following terms have to be defined before the equations are presented:

- m_t is the transverse module,
- N is the number of teeth,
- Addendum, $a_d = \epsilon m_t$ ($\epsilon = 1$ for standard tooth helical gears),
- Dedendum, $d_e = \eta m_t$ ($\eta = 1.25$ for standard tooth helical gears),
- Tip radius, $r_t = \rho m_t$ ($\rho = 0.25$ for standard tooth helical gears),
- ϕ_t is the transverse pressure angle,
- o is the cutter offset, and

- $Q = \frac{o}{m_t}$ is the addendum modification coefficient.

Figure 2.11 shows a single gear tooth profile with the basic parameters given above.

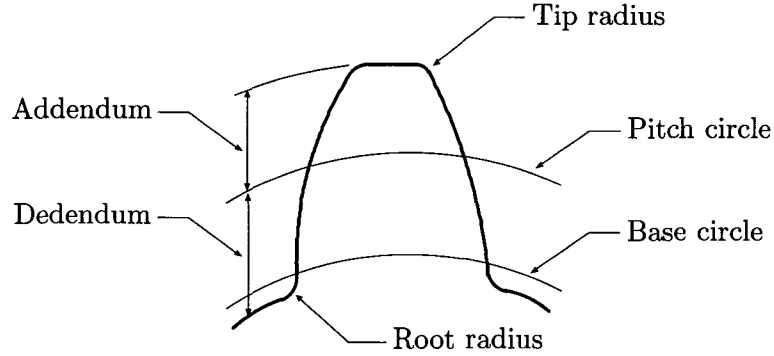


Figure 2.11: *Single gear tooth profile nomenclature.* The pitch circle is a theoretical circle upon which all the calculations are based. The Addendum is the radial distance between the pitch circle and the addendum circle. The Dedendum is the radial distance between the pitch circle and the dedendum circle. The involute tooth profile is derived from the base circle.

The gear tooth profile is defined by the involute portion and by the fillet portion. The x and y coordinates of the involute tooth profile are given by the following two equations

$$x(\theta) = \frac{Nm_t}{2} \left[\sin(\theta) - \left(\left(\theta + \frac{\pi}{2N} \right) \cos(\phi_t) + \frac{2Q}{N} \sin(\phi_t) \right) \cos(\theta + \phi_t) \right], \quad (2.4.1)$$

and

$$y(\theta) = \frac{Nm_t}{2} \left[\cos(\theta) + \left(\left(\theta + \frac{\pi}{2N} \right) \cos(\phi_t) + \frac{2Q}{N} \sin(\phi_t) \right) \sin(\theta + \phi_t) \right]. \quad (2.4.2)$$

The parameter θ of the involute curve is limited by the following range of minimum and maximum values

$$\theta_{min} = \frac{2}{N} [U + (V + Q) \cot(\phi_t)], \quad (2.4.3)$$

and

$$\theta_{max} = \frac{1}{N \cos(\phi_t)} \sqrt{(2 + N + 2Q)^2 - (N \cos(\phi_t))^2} - \left(1 + \frac{2Q}{N} \right) \tan(\phi_t) - \frac{\pi}{2N}. \quad (2.4.4)$$

The parameter U is defined as

$$U = - \left[\frac{\pi}{4} + (\epsilon - \varrho) \tan(\phi_t) + \frac{\varrho}{\cos(\phi_t)} \right], \quad (2.4.5)$$

and parameter V is given as

$$V = \varrho - \epsilon. \quad (2.4.6)$$

The fillet portion of the tooth profile is defined next. The x and y coordinates of the profile are calculated as

$$x(\theta) = m_t(P \cos(\theta) + H \sin(\theta)), \quad (2.4.7)$$

and

$$y(\theta) = m_t(-P \sin(\theta) + H \cos(\theta)). \quad (2.4.8)$$

Again, the limiting values of θ are obtained as

$$\theta_{min} = \frac{2}{N} [U + (V + Q) \cot(\phi_t)], \quad (2.4.9)$$

and

$$\theta_{max} = \frac{2U}{N}. \quad (2.4.10)$$

Before P and H parameters used in the above equations are defined, an additional parameter L has to be introduced as

$$L = \sqrt{1 + 4 \left(\frac{V + Q}{2U - N\theta} \right)^2}. \quad (2.4.11)$$

Now,

$$P = \frac{\varrho}{L} + \left(U - \frac{N\theta}{2} \right), \quad (2.4.12)$$

and

$$H = \frac{2\varrho}{L} \left(\frac{V + Q}{2U - N\theta} \right) + V + \frac{N}{2} + Q. \quad (2.4.13)$$

Once the parametric equations for the tooth profile were defined, they were then programmed into ANSYS using APDL (ANSYS Parametric Design Language). The user then only needs to supply the basic gear parameters defined earlier, and the number of desired points along each portion of the tooth profile. The points were then connected with a spline to form a tooth profile. The profiles were mirrored and copied a desired number of times to get the 2D gear profile ready for the extrusion. ANSYS macro was used again to obtain the helix needed for the extrusion. The APDL code that produced the involute profile points and the helical profile for that particular gear is attached in Appendix A. The APDL code

attached in Appendix A is the combination of the involute code given by Wang[29], and the code for the helical gear curve creation.

A three tooth model of each gear was chosen because of the fact that the contact ratio of this helical gear pair was calculated to be approximately 2.2. This means that during mesh, these particular gears alternate between having two and three teeth engaged. Therefore, a three tooth partial model would be sufficient for one complete mesh cycle description. After finishing the solid model, the meshing procedure followed a similar procedure described in Section 2.3, where the 3D cylinder model was meshed. The cylinders modelled in Section 2.3 had dimensions similar to the gears analyzed here, and their radii of curvature resembled the gear tooth profiles. First, the gear face area was meshed with 1.75 *mm* elements. Then, a two level mesh refinement was applied to the contacting tooth profiles of both gears. Next, the meshed area was swept with SOLID95 elements. Due to the node number limitation, there were only five divisions along the sweep direction. This was found to be acceptable as long as the helix angle of the gears did not exceed 15°. Figure 2.12 shows a screen shot of the meshed model. The screen shot on the right shows the fine mesh applied to the gear teeth in mesh. The tooth side that made contact with another tooth was given additional mesh refinement when compared to the non-contacting tooth side. This was done in order to reduce the number of nodes in the model.

The contact wizard was used to define the contact surfaces and to initiate contact between the two surfaces. The mating teeth on both gears were coupled to form contact pairs. Depending on the angular position of the gears, a different contact pair was chosen to be forced to initiate contact, while the other two pairs were not given any initial contact adjustment. As the applied load was increased, the engaged gear pair deformed, thus forcing the other gear pairs to come into contact.

To obtain the STE, the hub of the output gear (gear j) was constrained in all six DOF, while the hub of the input gear was allowed to rotate around the gear axis only. A pilot node contact option was used to apply torque to the input hub and to constrain the output hub. To obtain the STE for a complete mesh cycle, the gears had to be rotated through

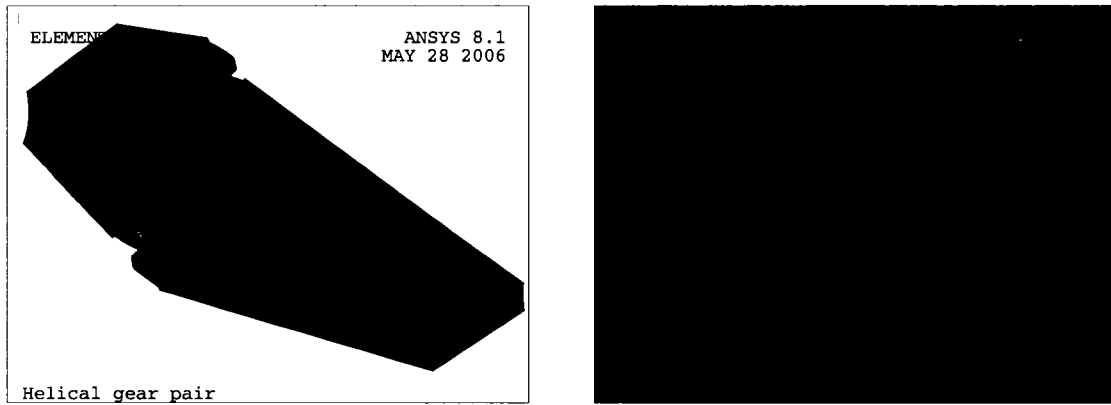


Figure 2.12: *3D partial helical gear pair mesh.* A macro was developed and used to generate an involute profile for gear teeth. SOLID95 brick elements were used to mesh the model. A pilot node contact option was used to apply the torque to the pinion and to restrain the gear. The screen shot on the right shows the fine mesh applied to the gear teeth in mesh.

a 12° angle (increments of 1°) from their initial position. At each angular position, the gears were loaded and the solution was initiated. The rotation of the input pilot node, due to the gear tooth deformation and local contact deformation, was then recorded, and Equation 1.3.2 was used to obtain the TE. It is negative due to the fact that the output gear always lags behind the input gear. To obtain the torsional mesh stiffness, the applied load at each angular position was divided by the TE for that angular position.

For the first simulation, the applied load was incremented from $100\text{ N}\cdot\text{m}$ to $500\text{ N}\cdot\text{m}$ in increments of $100\text{ N}\cdot\text{m}$. The TE plot for this simulation is shown in Figure 2.13. 0° from the reference in the above plot represents the position of the gears when only two pairs of mating gear teeth are in contact. As the gears are rotated away from the reference position, the line of contact moves up along the pinion tooth profile, and as result, the TE increases. At around 4° of pinion rotation from the reference, the contact of a third gear tooth pair becomes active. By this time, the tooth pair on the opposite side of the mesh is nearly leaving the mesh. Between 4° and 8° , there are three gear tooth pairs in contact with the two outside pairs, making significantly shorter lines of contact when compared to the case of two fully engaged teeth (around reference and again around 11°). As a result, the

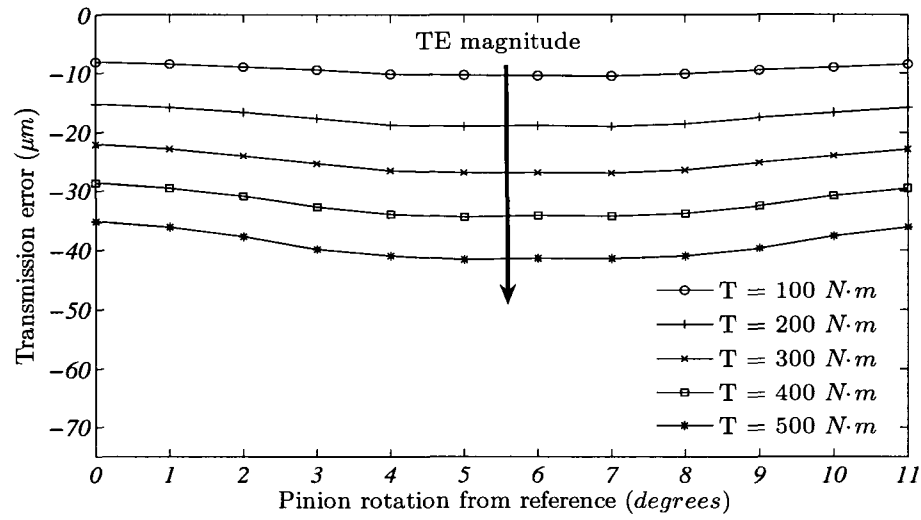


Figure 2.13: Transmission error as a function of pinion position. The applied load was incremented from $100 \text{ N}\cdot\text{m}$ to $500 \text{ N}\cdot\text{m}$ in increments of $100 \text{ N}\cdot\text{m}$. The TE magnitude increases with the increase in applied load.

increase in the TE is eminent. The TE plot for only one mesh cycle is shown. The torsional mesh stiffness plot corresponding to the above TE plot is shown in Figure 2.14. Again, the mesh stiffness is inversely proportional to the TE. As the load increases, the torsional mesh stiffness increases for a given pinion rotation angle. This is typical behaviour for systems where a non-linear contact analysis is performed.

Next, the effect of the pressure angle on TE is investigated. For this investigation, an input load of $200 \text{ N}\cdot\text{m}$ was chosen and applied with three different pressure angles (17.5° , 20° , and 22.5°). The other gear properties given in Table 2.2 remained the same. Figure 2.15 shows the TE results for this run. The decrease in pressure angle has a positive effect on the TE magnitude. This is due to the fact that a decrease in pressure angle results in a higher contact ratio. The TE mean and peak values obtained from ANSYS are both reduced. In addition, a high contact gear pair is less sensitive to tooth profile errors when compared to a low contact ratio gear pair. On the other hand, when the pressure angle is decreased, the tooth geometry is changed in such a way that there is a decrease in tooth thickness, strength, and stiffness. This increases bending and compressive stresses in the gear teeth. Also, an increase in contact ratio translates into higher sliding velocity,

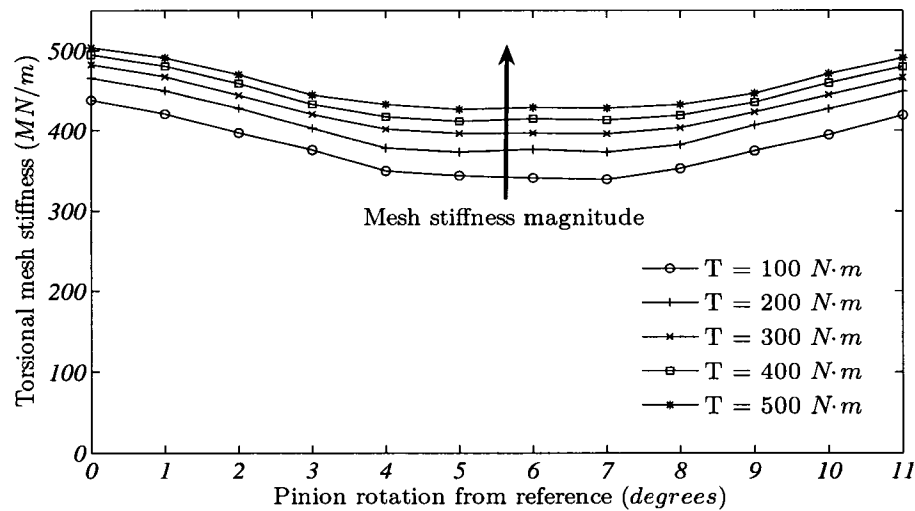


Figure 2.14: Torsional mesh stiffness as a function of pinion position. The torsional mesh stiffness increases with applied load. This behaviour is typical in contact stiffness analysis.

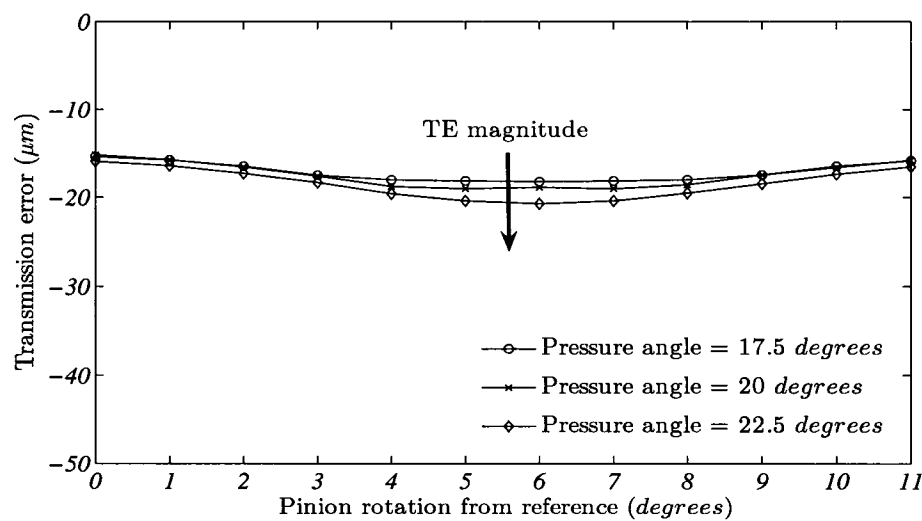


Figure 2.15: Transmission error as a function of pinion position with constant torque. An input load of $200 \text{ N}\cdot\text{m}$ was chosen, and applied with three different pressure angles. The increase in the pressure angle has a negative effect on the TE magnitude. A 20° pressure angle provides a good compromise between the requirements for low stresses and low TE.

resulting in higher power losses. A 14.5° pressure angle used to be the standard in the industry. This pressure angle provided quiet running gears, but required undercutting to prevent interference which further reduced gear tooth strength. The demand for smaller pinions with fewer, but stronger, teeth resulted in an increase in pressure angle to 20° or 25° . A 20° pressure angle provides a good compromise between the requirements for low stresses and low TE. The plot for the torsional mesh stiffness for the above TE plot is shown in Figure 2.16. Again, with the decrease in pressure angle, the tooth bending stiffness decreases, but because of the higher contact ratio, the overall torsional mesh stiffness is increased.

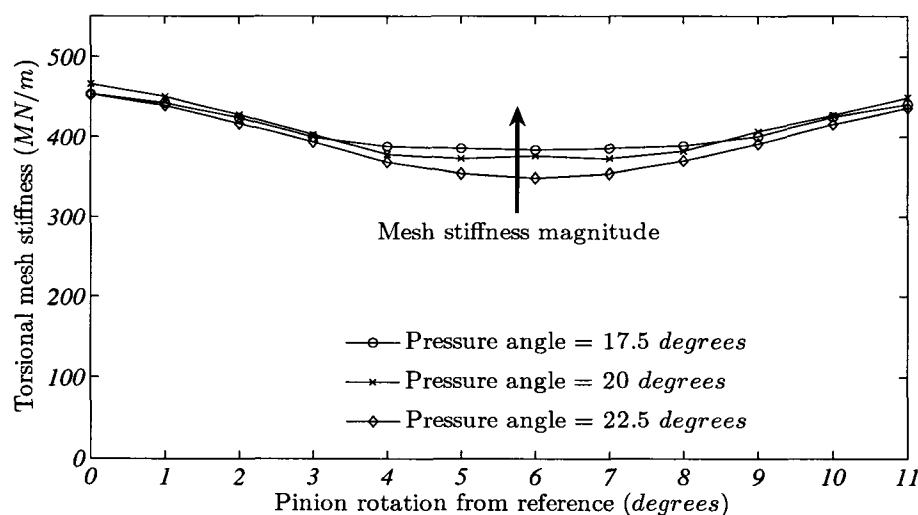


Figure 2.16: Torsional mesh stiffness as a function of pinion position with constant torque. Pressure angle of 17.5° provides the highest torsional mesh stiffness value for the three cases considered.

To justify the use of time invariant mesh stiffness for helical gear dynamic analysis, a comparison between the spur gear pair mesh stiffness and helical gear pair mesh stiffness is presented. For this study, the helical gear pair with the properties given in Table 2.2 was chosen. The spur gear pair properties were also taken from the same table. The only difference is that the spur gear tooth profile was extruded along the gear longitudinal axis, and not along the helix curve. To obtain the transmission error, the procedure used for helical gear transmission error was also used for the spur gear pair. The mesh stiffness

results for the two gear pairs are shown in Figure 2.17. The main reason for the mesh stiffness oscillations in spur gear pairs is the abrupt change between one and two tooth pairs in contact. Helical gears, because of a higher contact ratio, result in a smoother mesh stiffness curve. The difference between the two results is even more obvious when plotted in frequency domain. Both TE and the mesh stiffness are periodic functions with the period of 12° of pinion rotation. Figure 2.18 shows the same two mesh stiffness plots shown in

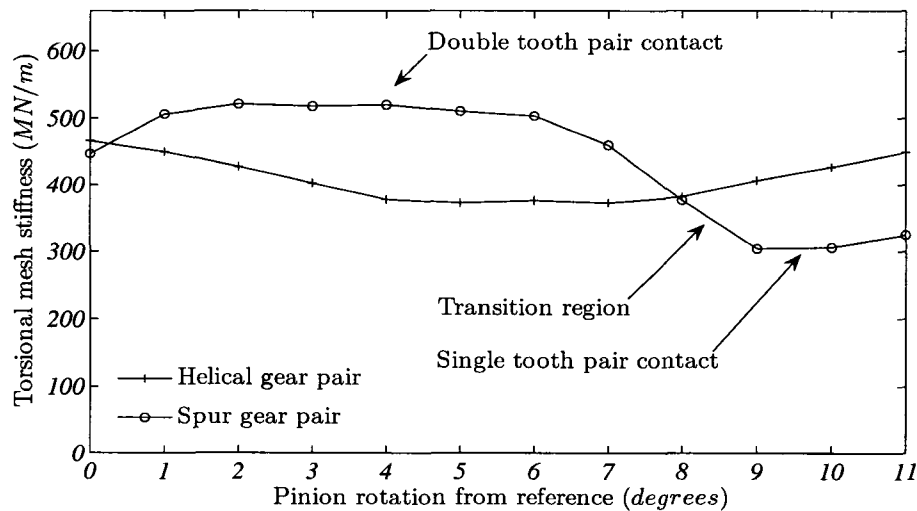


Figure 2.17: *Spur and helical gear mesh stiffness comparison.* A torque of $200 \text{ N}\cdot\text{m}$ applied to each gear pair. A transverse pressure angle of 20° was chosen for both gear pairs. A double tooth spur gear contact between 1° and 6° of pinion rotation results in a relatively steady mesh stiffness plot. As the pinion rotation continues throughout the mesh cycle, the transition between a double and single tooth pair occurs, resulting in a significant decrease in mesh stiffness. The helical gear pair produces a much smoother mesh stiffness plot.

Figure 2.17 but in a frequency (Fourier series terms) domain and without the steady state term. Figure 2.19 shows the TE frequency plots obtained from the same simulation used to produce Figure 2.18. Based on the above results, one can see why the time invariant helical gear mesh stiffness assumption is used in gear dynamic models.

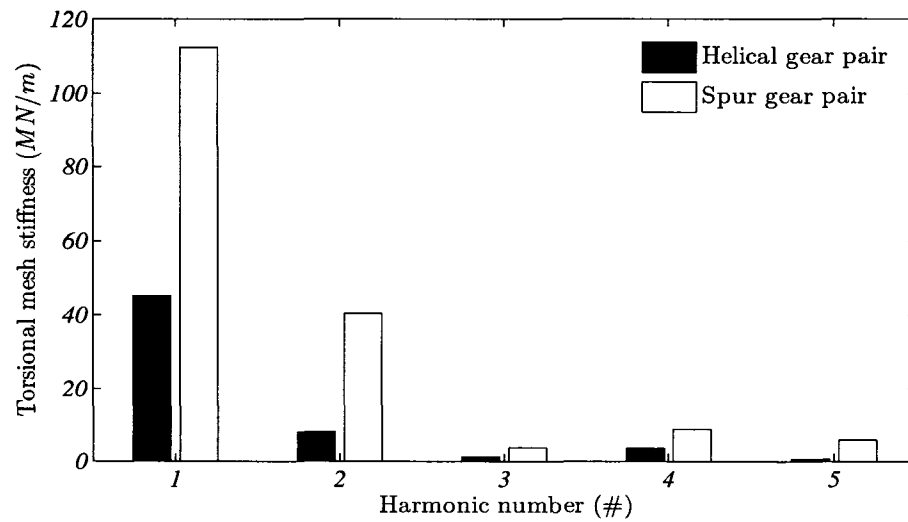


Figure 2.18: *Spur and helical gear pair mesh stiffness harmonics.* Spur gear pair mesh stiffness harmonics amplitudes are significantly larger when compared to the helical gear harmonics for all harmonic numbers shown.

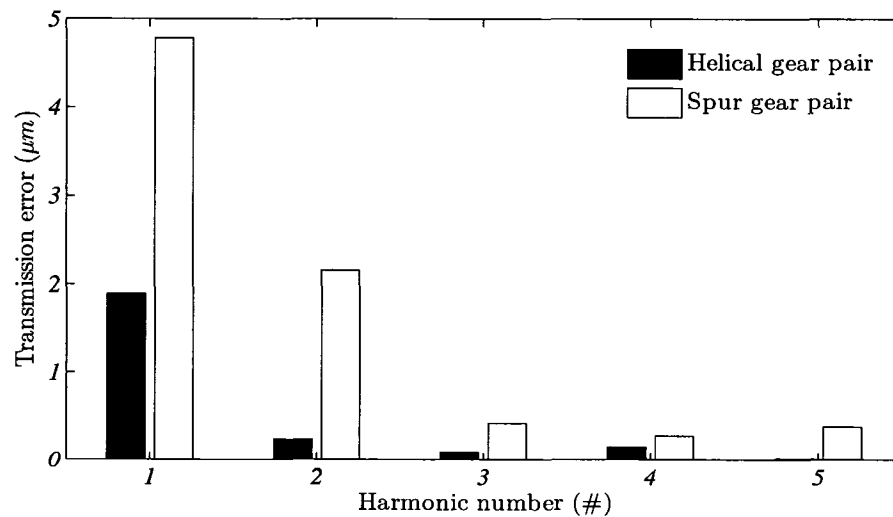


Figure 2.19: *Spur and helical gear pair TE harmonics.* Spur gear pair TE harmonics amplitudes are significantly larger when compared to the helical gear harmonics for all harmonic numbers shown.

Chapter 3

Analytical Finite Element Model

To develop an analytical finite element model for any gear reduction system, the following six general steps should be followed:

- Represent gear mesh with a linear spring in series with the TE excitation.
- Divide shafts into beam elements connected to each other through points (nodes).
- Describe the behaviour of each element (i.e. derive its stiffness, damping, and mass matrices, and load vector in local coordinate system).
- Obtain the local to global coordinate system transformation matrix for each element and describe the behaviour of the system by combining the behaviour of each of the elements (assemble their stiffness, damping and mass matrices, and load vectors).
- Apply appropriate boundary conditions.
- Reduce the system (if safe to do so) and solve.

3.1 Gearbox Model Layout

In this section, a brief description of the overall model is given, with the intent to provide an outline of what follows in the remainder of Chapter 3. Figure 3.1 describes the system's physical layout in a global coordinate system. It represents the left side view of a double-stage reduction gearbox. The system is positioned in the $Y-Z$ global coordinate plane with the global origin placed at the left end of the input shaft.

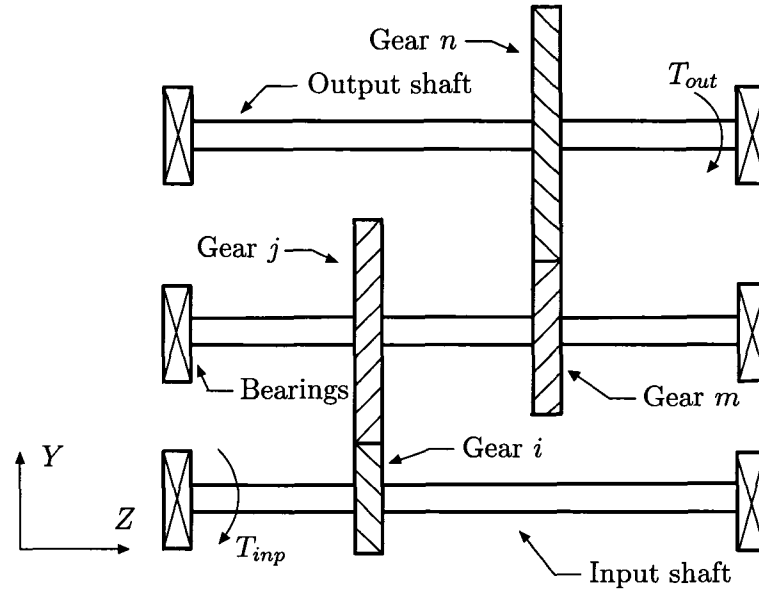


Figure 3.1: *Gearbox layout.* This figure represents the gearbox orientation with all the components. The gearbox model contains three shafts, four helical gears, and six bearings. The housing is assumed to be rigid.

The finite element schematic of the same system is shown in Figure 3.2. Each shaft is divided into six beam elements (shown as springs). There are 18 shaft elements in total. Spring elements are each represented by their element stiffness matrix. Each spring is coupled with the adjacent spring via nodes. The mass of each element is distributed evenly between the two nodes. A helical gear mesh model is used to couple the two shafts between the corresponding nodes. Gear mesh coupling is represented by a linear spring connected between the two gear base circles acting along the plane of action. Each gear mass is attached to its corresponding node on the shaft. In addition to the linear spring coupling, the gear TE is also shown in series with the spring. Stiffness matrices are used to represent the roller bearings. They are added to the corresponding beam element nodes. Bearings are modelled as being attached to the rigid housing.

A detailed mathematical description of each element group (shaft elements, gear meshes, and bearings) is provided in the remainder of Chapter 3. Each section presents the formation of the stiffness and mass matrices for each element. Damping matrices are not derived because the damping values for each element are not known until the final stages of the

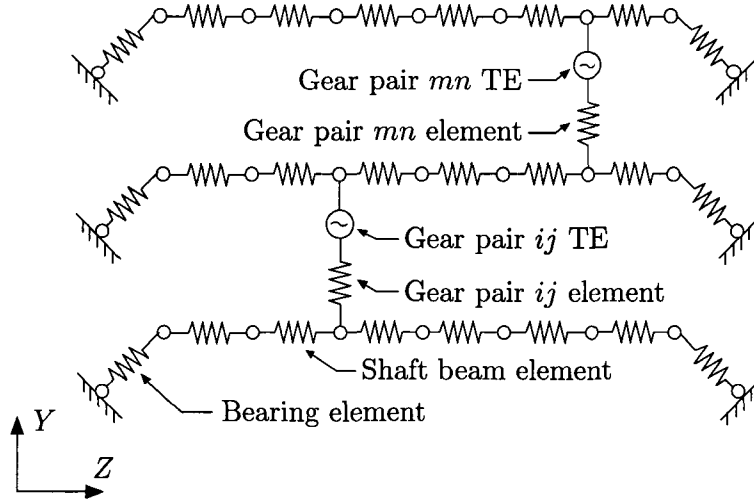


Figure 3.2: *Finite element representation of the gearbox.* Each shaft is divided into six beam elements whose end nodes possess six DOF. Each gear mesh is represented by a linear spring connected between the two gear base circles. In series with the spring, a displacement excitation in the form of the transmission error is included in the model as well.

design. Instead, proportional (modal) damping is used here. Before the mass and stiffness matrices are assembled, the definition of the 12x1 displacement vector $\left(\vec{X}_{ab}\right)$ for each finite element is obtained and is given by the following vector equation

$$\vec{X}_{ab} = \left[x_a \quad y_a \quad z_a \quad \theta_{xa} \quad \theta_{ya} \quad \theta_{za} \quad x_b \quad y_b \quad z_b \quad \theta_{xb} \quad \theta_{yb} \quad \theta_{zb} \right]^T, \quad (3.1.1)$$

where

x_a, y_a , and z_a = displacement of node a in x, y , and z directions, respectively,

x_b, y_b , and z_b = displacement of node b in x, y , and z directions, respectively,

θ_{xa}, θ_{ya} , and θ_{za} = angular displacement of node a about x, y , and z axis, respectively,

θ_{xb}, θ_{yb} , and θ_{zb} = angular displacement of node b about x, y , and z axis, respectively, and

superscript T = matrix transpose.

3.2 Finite Element Shaft Model

Shafts are modelled as straight, uniform, circular cross-section beam elements. They are able to resist axial, bending moment, and torsional loads. As a consequence of this assumption,

the resulting beam element possesses 12 DOF (six rotational and six translational DOF).

Figure 3.3 represents the beam element, its orientation in space, and applied forces.

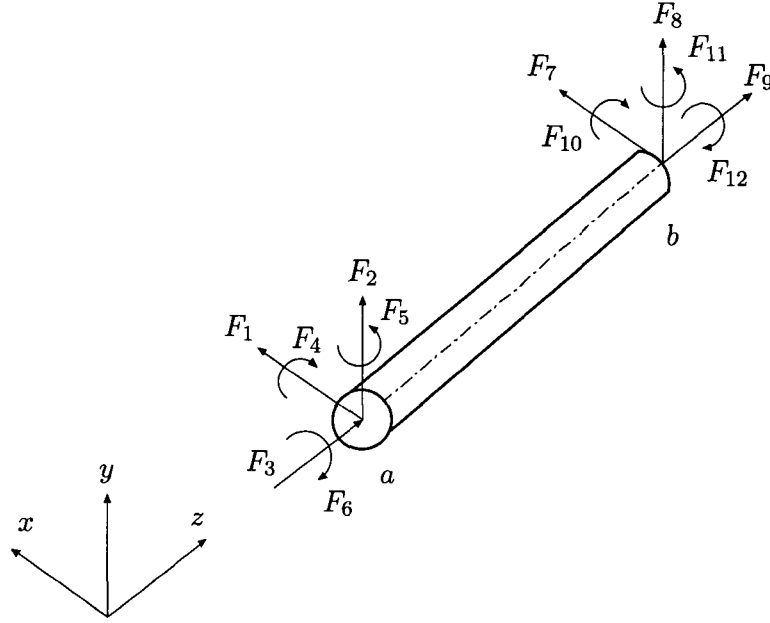


Figure 3.3: (Figure 5.4 in Przemieniecki[25]) *3D beam element*. The beam element is assumed to be a straight bar of a uniform cross-section. The bar is capable of resisting axial (F_3 and F_9), bending (F_4 , F_5 , F_{10} and F_{11}), torsional (F_6 and F_{12}) and shearing (F_1 , F_2 , F_7 and F_8) loads.

In accordance with the above element coordinate system and the engineering beam displacement theory, the following 12×12 $\left(\begin{bmatrix} k_s \end{bmatrix} \right)$ stiffness matrix (only upper-left 6×6 stiffness sub-matrix presented for clarity purposes) is derived (for a complete derivation consult Przemieniecki[25])

$$\begin{bmatrix} k_s \end{bmatrix} = \begin{bmatrix} \frac{12EI_y}{l^3(1+\phi_x)} & 0 & 0 & 0 & -\frac{6EI_y}{l^2(1+\phi_x)} & 0 & \dots \\ 0 & \frac{12EI_x}{l^3(1+\phi_y)} & 0 & \frac{6EI_x}{l^2(1+\phi_y)} & 0 & 0 & \dots \\ 0 & 0 & \frac{EA}{l} & 0 & 0 & 0 & \dots \\ 0 & \frac{6EI_x}{l^2(1+\phi_y)} & 0 & \frac{(4+\phi_y)EI_x}{l(1+\phi_y)} & 0 & 0 & \dots \\ -\frac{6EI_y}{l^2(1+\phi_x)} & 0 & 0 & 0 & \frac{(4+\phi_x)EI_y}{l(1+\phi_x)} & 0 & \dots \\ 0 & 0 & 0 & 0 & 0 & \frac{GJ}{l} & \dots \\ \vdots & \vdots & \vdots & \vdots & \vdots & \vdots & \ddots \end{bmatrix}, \quad (3.2.1)$$

where

A = cross-sectional area of a beam element,

G = modulus of rigidity,

I_x and I_y = moment of inertia about x and y axis, respectively,

J = polar moment of inertia,

l = length of a shaft element, and

ϕ_x and ϕ_y = shear deformation parameter in x and y directions, respectively.

The complete 12x12 $\left(\begin{bmatrix} k_s \end{bmatrix} \right)$ stiffness matrix is included in Appendix B. Parameters ϕ_x and ϕ_y are defined as

$$\phi_x = 24(1 + \nu) \frac{A}{A_{S_x}} \left(\frac{r_y}{l} \right)^2, \text{ and} \quad (3.2.2)$$

$$\phi_y = 24(1 + \nu) \frac{A}{A_{S_y}} \left(\frac{r_x}{l} \right)^2, \quad (3.2.3)$$

where

A_{S_x} and A_{S_y} = net shear effective area in x and y directions, respectively, and

r_x and r_y = radius of gyration about x and y axis, respectively.

If the ratios of the radius of gyration to element length are small when compared to unity, shear deformation parameters can be neglected (slender beams). If this is not the case, then the above deformation parameters should be included. For this purpose, the shear deflection constant is defined as the ratio of the actual beam cross-sectional area to the effective area resisting shear. Shear deflection constants for a number of common sections are: rectangle (6/5), solid circle (10/9) and hollowed (thin walled) circle (2). When circular cross-section beam elements are used, the element properties are identical in both x and y and direction. The presence of temperature gradients across the beam cross-section and along the length of the beam is neglected in the stiffness matrix formulation.

The inertial properties of a structural beam element could be constructed by either discrete or lumped mass element representations. Discrete (equivalent) mass matrices are the preferred route that one should take if a system with a relatively small number of DOF is analyzed. If that is not the case, the lumped mass approach is recommended. The lumped

mass approach does not conserve momentum and kinetic energy for the given system, but as the number of elements increases, it converges to a correct solution. In the case of the lumped mass approach, the element mass matrix is not dynamically coupled and only the diagonal terms are present. Due to this, computation of the inverse mass matrix is a trivial task and the result is still a diagonal matrix. The 12x12 mass matrix $\left(\begin{bmatrix} m_s \end{bmatrix} \right)$ for the circular cross-section beam element, using the lumped mass approach, is given as

$$\begin{bmatrix} m_s \end{bmatrix} = \left(\frac{\rho A l}{2} \right) \text{diag} \begin{bmatrix} 1 & 1 & 1 & \frac{1}{4}r_b^2 + \frac{1}{12}l^2 & \frac{1}{4}r_b^2 + \frac{1}{12}l^2 & \frac{1}{2}r_b^2 & \dots \\ \dots & 1 & 1 & 1 & \frac{1}{4}r_b^2 + \frac{1}{12}l^2 & \frac{1}{4}r_b^2 + \frac{1}{12}l^2 & \frac{1}{2}r_b^2 \end{bmatrix}, \quad (3.2.4)$$

where

diag = a diagonal matrix,

ρ = beam element mass density, and

r_b = radius of the shaft element.

3.3 Gear Mesh Model

This section as well as Section 3.4 of the thesis were developed in Kahraman et al.[15]. Both sections are presented because of their importance to the research. Prior to assembling the gear mesh stiffness matrix a few assumptions are in order:

- Sliding of the gear teeth and associated friction forces are neglected for a given gear pair.
- Tooth separation is not considered, and accordingly, the modelling of the gear backlash is not incorporated.
- Gyroscopic effects on gears are also not modelled.

The gear pair mesh model is represented with rigid gear bodies and compliant gear teeth. Tooth mesh stiffness is modelled as a linear spring of stiffness k_{ij} . This spring is positioned on the plane of action between the two gears and acts in the direction of the tooth normal. A 3D helical gear pair model is shown in Figure 3.4. Each gear possesses

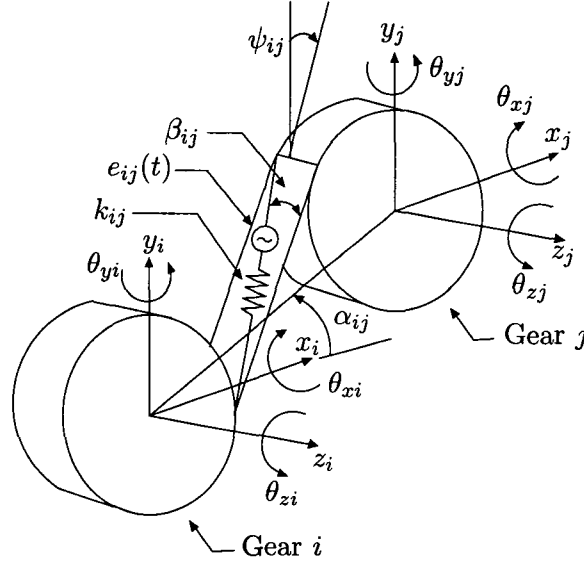


Figure 3.4: (Figure 2 in Kahraman et al.[15]) *3D helical gear pair model*. α_{ij} is the relative gear position angle and ψ_{ij} is the angle between the positive y axis and the plane of action. The helix angle β_{ij} is a function of the hand of gears and is positive if gear i has left hand teeth and negative otherwise.

six DOF and as a result a coupling between the two shafts holding the gears has 12 DOF. Before the stiffness matrix is finally assembled, two gear orientation parameters must be defined for proper overall system assembly. The angle ψ_{ij} is defined as the angle between the positive y axis and the plane of action and is given by the following formulae

$$\psi_{ij} = \begin{cases} \phi_{ij} - \alpha_{ij} & \text{if } T_i \text{ is counterclockwise (CCW)} \\ -(\phi_{ij} + \alpha_{ij}) & \text{if } T_i \text{ is clockwise (CW)} \end{cases}, \quad (3.3.1)$$

where

ϕ_{ij} = transverse operating pressure angle of gear pair ij ,

α_{ij} = relative angular position of gear pair ij , and

T_i = torque applied to gear i .

The helix angle β_{ij} is a function of the hand of gears and is positive if i gear has left hand teeth and negative otherwise. In the case of multiple gear meshes, the more general formula for $\psi_{(i)(i+1)}$ is given as

$$\psi_{(i)(i+1)} = \begin{cases} (-1)^{\left(\frac{i+3}{2}\right)} \phi_{(i)(i+1)} - \alpha_{(i)(i+1)} & \text{if } T_1 \text{ is CCW} \\ (-1)^{\left(\frac{i+1}{2}\right)} \phi_{(i)(i+1)} - \alpha_{(i)(i+1)} & \text{if } T_1 \text{ is CW} \end{cases}. \quad (3.3.2)$$

Once the above two terms are defined, then the equations of motion for gear pair ij are

$$m_i \ddot{x}_i + k_{ij} p_{ij}(t) \cos(\beta_{ij}) \sin(\psi_{ij}) = 0, \quad (3.3.3)$$

$$m_i \ddot{y}_i + k_{ij} p_{ij}(t) \cos(\beta_{ij}) \cos(\psi_{ij}) = 0, \quad (3.3.4)$$

$$m_i \ddot{z}_i - k_{ij} p_{ij}(t) \sin(\beta_{ij}) = 0, \quad (3.3.5)$$

$$I_i \ddot{\theta}_{xi} + r_{bi} k_{ij} p_{ij}(t) \sin(\beta_{ij}) \sin(\psi_{ij}) = 0, \quad (3.3.6)$$

$$I_i \ddot{\theta}_{yi} + r_{bi} k_{ij} p_{ij}(t) \sin(\beta_{ij}) \cos(\psi_{ij}) = 0, \quad (3.3.7)$$

$$J_i \ddot{\theta}_{zi} + r_{bi} k_{ij} p_{ij}(t) \cos(\beta_{ij}) = T_i, \quad (3.3.8)$$

$$m_j \ddot{x}_j - k_{ij} p_{ij}(t) \cos(\beta_{ij}) \sin(\psi_{ij}) = 0, \quad (3.3.9)$$

$$m_j \ddot{y}_j - k_{ij} p_{ij}(t) \cos(\beta_{ij}) \cos(\psi_{ij}) = 0, \quad (3.3.10)$$

$$m_j \ddot{z}_j + k_{ij} p_{ij}(t) \sin(\beta_{ij}) = 0, \quad (3.3.11)$$

$$I_j \ddot{\theta}_{xj} + r_{bj} k_{ij} p_{ij}(t) \sin(\beta_{ij}) \sin(\psi_{ij}) = 0, \quad (3.3.12)$$

$$I_j \ddot{\theta}_{yj} + r_{bj} k_{ij} p_{ij}(t) \sin(\beta_{ij}) \cos(\psi_{ij}) = 0, \text{ and} \quad (3.3.13)$$

$$J_j \ddot{\theta}_{zj} + r_{bj} k_{ij} p_{ij}(t) \cos(\beta_{ij}) = -T_j, \quad (3.3.14)$$

where

m_i and m_j = mass of gears i and j , respectively,

\ddot{x}_i , \ddot{y}_i , and \ddot{z}_i = acceleration of gear i in x , y , and z directions, respectively,

\ddot{x}_j , \ddot{y}_j , and \ddot{z}_j = acceleration of gear j in x , y , and z directions, respectively,

k_{ij} = mesh stiffness of gear pair ij ,

t = time,

$p_{ij}(t)$ = relative displacement of gear mesh ij ,

I_i and I_j = moment of inertia of gears i and j , respectively,

$\ddot{\theta}_{xi}$, $\ddot{\theta}_{yi}$, and $\ddot{\theta}_{zi}$ = angular acceleration of gear i about x , y , and z axis, respectively,

$\ddot{\theta}_{xj}$, $\ddot{\theta}_{yj}$, and $\ddot{\theta}_{zj}$ = angular acceleration of gear j about x , y , and z axis, respectively,

r_{bi} = base circle radius of gear i ,

J_i and J_j = polar moment of inertia of gears i and j , respectively, and

T_j = torque applied to gear j .

In the above equations, a relative displacement of gear mesh ij in a direction normal to teeth contact surfaces is defined as

$$\begin{aligned} p_{ij}(t) = & (x_i \sin(\psi_{ij}) - x_j \sin(\psi_{ij}) + y_i \cos(\psi_{ij}) - y_j \cos(\psi_{ij}) + r_{bi} \theta_{zi} \dots \\ & \dots + r_{bj} \theta_{zj}) \cos(\beta_{ij}) + (z_j - z_i + r_{bi} \theta_{xi} \sin(\psi_{ij}) + r_{bj} \theta_{xj} \sin(\psi_{ij}) \dots \\ & \dots + r_{bi} \theta_{yi} \cos(\psi_{ij}) + r_{bj} \theta_{yj} \cos(\psi_{ij})) \sin(\beta_{ij}) - e_{ij}(t), \end{aligned} \quad (3.3.15)$$

where

x_i, y_i , and z_i = displacement of gear i in x, y , and z directions, respectively,

x_j, y_j , and z_j = displacement of gear j in x, y , and z directions, respectively,

θ_{xi}, θ_{yi} , and θ_{zi} = angular displacement of gear i about x, y , and z axis, respectively, and

θ_{xj}, θ_{yj} , and θ_{zj} = angular displacement of gear j about x, y , and z axis, respectively.

From the above equations (Equation 3.3.3 through Equation 3.3.15), the stiffness matrix $\left(\begin{bmatrix} k_g \end{bmatrix} \right)$ that couples the two shafts holding the gears is obtained as

$$\begin{bmatrix} k_g \end{bmatrix} = k_{ij} \begin{bmatrix} \cos(\beta_{ij}) \sin(\psi_{ij}) (\sin(\psi_{ij}) \cos(\beta_{ij}) - e_{ij}(t)) & \dots \\ \cos(\beta_{ij}) \cos(\psi_{ij}) (\sin(\psi_{ij}) \cos(\beta_{ij}) - e_{ij}(t)) & \dots \\ \vdots & \ddots \end{bmatrix}, \quad (3.3.16)$$

In the above matrix, the gear pair mesh stiffness (k_{ij}) is obtained from the gear pair finite element model in ANSYS and its time average value will be used in the model. Experimental validation of this assumption is offered in Kahraman et al.[15]. The STE is also obtained from the ANSYS model.

As mentioned in Section 3.1, the mass of each gear is attached to its corresponding shaft node. Again, this offers a numerical advantage when compared to the distributed mass approach. The mass matrix (Equation 3.2.4) obtained in Section 3.2 is also used here. In this case, mass term in front of the matrix is not divided by two (each gear is attached to its corresponding node). Also, the moments of inertia formulae should be changed from solid cylinder formulae (shafts in this model) to hollow cylinder formulae (gears in the model). The resulting gear mass matrix $\left(\begin{bmatrix} m_g \end{bmatrix} \right)$ is given as

$$\begin{bmatrix} m_g \end{bmatrix} = (\rho A w) \text{diag} \begin{bmatrix} 1 & 1 & 1 & \frac{1}{12}(3r_p^2 + 3r_h^2 + w^2) & \frac{1}{12}(3r_p^2 + 3r_h^2 + w^2) & \frac{1}{2}(r_p^2 + r_h^2) & \dots \\ \dots & 1 & 1 & 1 & \frac{1}{12}(3r_p^2 + 3r_h^2 + w^2) & \frac{1}{12}(3r_p^2 + 3r_h^2 + w^2) & \frac{1}{2}(r_p^2 + r_h^2) \end{bmatrix}, \quad (3.3.17)$$

where

w = gear face width,

r_p = pitch radius,

r_h = hub radius, and

$$A = \pi(r_p^2 - r_h^2).$$

3.4 Load Vector

There are two possible sources of excitation in any gearbox system[22]. First, there is a so-called external excitation. Rotating mass unbalance, geometric eccentricities, and prime mover or load torque fluctuations all fall into this category. Manufacturing related profile and spacing errors and the elastic deformation of teeth, shafts, and bearings are all considered to be an internal type of excitation. These are typically high frequency excitations and are the major noise sources in gearbox systems. In this research, the only excitation comes in the form of the STE displacement excitation due to gear teeth elasticity. The effect of a time-varying mesh stiffness is included in the model by the use of the sinusoidal STE displacement function. This approach has been widely used in helical gear dynamic studies[15], and in some cases, in spur gear dynamic studies[16]. A development of the forcing vector for multi-mesh excitations is given next.

The alternating force vector $\left(\vec{F}(t)\right)$ is identified in terms of all $(N_s - 1)$ static transmission error excitations as

$$\vec{F}(t) = \sum_{i=1,3,5}^{2N_s-3} \vec{F}_{(i)(i+1)}, \quad (3.4.1)$$

where

$\vec{F}_{(i)(i+1)}$ = extended forcing vector, and

N_s = number of shafts.

The extended forcing vector is obtained by the use of Equations 3.3.3 through Equation 3.3.14. In these equations, p_{ij} represents the relative displacement at the gear mesh. Static transmission error is the relative displacement at the gear mesh which is multiplied

by mesh stiffness (k_{ij}) to obtain the force ($\vec{F}_{(i)(i+1)}$) acting in a direction normal to teeth contacting surfaces

$$\vec{F}_{(i)(i+1)} = k_{ij} p_{ij}(t). \quad (3.4.2)$$

For multiple gear meshes, a phase relationship between multiple excitations needs to be defined. The STE is defined in Fourier series form as

$$e_{(i)(i+1)}(t) = \sum_{r=1}^R \tilde{e}_{(i)(i+1)r} \sin [r\omega_{(i)(i+1)}t + \Gamma_{(i)(i+1)r} + r\Pi_{(i)(i+1)}], \quad (3.4.3)$$

where

$\tilde{e}_{(i)(i+1)r}$ = r -th harmonic amplitude (obtained from ANSYS model),

$\omega_{(i)(i+1)}$ = frequency of gear mesh ij ,

$\Gamma_{(i)(i+1)r}$ = r -th harmonic phase angle, and

$\Pi_{(i)(i+1)}$ = phase angle difference between the $e_{(i)(i+1)}(t)$ and $e_{12}(t)$.

To define the last term in Equation 3.4.3, Figures 3.5 and Figures 3.6 are used. Based on these figures

$$\Pi_{(i)(i+1)} = \sum_{j=1,3,5}^i N_j [\bar{\alpha}_{(j)(j+1)} - \gamma_{(j-1)(j)}]. \quad (3.4.4)$$

The first angle in square brackets above is obtained according to Figure 3.5 as

$$\bar{\alpha}_{(j)(j+1)} = \pi - \alpha_{(j)(j+1)} + \alpha_{(j-2)(j-1)}. \quad (3.4.5)$$

The second angle in the Equation 3.4.4 ($\gamma_{(j-1)(j)}$) is attained via use of Figure 3.6. It is an angle between the reference teeth of gears $(j-1)$ and (j) mounted on the same shaft.

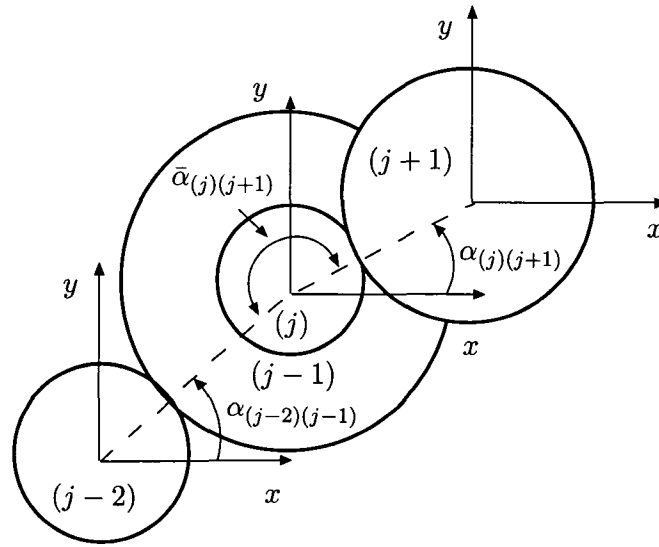


Figure 3.5: (Figure 3 in Kahraman et al.[15]) *Shaft position angle definition.* Definition of the shaft position angle for multiple TE excitations.

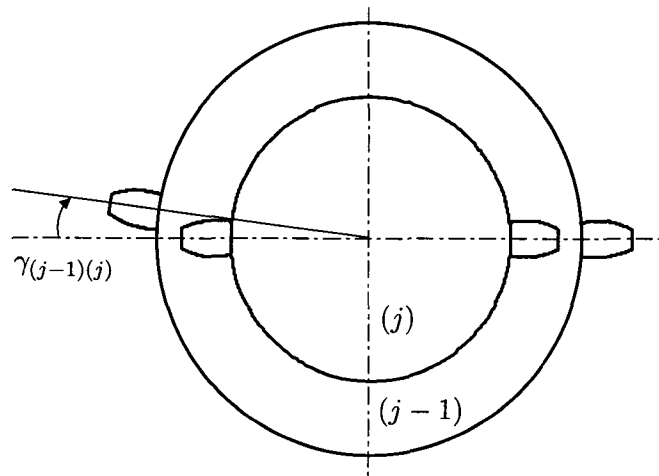


Figure 3.6: (Figure 4 in Kahraman et al.[15]) *Phase angle definition.* The definition of the phase angle for multiple TE excitations. More specifically, this figure takes into account teeth alignment between the gears mounted on the same shaft.

3.5 Bearing Model

Bearing behaviour is assumed to be linear. This assumption is valid in cases where the bearings are preloaded. In the majority of automotive gearboxes, bearings are preloaded, and as a result are modelled as being linear. Tapered roller bearings are assumed in all three shafts modelled. The following bearing stiffness matrix $\left(\begin{bmatrix} k_b \end{bmatrix} \right)$ is used

$$\begin{bmatrix} k_b \end{bmatrix} = \text{diag} \begin{bmatrix} k_x & k_y & k_z & k_{\theta x} & k_{\theta y} & 0 \end{bmatrix}, \quad (3.5.1)$$

where

k_x , k_y , and k_z = bearing stiffness in x , y , and z directions, respectively, and

$k_{\theta x}$ and $k_{\theta y}$ = bearing stiffness about x and y directions, respectively.

There are no off diagonal terms, therefore there is no coupling between the individual DOF. The terms in the above matrix will be assumed based on previous publications because the actual bearing numbers are difficult to obtain. There are more accurate bearing models, but they require knowledge of additional bearing parameters that are also difficult to obtain. Most of these extended models are used to study the effects of gear vibration on the gearbox housing. This is not the primary objective of this thesis; therefore a simpler model was chosen. In addition, bearing mass is neglected, and as a result, the bearing mass matrix does not exist.

3.6 Overall System Assembly

This section is divided into two parts. The first part describes the derivation used to obtain the relationship between the local and global coordinate system for any general finite element. The second part describes the standard finite element procedure for assembling the overall system equation of motion.

3.6.1 Coordinate Transformation

Prior to assembling equations of motion for the overall system, the relationship between the local and global coordinate system for each finite element has to be established. In preceding sections, the stiffness, mass, displacement and force matrices were all derived in

a body fixed local coordinate system. Their transformation into a global coordinate system is essential for proper system model assembly. To obtain a matrix relationship between the element displacement \vec{x} in the local system and the element displacement \vec{X} in the global system the following matrix equation is used

$$\vec{x} = \begin{bmatrix} T \end{bmatrix} \vec{X}, \quad (3.6.1)$$

where

$$\begin{bmatrix} T \end{bmatrix} = \text{transformation matrix.}$$

The structure of this matrix will be shown at the end of this section. If virtual displacements (δ_v) are introduced on an element, the following equation is obtained

$$\delta_v \vec{x} = \begin{bmatrix} T \end{bmatrix} \delta_v \vec{X}. \quad (3.6.2)$$

The resulting virtual work (scalar quantity) is independent of the coordinate system, therefore

$$\delta_v \vec{X}^T \vec{F} = \delta_v \vec{x}^T \vec{f}, \quad (3.6.3)$$

where

\vec{F} and \vec{f} = force vector in global and local coordinates, respectively.

Substituting Equation 3.6.1 into the above equation, the following is obtained

$$\delta_v \vec{X}^T \left(\vec{F} - \begin{bmatrix} T \end{bmatrix}^T \vec{f} \right) = 0. \quad (3.6.4)$$

Because $\delta_v \vec{X}$'s are arbitrary, it follows that

$$\left(\vec{F} - \begin{bmatrix} T \end{bmatrix}^T \vec{f} \right) = 0. \quad (3.6.5)$$

If it is recognized that

$$\vec{f} = \begin{bmatrix} m \end{bmatrix} \vec{\tilde{x}} + \begin{bmatrix} k \end{bmatrix} \vec{x}, \quad (3.6.6)$$

and by substitution of this identity and Equation 3.6.1 into the Equation 3.6.5, local to global transformation for any general element is obtained in the following manner

$$\begin{bmatrix} T \end{bmatrix}^T \begin{bmatrix} m \end{bmatrix} \begin{bmatrix} T \end{bmatrix} \vec{X} + \begin{bmatrix} T \end{bmatrix}^T \begin{bmatrix} k \end{bmatrix} \begin{bmatrix} T \end{bmatrix} \vec{X} = \vec{F}, \quad (3.6.7)$$

where

- $\begin{bmatrix} m \end{bmatrix}$ = element mass matrix in local coordinates,
- $\vec{\ddot{x}}$ and $\vec{\ddot{X}}$ = element acceleration vector in local and global coordinates, respectively, and
- $\begin{bmatrix} k \end{bmatrix}$ = element stiffness matrix in local coordinates.

The transformation matrix $\begin{bmatrix} T \end{bmatrix}$ for any element is formed from the direction cosines for that element and its structure is as follows

$$\begin{bmatrix} T \end{bmatrix} = \begin{bmatrix} \tau & 0 & 0 & 0 \\ 0 & \tau & 0 & 0 \\ 0 & 0 & \tau & 0 \\ 0 & 0 & 0 & \tau \end{bmatrix}, \quad (3.6.8)$$

where

τ = 3x3 direction cosine sub-matrix, and

0 = 3x3 zero matrix.

Figure 3.7 shows the local and global coordinate frames. Based on Figure 3.7, the following 3x3 direction cosine sub-matrix relating local to global coordinate frames is obtained

$$\begin{bmatrix} \tau \end{bmatrix} = \begin{bmatrix} \cos(\theta_{Xx}) & \cos(\theta_{Yx}) & \cos(\theta_{Zx}) \\ \cos(\theta_{Xy}) & \cos(\theta_{Yy}) & \cos(\theta_{Zy}) \\ \cos(\theta_{Xz}) & \cos(\theta_{Yz}) & \cos(\theta_{Zz}) \end{bmatrix}. \quad (3.6.9)$$

In this thesis, the local coordinate system for every element coincides with the global coordinate system and as a consequence, the transformation matrix is just a 12x12 identity matrix.

3.6.2 Finite Element Model Assembly Procedure

Once each structural element is defined in terms of their stiffness and mass matrices in the global coordinate system, they all have to be combined and assembled into an overall equation of motion for the model. To show the assembly procedure, a simple example of two spring elements connected in series is presented (Figure 3.8). This simple structure has two elements, three nodes, three DOF, and no specific boundary conditions. Element numbers are enclosed in triangles while the node numbers are enclosed in circles. Applying static

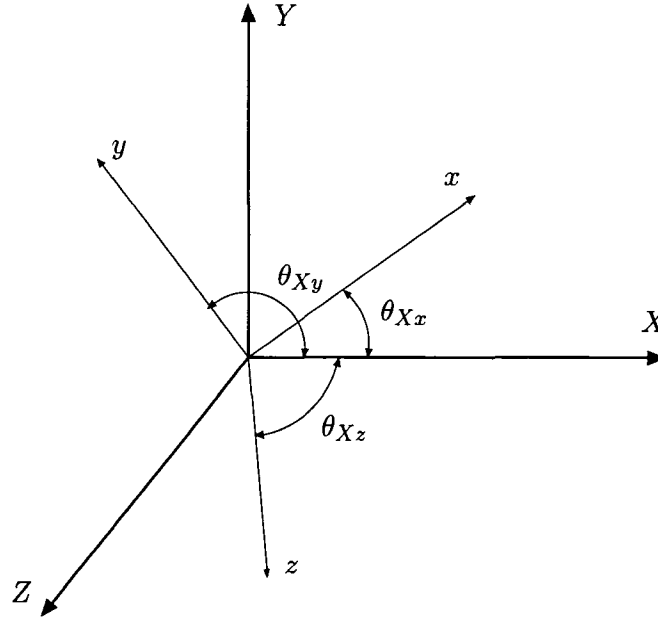


Figure 3.7: *Local and global coordinate frames.* The $X-Y-Z$ represents global coordinate frame, while the $x-y-z$ represents local coordinate frame. Angles relating the local reference frame to the X axis of global frame are shown only.

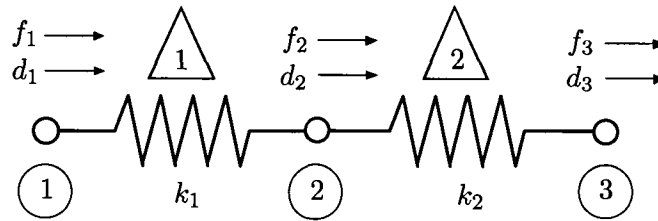


Figure 3.8: (Figure 2.5.1 in Altenhof and Zamani[3]) *Spring elements.* Element numbers are enclosed in triangles while the node numbers are enclosed in circles. Element stiffnesses are shown as k_1 and k_2 . Nodal forces are f_1 , f_2 , and f_3 , while the node displacements are d_1 , d_2 , and d_3 .

equilibrium equations to all three nodes results in the following system of linear equations

$$\begin{aligned} k_1(d_1 - d_2) &= f_1 \\ -k_1(d_1 - d_2) + k_2(d_2 - d_3) &= f_2, \\ -k_2(d_2 - d_3) &= f_3 \end{aligned} \tag{3.6.10}$$

where

k_1 and k_2 = stiffness of element 1 and 2, respectively,

d_1 , d_2 , and d_3 = displacement of node 1, 2, and 3, respectively, and

f_1 , f_2 , and f_3 = force acting on node 1, 2, and 3, respectively.

These equations can then be rewritten in the matrix form as follows

$$\begin{bmatrix} k_1 & -k_1 & 0 \\ -k_1 & k_1 + k_2 & -k_2 \\ 0 & -k_2 & k_2 \end{bmatrix} \begin{Bmatrix} d_1 \\ d_2 \\ d_3 \end{Bmatrix} = \begin{Bmatrix} f_1 \\ f_2 \\ f_3 \end{Bmatrix}. \tag{3.6.11}$$

The stiffness matrix in the above equation is obtained via superposition of the stiffness matrices for individual elements. Top left 2x2 matrix contained within the global stiffness matrix represents element 1, while the bottom right 2x2 matrix represents element 2. To assemble the global stiffness matrix for a more general case, the use of connectivity tables is utilized. For the example presented here, the connectivity table is given in Table 3.1. The

Table 3.1: *Connectivity table.* Example connectivity table for overall system stiffness matrix assembly. It relates local element nodes to the global node numbers.

Element	Local node 1	Local node 2	Stiffness
1	1	2	k_1
2	2	3	k_2

global stiffness matrix is symmetric and singular. This is expected because no boundary conditions are assigned to the structure. For dynamic systems, in addition to the global

stiffness matrix, assembly of the global mass matrix is also needed. For this purpose, the same connectivity table is used. As mentioned earlier, the model developed in this thesis assumes proportional damping for the system, therefore, element damping matrices do not exist. For the systems that have damping included, the same connectivity table would be used. With the use of the connectivity tables, the equation of motion for the overall system is assembled. In the gearbox analyzed here, bearing, shaft and gear nodes all have six DOF resulting in relatively large overall mass and stiffness matrices.

3.7 Solution Methodology

Both analytical and numerical methods are used to perform structural analysis. If a simple structural configuration is analyzed, the analytical method is possible. For more complex structures, numerical methods are more practical. Two types of numerical methods exist. They include the numerical solution of differential equations, and matrix methods based on the discrete element idealization. In numerical solutions of differential equations, the equations of elasticity are solved by either direct numerical integration or by finite difference techniques. Practical limitations restrict these approaches to simple structures. The equations in the two numerical techniques could be cast into the matrix notation and the matrix algebra could be applied to obtain the solution, but these techniques are generally not referred to as matrix methods.

In matrix based methods, the structure is first idealized into an assembly of discrete structural elements with assumed stress distribution and displacement. To obtain a complete solution, these individual displacements and stresses are combined in a way that satisfies the force equilibrium and displacement compatibility at the nodes between the elements. This approach lends itself for use in complex structure analysis. The matrix method can further be classified as either the displacement method or the force method. In the first case, the displacements are chosen as unknowns, while in the other approach, the forces are solved for.

In this research, the matrix displacement method is employed. To solve for the unknown displacements, the modal summation technique is used. Before the modal summation technique is discussed, discussion of damping models is in order. It is important to understand the limitations that come from the use of modal damping in structural analysis. Again, the gearbox model analyzed here is using modal damping values rather than the element damping matrices.

Damping, in simple words, usually refers to the dissipation of vibratory energy in solids or structures over time. Vibratory energy contains a combination of kinetic and potential energy. The dissipation process involves conversion of vibratory energy into thermal energy. The higher the conversion rate, the higher the damping is for that particular structure. There are two approaches that one could take to obtain damping values for a structure. The first approach involves direct damping measurements, which guarantees accurate results, but is not usually feasible because the structure has to be built first. In the second approach, mathematical models are built to describe damping. The three most common types of damping are viscous, dry friction, and hysteretic[8].

Viscous damping is a common form of damping found in many engineering systems. The damping force is proportional to the velocity. This damping approach leads to the simplest mathematical formulation for a given model. Due to this, more complicated damping models are sometimes approximated as being viscous. The free vibration of dynamic structures with viscous damping is easily identified by an exponential decay of the oscillation.

Coulomb or dry friction damping is present when a relative motion between the two adjacent members takes place. These friction forces are independent of the amplitude and frequency. The magnitude of the friction forces can be considered constant. In this case, the free vibration oscillation decay is a linear function of time. Many real structures possess a combination of viscous and dry damping, resulting in combined vibration decay. The actions of two damping mechanisms are sometimes amplitude dependent resulting in initial exponential function, followed by the linear decay function.

When solid materials or structures are subjected to the cyclic stressing, the damping force developed within the structure is frequency dependent. This phenomenon is referred to as the hysteretic damping. Hysteretic damping is mainly due to the hysteresis properties of materials. Another source of hysteresis damping comes from friction between the joints of structural components. Viscous damping forces are independent of the frequency of oscillations, therefore the viscous damping model is not suitable for modelling of internal damping of structures. The energy loss per cycle for hysteretic and friction damping is independent of frequency, while for viscous damping the opposite is true. Hysteretic damping and the structure stiffness are not usually easily separated. Mathematical models account for this fact by using of complex stiffnesses. Complex stiffness is equal to the sum of the static stiffness and hysteretic damping loss factor. Example values for the damping loss factors are available in literature, but are highly dependent on the mechanism associated with the internal reconstruction such as molecular dissociation and stress changes at grain boundaries. These damping effects are non-linear and variable within a material and, as a result, the analysis of these damping mechanisms is complicated. To obtain the energy dissipated at various strain levels for a specific material sample, experimental measurement techniques must be used.

The common approach used in structural analysis is to use the special type of viscous damping called proportional or modal damping. The advantages of using of this type of damping are the ease of use in the analysis and the fact that modes of the structure are almost identical to those of the undamped model. The modal damping model expresses the damping as a linear combination of the mass and stiffness matrices. This type of damping is also referred to as Rayleigh damping. To obtain the modal properties of the overall system, the undamped version of the model is analyzed first, and then corrections are made for the presence of damping. This approach is acceptable as long as the system's modes remain real. In case of real structures, the amount of damping is small, so the imaginary part is small when compared to the real part. Caughey and O'Kelly[10] have proved that a damped linear system possesses the same modes as the undamped counterpart if the following

is satisfied

$$\begin{bmatrix} M \end{bmatrix}^{-1} \begin{bmatrix} K \end{bmatrix} \begin{bmatrix} M \end{bmatrix}^{-1} \begin{bmatrix} C \end{bmatrix} = \begin{bmatrix} M \end{bmatrix}^{-1} \begin{bmatrix} C \end{bmatrix} \begin{bmatrix} M \end{bmatrix}^{-1} \begin{bmatrix} K \end{bmatrix}, \quad (3.7.1)$$

where

$$\begin{aligned} \begin{bmatrix} M \end{bmatrix} &= \text{mass matrix,} \\ \begin{bmatrix} K \end{bmatrix} &= \text{stiffness matrix, and} \\ \begin{bmatrix} C \end{bmatrix} &= \text{damping matrix.} \end{aligned}$$

However, the main limitation of this model still remains, because the variation of the of damping factors with respect to vibration frequency is not accurately modelled. Adhikari[2] developed a proportional damping model that captured the frequency variation of the damping factors. The proposed model requires the measurement of natural frequencies and modal damping values. Again, measurement is needed to obtain the modal damping values, and therefore not feasible for use in this thesis. Instead, modal damping values will be estimated based on the published data and will be used directly without the formation of damping matrices.

3.7.1 Modal Summation

Once the overall system model is formed, one must choose the appropriate solution technique to solve for the desired quantities. The modal summation technique was chosen here because it offers frequency dependent results, and is capable of dealing with large size systems. A derivation of the modal summation technique[14] via use of the undamped MDOF system is presented next.

The equation of motion for forced response undamped MDOF system is given as

$$\begin{bmatrix} M \end{bmatrix} \ddot{\vec{X}}(t) + \begin{bmatrix} K \end{bmatrix} \vec{X}(t) = \vec{F}(t). \quad (3.7.2)$$

To obtain the modal model of the above equation, the free response of the system is considered, or $\vec{F}(t) = 0$. Next, assume the solution of the following form

$$\vec{X}(t) = \vec{X}e^{j\omega t}, \quad (3.7.3)$$

where

e = natural number,

j = imaginary number, and

ω = vibrating frequency.

The above is true if the whole system is capable of vibrating at a single frequency. Substitution of Equation 3.7.3 into Equation 3.7.2 leads to

$$\left(\begin{bmatrix} K \end{bmatrix} - \omega^2 \begin{bmatrix} M \end{bmatrix} \right) \vec{X} e^{j\omega t} = 0. \quad (3.7.4)$$

The only non-trivial solution to this equation is given as

$$\det \left| \begin{bmatrix} K \end{bmatrix} - \omega^2 \begin{bmatrix} M \end{bmatrix} \right| = 0. \quad (3.7.5)$$

When the determinant in Equation 3.7.5 is expanded, a polynomial in terms of ω^2 is obtained. This equation is known as the characteristic equation, and if $\omega^2 = \lambda$, the values of λ are known as the eigenvalues of the system. Substituting any of the eigenvalues back into Equation 3.7.4 yields a corresponding set of relative values for \vec{X} . These vectors are usually referred to as eigenvectors. The eigenvalues form a diagonal matrix, while the eigenvectors form a square matrix. These two matrices represent the system's modal model. A number of different procedures are available that take a system's spatial model and transform it into the modal model. The eigenvalue matrix is unique, while the eigenvector matrix is not unique, and is subject to an indeterminate scaling factor. The size of the scaling factor depends on the solution procedure used.

Before proceeding, it is important to examine orthogonality of the modal model.

$$\begin{bmatrix} \Psi \end{bmatrix}^T \begin{bmatrix} M \end{bmatrix} \begin{bmatrix} \Psi \end{bmatrix} = \begin{bmatrix} M_s \end{bmatrix}, \quad (3.7.6)$$

where

$$\begin{bmatrix} \Psi \end{bmatrix} = \text{modal matrix, and} \\ \begin{bmatrix} M_s \end{bmatrix} = \text{modal mass matrix.}$$

The same transformation is used to obtain the modal stiffness matrix (diagonal). As mentioned before, these two matrices are not unique, but the ratio of the stiffness over the mass

matrix is unique and is equal to the eigenvalue matrix. Many eigenvalue extraction routines scale each eigenvector so that the largest magnitude is equal to one. For modal modelling purposes, mass normalized eigenvectors are desirable. They possess the following properties

$$\begin{bmatrix} \Phi \end{bmatrix}^T \begin{bmatrix} M \end{bmatrix} \begin{bmatrix} \Phi \end{bmatrix} = \begin{bmatrix} I \end{bmatrix}, \quad (3.7.7)$$

where

$$\begin{bmatrix} \Phi \end{bmatrix} = \text{mass normalized modal matrix, and} \\ \begin{bmatrix} I \end{bmatrix} = \text{identity matrix.}$$

Premultiplying mass matrix with the eigenvector matrix transpose, and postmultiplying it with the eigenvector matrix results in an identity matrix (Equation 3.7.7). If the same transformation is applied to the stiffness matrix, a diagonal eigenvalue matrix is obtained. The relationship between the mass normalized and general eigenvector matrix is

$$\begin{bmatrix} \Phi \end{bmatrix} = \begin{bmatrix} \Psi \end{bmatrix} \begin{bmatrix} M_s \end{bmatrix}^{-\frac{1}{2}}. \quad (3.7.8)$$

Now that the modal model is defined and its orthogonal properties are identified, the forced response of the system is considered next. The system is excited by sinusoidal input at the same frequency, with various amplitudes and phases

$$\vec{F}(t) = \vec{F}e^{j\omega t}. \quad (3.7.9)$$

Again, the solution is assumed as

$$\vec{X}(t) = \vec{X}e^{j\omega t}. \quad (3.7.10)$$

Then the equation of motion becomes

$$\left(\begin{bmatrix} K \end{bmatrix} - \omega^2 \begin{bmatrix} M \end{bmatrix} \right) \vec{X}e^{j\omega t} = \vec{F}e^{j\omega t}. \quad (3.7.11)$$

To solve for the response, the following is used

$$\vec{X} = \left(\begin{bmatrix} K \end{bmatrix} - \omega^2 \begin{bmatrix} M \end{bmatrix} \right)^{-1} \vec{F}. \quad (3.7.12)$$

This can be simplified as

$$\vec{X} = \begin{bmatrix} \Omega(\omega) \end{bmatrix} \vec{F}, \quad (3.7.13)$$

where

$$\begin{bmatrix} \Omega \end{bmatrix} = \text{receptance matrix for the system.}$$

It is possible to determine values for the receptance matrix at any frequency by substituting the values into the above equation and inverting the system matrix. As the system size increases, this technique becomes too costly. For this and other reasons, an alternative means of solving the receptance matrix is used. This technique makes use of the modal properties of the system and is referred to as the modal summation technique. Equation 3.7.12 can be written as

$$\left(\begin{bmatrix} K \end{bmatrix} - \omega^2 \begin{bmatrix} M \end{bmatrix} \right) = \begin{bmatrix} \Omega(\omega) \end{bmatrix}^{-1}. \quad (3.7.14)$$

Next, premultiplying both sides by $\begin{bmatrix} \Phi \end{bmatrix}^T$ and postmultiplying by $\begin{bmatrix} \Phi \end{bmatrix}$ gives

$$\begin{bmatrix} \Phi \end{bmatrix}^T \left(\begin{bmatrix} K \end{bmatrix} - \omega^2 \begin{bmatrix} M \end{bmatrix} \right) \begin{bmatrix} \Phi \end{bmatrix} = \begin{bmatrix} \Phi \end{bmatrix}^T \begin{bmatrix} \Omega(\omega) \end{bmatrix}^{-1} \begin{bmatrix} \Phi \end{bmatrix}. \quad (3.7.15)$$

When simplified, the above equation results in a diagonal matrix

$$\begin{bmatrix} (\lambda - \omega^2) \end{bmatrix} = \begin{bmatrix} \Phi \end{bmatrix}^T \begin{bmatrix} \Omega(\omega) \end{bmatrix}^{-1} \begin{bmatrix} \Phi \end{bmatrix}. \quad (3.7.16)$$

The receptance matrix is then given as

$$\begin{bmatrix} \Omega(\omega) \end{bmatrix} = \frac{\begin{bmatrix} \Phi \end{bmatrix} \begin{bmatrix} \Phi \end{bmatrix}^T}{\begin{bmatrix} (\lambda - \omega^2) \end{bmatrix}}. \quad (3.7.17)$$

To solve for the response, transform the above equation into the following

$$\vec{X} = \frac{\begin{bmatrix} \Phi \end{bmatrix} \begin{bmatrix} \Phi \end{bmatrix}^T}{\begin{bmatrix} (\lambda - \omega^2) \end{bmatrix}} \vec{F}. \quad (3.7.18)$$

This is the most general form of the modal summation equation. When rotating structures and modal damping values are included in the model (gearbox), the modal summation response equation takes the following explicit form

$$\vec{X} = \sum_{i=1,3,5}^{2N_s-3} \sum_{r=1}^R \sum_{s=1}^q \frac{\vec{\Phi}_s \vec{\Phi}_s^T}{\left(\omega_s^2 - r^2 \omega_{(i)(i+1)}^2 + 2jr\zeta_s \omega_s \omega_{(i)(i+1)} \right)} \vec{F}, \quad (3.7.19)$$

where

r = transmission error harmonic,

R = total number of transmission error harmonics,

s = mode number,

q = total number of degrees of freedom,

$\vec{\Phi}_s$ = modal vector,

ω_s = natural frequency associated with $\vec{\Phi}_s$ modal vector, and

ζ_s = modal damping value.

Chapter 4

Results and Discussion

Before presenting the results, the following assumptions regarding the model developed here are given in Chapter 3 and are repeated here:

- A linear time invariant helical gear mesh model is employed.
- Sliding of the gear teeth and associated friction forces are neglected for all gear pairs.
- Tooth separation is not considered, and accordingly, the model does not consider the backlash phenomenon.
- Gyroscopic effects on gears are not included in the model.

Also, the response to the geometric eccentricities and mass unbalances of the gears and shafts is not included here. The aforementioned balances and eccentricities excite the system at shaft rotational frequencies, and the noise produced by them is usually negligible when compared to the gear mesh noise caused by the TE.

The equations derived in the previous chapter have been programmed into MATLAB. In addition, the benchmark gearbox system was also modelled in ANSYS for natural frequency result verification and for mode shape visualization. The ANSYS model is also used to verify the Frequency Response Function (FRF) obtained from MATLAB. The free response of the system is presented, and then followed by the forced response. Both responses are presented in the frequency domain. The only excitation to the system comes in the form of the TE displacement, while the mesh stiffness is assumed constant and its averaged value is

used. The constant mesh stiffness approach is justified when used in helical gear analysis, as explained in Chapter 2. Only the first harmonic of the TE excitation is considered in all the cases presented in this research. An inclusion of second order and higher order harmonics of the TE is very simple, but the inclusion increases the simulation time. Also, first harmonic is the dominant one for all the TE results obtained from the ANSYS helical gear model. The system's response due to the static or mean input is not considered because the objective of the research is the dynamic response of the system. An experimental verification of the approach (gear mesh model) presented in this thesis is given in Kahraman et al.[15].

The gearbox model given in Figure 4.1 was selected as the benchmark model for both the free and forced responses. Bearing numbers are enclosed in rectangles, while node numbers are not enclosed. Gear pair 1-2 connects nodes 3 and 10, and gear pair 3-4 couples nodes 13 and 20. Each shaft has six elements and seven nodes. The output shaft relative

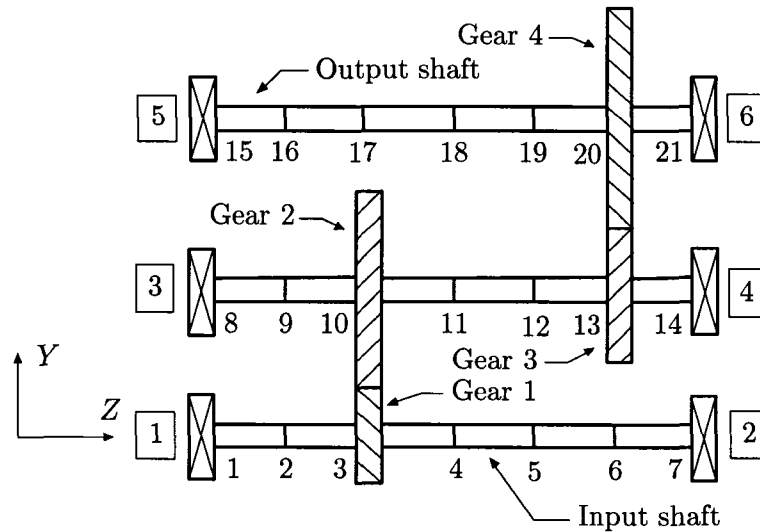


Figure 4.1: *Benchmark gearbox finite element model.* There is a total of 18 elements and 21 nodes. Bearing numbers are enclosed in rectangles, while node numbers are not enclosed. Identical gear sets are used for both gear meshes. All bearings have identical properties.

angular position (α_{34}) was chosen to allow γ_{23} to remain zero. This simplifies phase angle calculations between the two STE excitations. Angle γ_{23} will remain zero as long as α_{34} is changed in increments of 12° from its initial value of 96° . An incremental value of 12°

is a result of both gear pairs geometry and their number of teeth. The gear pair given in Table 2.2 was chosen for both gear meshes. All relevant model specifications are provided in Table 4.1.

Table 4.1: *Benchmark model specifications.* The gearbox with the properties given in this table was chosen as the benchmark model for free and forced response studies. CCW abbreviation in this table stands for counterclockwise rotational direction. Bearing stiffness values are obtained from Kahraman et al.[15].

Parameter	Notation(Units)	Typical values
input torque	$T_1(N \cdot m)$	100 CCW
mesh stiffness	$k_{12}(N/m)$	$3.79(10)^8$
mesh stiffness	$k_{34}(N/m)$	$4.09(10)^8$
relative angular position	$\alpha_{12}(degrees)$	90
relative angular position	$\alpha_{34}(degrees)$	96
helix angle	$\beta_{12}(degrees)$	15
helix angle	$\beta_{34}(degrees)$	-15
shaft element length	$l(m)$	0.03
shaft element radius	$r_b(m)$	0.0125
bearing stiffness	$k_x(N/m)$	$2(10)^9$
bearing stiffness	$k_y(N/m)$	$2(10)^9$
bearing stiffness	$k_z(N/m)$	$1(10)^9$
bearing stiffness	$k_{\theta x}(N \cdot m/rad)$	$1(10)^6$
bearing stiffness	$k_{\theta y}(N \cdot m/rad)$	$1(10)^6$
modulus of elasticity	$E(GPa)$	207
Poisson's ratio	ν	0.292

4.1 Free Response

To obtain a free response, the system was modelled in MATLAB and ANSYS. The equations developed in Chapter 3 were coded in MATLAB and eigenvalues as well as corresponding eigenvectors were obtained analytically. An ANSYS model was built using BEAM188, MASS21, COMBIN14, and MATRIX27 elements. BEAM188 is a two node linear beam element for 3D analysis. MASS21 is a structural mass point element also suitable for 3D analysis. COMBIN14 is a spring damper element with longitudinal or torsional capabilities. MATRIX 27 represents an arbitrary element with undefined geometry. Its elastic kinematic response is defined by stiffness, damping, and mass coefficients. The matrix is used to relate two nodes with each node having up to six DOF. Each element above can be assigned a number of different real constants so that it can be used in multiple places in the model, without having to define a new element every time. Table 4.2 relates the gearbox components and its corresponding ANSYS elements used in the benchmark model. Figure 4.2 shows an isometric view of the ANSYS benchmark gearbox model.

Table 4.2: *Gearbox components with equivalent ANSYS elements.* Gear masses are attached to shaft nodes. Bearing masses are neglected in the model. Gear mesh stiffnesses are modelled as symmetrical 12x12 matrices that couple two shafts holding the gears.

Gearbox component	ANSYS element
shafts and gears	MASS21
shafts	BEAM188
bearings	COMBIN14
gear mesh stiffnesses	MATRIX27

As mentioned earlier, both ANSYS and MATLAB models are used to obtain the free response for this particular system. Table 4.3 offers a comparison of the 10 lowest natural frequencies obtained from these two models and their associated modes. The first mode

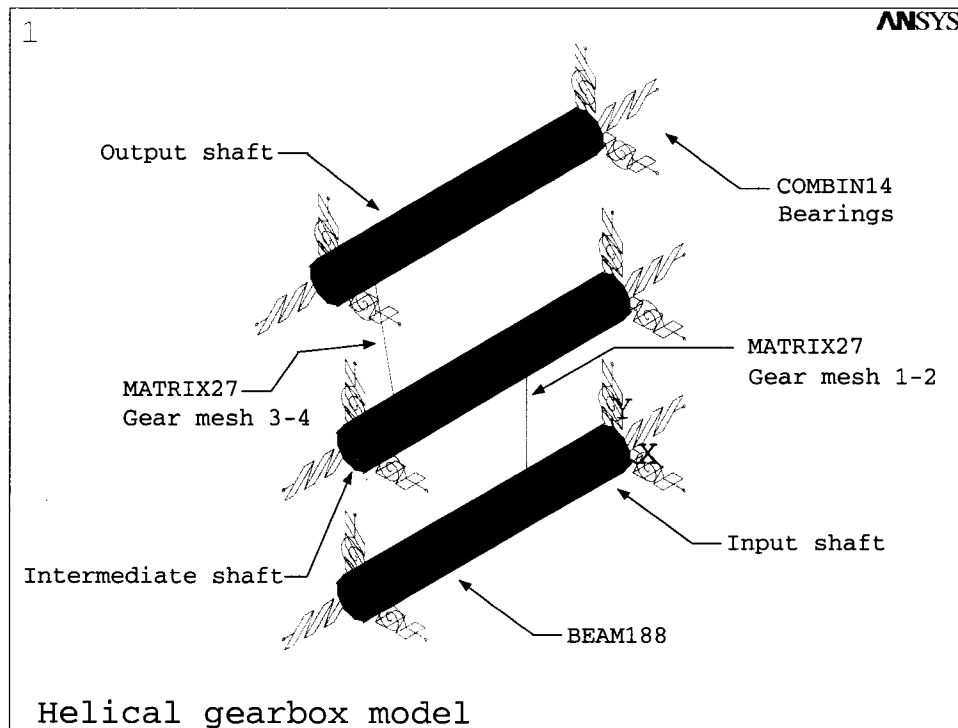


Figure 4.2: 3D ANSYS gearbox model. MASS21 structural mass point element used to model shafts and gears. Bearing mass is neglected in the model. Shafts were modelled using BEAM188 elements. There are a total of 18 shaft elements. COMBIN14 elements used to model torsional and longitudinal bearing stiffnesses. Both gear meshes used MATRIX27 elements with different real constants.

is the rotational rigid body motion of the gearbox system. The rest of the modes are exhibiting coupling between the torsional and translational DOF. Figure 4.3 shows the second

Table 4.3: *First 10 natural frequency results with their mode shapes.* In the table x , y , and z indicate displacements, while θ_x , θ_y , and θ_z are the rotations about x , y , and z directions, respectively. Shafts are annotated with the numbers in the brackets (input shaft (1), intermediate shaft (2), and output shaft (3)). For example, in the third mode, the input shaft is vibrating torsionally about the z axis, while the intermediate shaft vibration is coupled in a transverse (x and y) and torsional direction (θ_y and θ_z).

Natural frequency MATLAB (Hz)	Natural frequency ANSYS (Hz)	Percent difference (%)	Mode shape description
0	0	0	$\theta_z(1,2,3)$ -rigid body
992	993	0.10	$\theta_z(1)$, $x-\theta_z(2)$, $x-y-\theta_z(3)$
1285	1361	5.91	$\theta_z(1)$, $x-y-\theta_y-\theta_z(2)$
1376	1392	1.16	$x-y-\theta_x-\theta_y(2)$
1706	1731	1.52	$x-y-\theta_x-\theta_y(3)$
1760	1784	1.47	$\theta_z(1)$, $\theta_z(2)$, $x-y-\theta_x-\theta_y(3)$
2008	2068	2.99	$x-y-\theta_x-\theta_y-\theta_z(1)$
2269	2340	3.13	$x-y-\theta_x-\theta_y(1)$
2577	2684	4.15	$\theta_y-\theta_z-x-y(1)$, $x-y-\theta_x-\theta_y(2)$
2611	2717	4.06	$x-y-\theta_x-\theta_y(2)$

mode shape associated with the second natural frequency (993 Hz). The most dominant behaviour is the coupled intermediate shaft vibration in the $x-\theta_z$ direction, followed by the input shaft torsional vibration in θ_z direction.

A comparison of the rigid multi-body model (the model developed in this thesis) against the torsional model is worth mentioning here. In torsional models, only the flexibility of the gear teeth is taken into account. Both shafts and bearings are assumed to be rigid. To transform the current multi-body model into a torsional model, the shaft lengths need

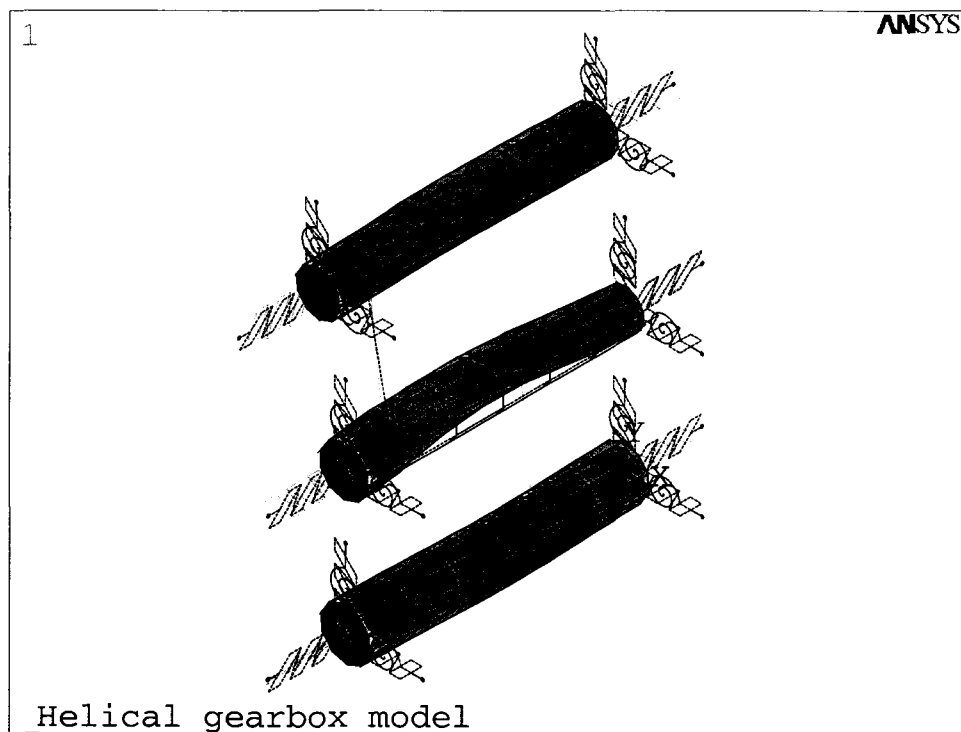


Figure 4.3: *Second mode shape in ANSYS.* The wireframe represents the undeformed, while the solid represents the deformed model shape. The intermediate shaft exhibits coupled vibration in x - θ_z direction. The next significant vibration is the torsional vibration (θ_z) of the input shaft. The output shaft motion is also coupled, but with relatively lower amplitudes when compared to the other two shafts.

to be decreased, thus increasing their stiffness, and bearing stiffnesses values also have to be increased. Figure 4.4 shows the first four natural frequencies of the multi-body model used as a torsional model. The results in the figure were obtained with element length equal to 0.03 mm , while the bearing stiffness coefficient was varied. The element length of 0.03 mm was chosen to sufficiently stiffen the shafts, and has no real physical significance. The two natural frequencies of the torsional model are 3864 (second) and 7790 (third) Hz . In Table 4.3 (multi-body model), the second natural frequency is equal to 992 Hz , and the third one is equal to 1285 Hz . A torsional model failed to predict a very large number of significant natural frequencies by neglecting shaft and bearing flexibilities. When using torsional models for gear dynamics studies of real gearbox systems with flexible bearings and shafts, one has to be fully aware of their shortcomings.

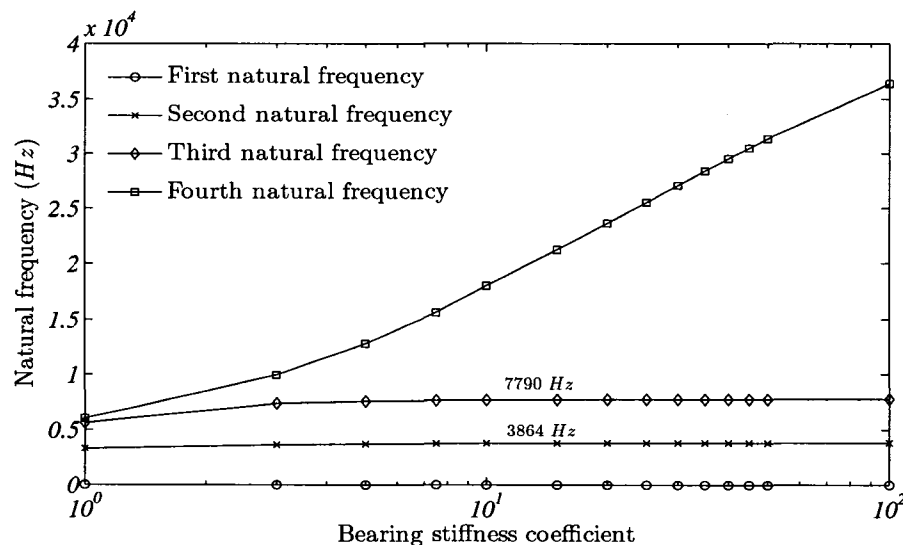


Figure 4.4: First four natural frequencies of the torsional model. The element length was chosen to be equal to 0.03 mm . As the bearing stiffness coefficient increases, the multi-body model transforms into a purely torsional model. Gear teeth are the only source of flexibility in the system. First natural frequency represents the rigid body mode. Second and third natural frequencies converge towards the torsional model natural frequencies (3864 Hz and 7790 Hz). Fourth and higher natural frequencies head towards infinity.

4.2 Forced Response

To investigate the system's forced response to a more complicated input, the frequency response function to a unity sinusoidal input is investigated first. For this purpose, both ANSYS and MATLAB models are used. The two FRF plots obtained from both models are plotted in Figure 4.5. Both of them represent gear 1 torsional response to a θ_z unity sinusoidal excitation at the gear 1 node (node 3). Resonance peaks obtained from the two models agree well with each other. The small discrepancy between the two results comes from the fact that MATLAB uses mode summation technique to obtain displacements, while ANSYS uses the direct solution technique to solve for displacements.

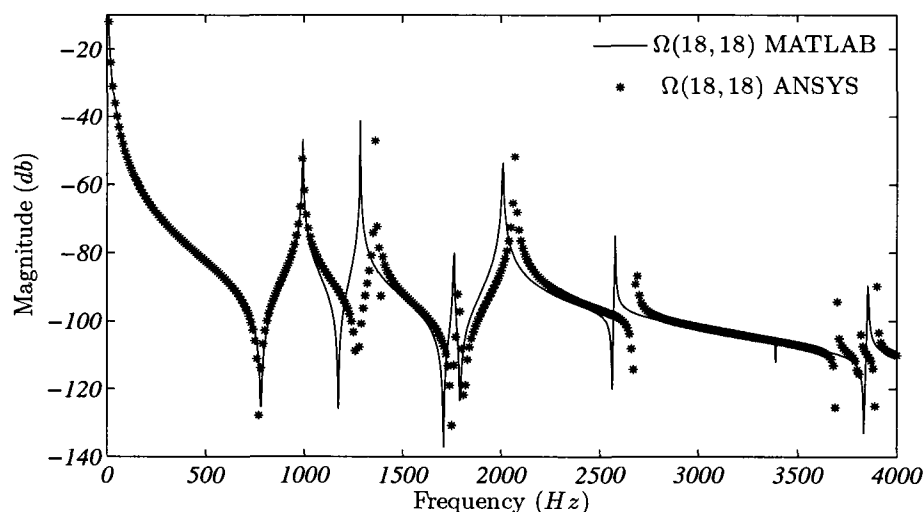


Figure 4.5: *MATLAB and ANSYS frequency response for gear 1 node.* Both approaches provide well correlated results. ANSYS response up to 1200 Hz is perfectly correlated with the MATLAB response.

Now that the FRF for the system was briefly presented and validated by the use of ANSYS and MATLAB models, the gearbox response due to the excitation at both gear meshes is analyzed. From this point on, only the MATLAB model is used. Instead of having a single excitation in the system, now the same excitation frequency can occur at two different input shaft speeds. In addition, these two excitations may or may not be in phase depending on the shaft positions and number of gear teeth on each gear. In Figure 4.6

the FRF response of the system as a function of the input shaft speed is shown. The first critical shaft speed is around 4000 *rpm*. Here, the system is being excited through gear pair 1-2 with the frequency of the excitation being equal to 2008 *Hz* (mode 7). At the same input shaft speed, because of the gear reduction, the gear pair 3-4 is exciting the system at 992 *Hz* (mode 2).

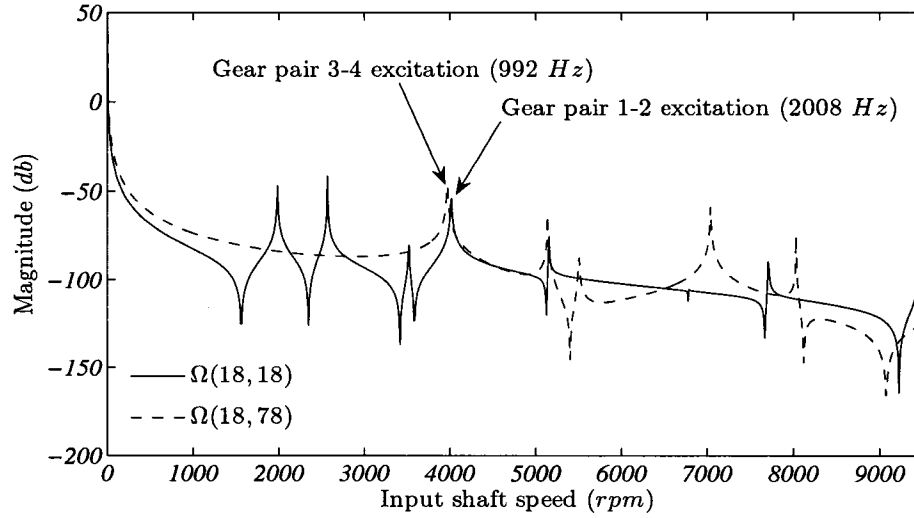


Figure 4.6: Frequency response at gear 1 node due to multi-mesh excitation. At the input shaft speed around 4000 *rpm*, the two peaks resulting from two different excitation frequencies are too close to each other. A similar phenomenon is observed at around 5000 *rpm*, but with a relatively smaller amplitude.

4.2.1 Benchmark Model Response

Dynamic transmission error for both gear pairs and dynamic forces on bearing 6 are chosen as the parameters by which the system's response to internal excitations will be quantified. For all the forced response studies, a modal damping of 3.5 % is used. The following STE excitation values are used for all simulations presented: $e_{12} = 1.14 \mu m$ and $e_{34} = 1.89 \mu m$. These values are valid as long as the input torque remains at 100 *N·m* and gears from Table 2.2 are used. If using different torque values, appropriate mesh stiffness and TE values have to be used. Figure 4.7 shows DTE results for both gear meshes for the benchmark gearbox model. Both dynamic forces on bearing 6 are plotted in Figure 4.8.

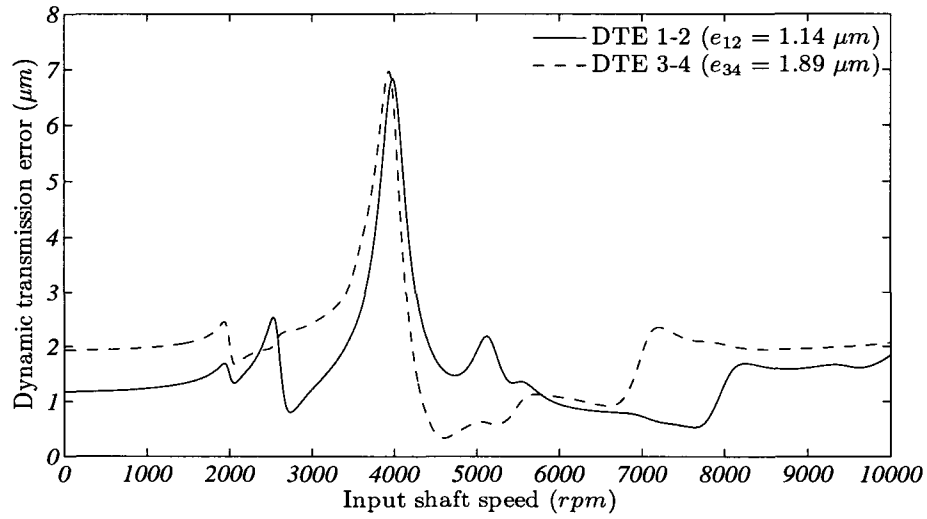


Figure 4.7: *Dynamic transmission errors for the benchmark model.* An input torque value of 100 Nm CCW and ζ_s equal to 0.035 were used in the simulation. Both DTEs experience the largest amplitudes around the 4000 rpm . At this speed, both gear meshes excitations are influencing both DTEs, resulting in very large amplitudes. The input shaft speed in the region around 6800 rpm presents the optimum operational point for the benchmark gearbox model.

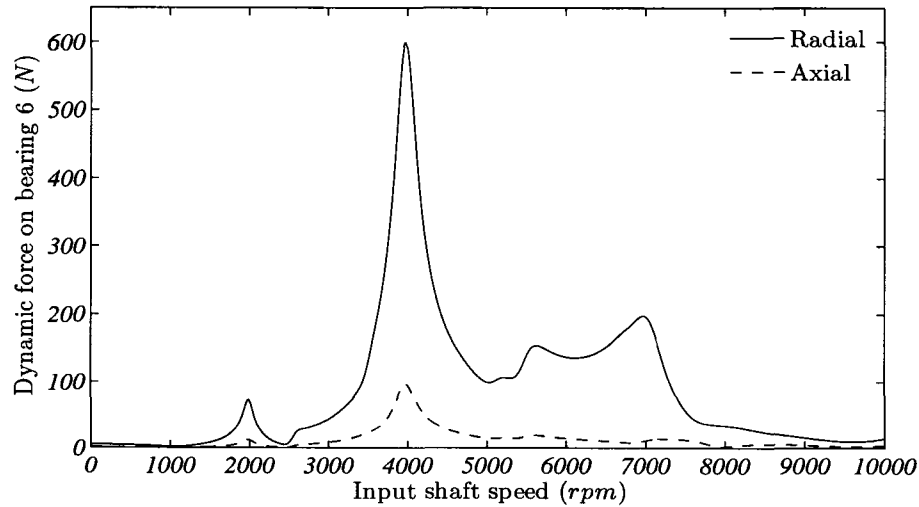


Figure 4.8: *Dynamic forces on bearing 6 for the benchmark model.* An input torque value of 100 Nm CCW and ζ_s equal to 0.035 were used in the simulation. Both forces are maximized around 4000 rpm .

4.2.2 Output Shaft Angle Effects

Next, the effect of the output shaft position angle on each DTE is investigated. α_{34} (Figure 4.9) is increased from the position of 0° in increments of 24° . The DTE for gear mesh

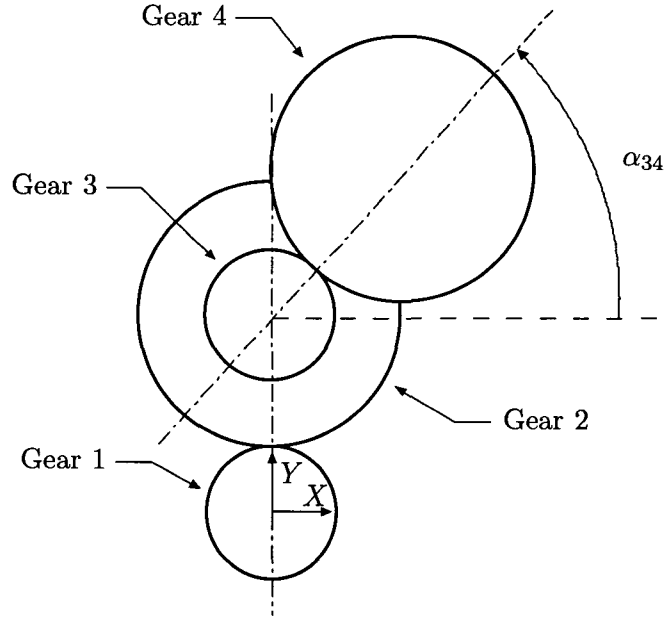


Figure 4.9: *Output shaft position angle α_{34} definition.* Front view of the gearbox model with the definition of the output shaft position angle. Angle α_{34} should be incremented in 24° increments from its initial position of 96° . If this is respected, then the phase angle between the two TE excitations will not be affected.

1-2 is plotted in Figure 4.10, while the DTE for gear mesh 3-4 is plotted in Figure 4.11. A large DTE amplitude around 4000 rpm is still present in all cases of output shaft position angles. The DTE at 4000 rpm for gear pair 1-2 (Figure 4.10) decreases as the value of α_{34} is increased. The benchmark model results in the lowest DTE 1-2 amplitude ($6.8 \mu\text{m}$) out of five cases considered. The same trend is present around 5200 rpm , where a change in output shaft angle from 0° to 96° reduces the DTE 1-2 from $4.5 \mu\text{m}$ to $2.2 \mu\text{m}$ (not indicated in the figure). The amplitude of DTE 3-4 is not a function of α_{34} as shown in Figure 4.11. For both DTEs, the two resonant peaks caused by both mesh excitations at 4000 rpm are still too close to each other and are causing excessive torsional vibrations in the system. Changes in α_{34} alone do not cause significant shifts in natural frequencies which

would move the two resonant peaks apart and improve dynamic response of the gearbox model.

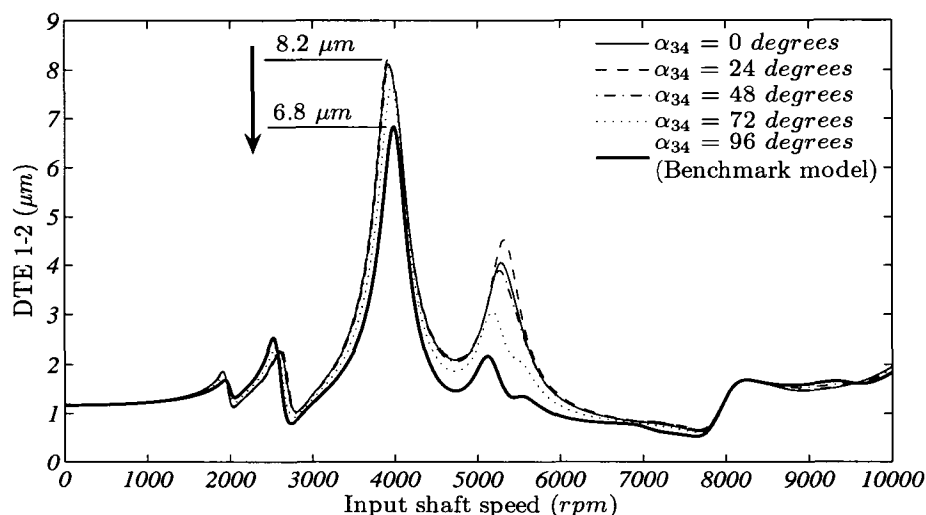


Figure 4.10: Gear pair 1-2 dynamic transmission error for varied output shaft angle. Dynamic transmission error decreases slightly with the output position angle increase at 4000 rpm. Around this speed, the benchmark model results in the lowest DTE 1-2 amplitude (6.8 μm) out of five cases considered. Shaft position angle is more influential at around 5200 rpm also with the same downward trend. Here, a change in output shaft angle from 0° to 96° reduces the DTE 1-2 from 4.5 μm to 2.2 μm (not indicated in the figure).

The effect of the output shaft angle on dynamic forces on bearing 6 is investigated next. Figure 4.12 shows radial dynamic bearing force on bearing 6 for the same five values of α_{34} used for DTE simulation. Radial bearing force is almost independent of α_{34} at all shaft speeds. A very large amplitude is observed around 4000 rpm. x and y bearing forces are changing significantly with the change in α_{34} , but the overall sum (radial) force exhibits very loose dependence on α_{34} . Axial dynamic bearing force on bearing 6 is shown in Figure 4.13 for the same values of α_{34} . In this case, the peak at around 8500 rpm is significantly reduced with the increase in α_{34} . In addition, the bearing force amplitude is larger at 8500 rpm when compared to the resonance peak at 4000 rpm for 0° and 24° values of α_{34} . Also, the axial force amplitude is much smaller when compared to the radial force amplitude for the same bearing, as it should be, due to the moderate helix angle of gear 4.

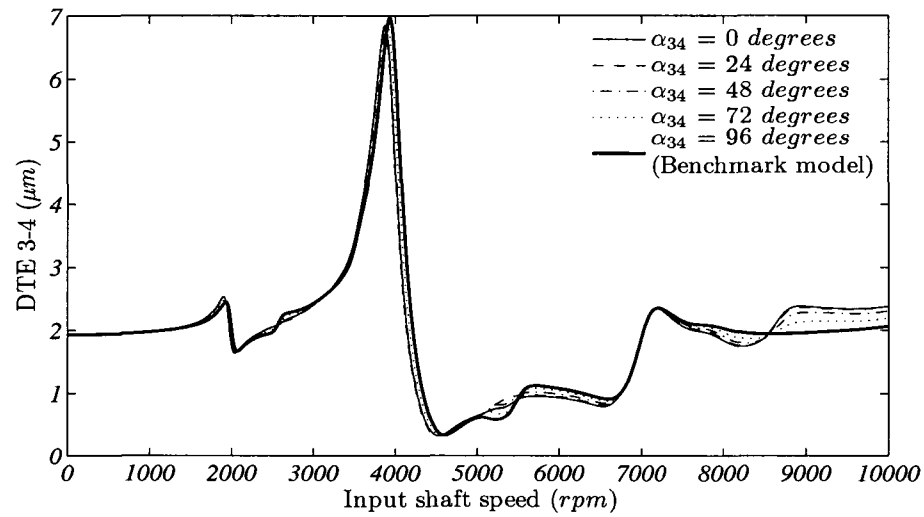


Figure 4.11: Gear pair 3-4 dynamic transmission error for varied output shaft angle. α_{34} has negligible influence on the DTE amplitude at all shaft speeds.

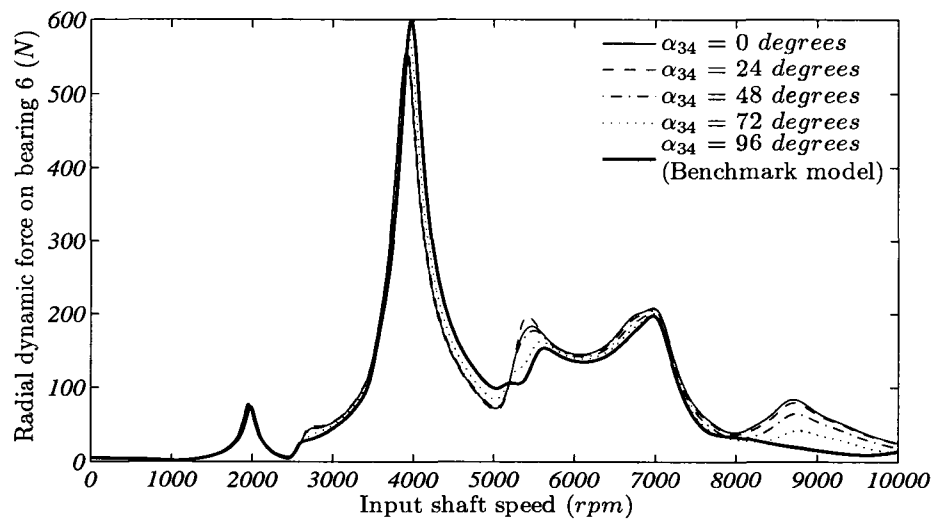


Figure 4.12: Radial dynamic force on bearing 6 for varied output shaft angle. Radial force on the bearing is lightly dependent of the output shaft position angle. x and y bearing forces are changing significantly with α_{34} but their sum (radial) force is independent of α_{34} .

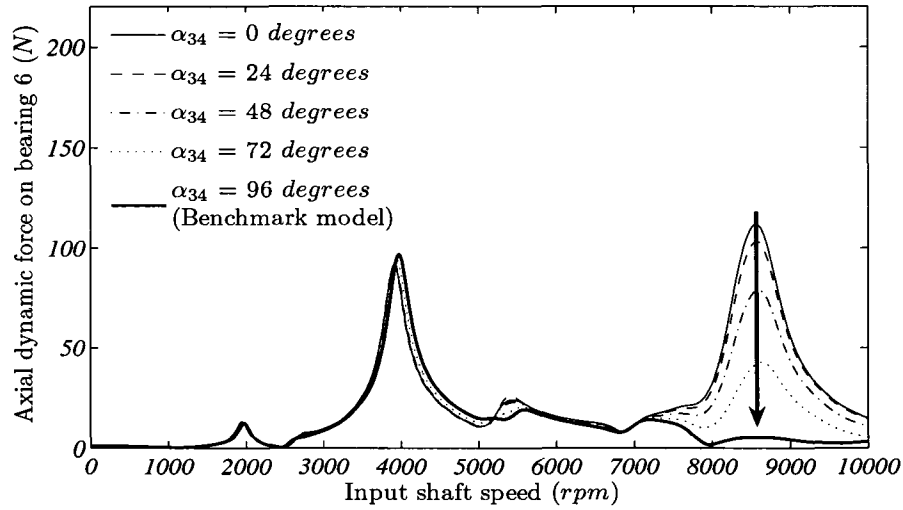


Figure 4.13: Axial dynamic force on bearing 6 for varied output shaft angle. Axial force on the bearing is slightly dependent on the output shaft position angle up to the input shaft speed of 7000 *rpm*. Starting at this speed, the bearing force decreases significantly with the increase in α_{34} (downward arrow). In addition, the bearing force amplitude is larger at 8500 *rpm* when compared to the resonance peak at 4000 *rpm* for 0° and 24° values of α_{34} .

4.2.3 Shaft Length Effects

In the previous section, the influence of α_{34} on the system's dynamics was investigated. The DTE peaks at 4000 *rpm* input shaft speed for all values of α_{34} . In other words, the output shaft angle change is not sufficient to cause significant shifts in system's natural frequencies and as a result, excessive values of DTE around 4000 *rpm* for both gear meshes are observed. The radial bearing force is maximized at this shaft speed, while the axial force peaks at 4000 *rpm* and 8500 *rpm*, depending on the output shaft angle value.

To shift system's natural frequencies, and to observe the effect of the frequency shift on both DTEs and bearing 6 forces, shaft element length is varied next. All the benchmark gearbox properties remain the same, except that the shaft element length is varied. There are still six elements making up each shaft, so by varying the element length, each shaft length varies accordingly. In all the cases presented, the decrease in shaft length causes an increase in shaft stiffness, which raises the natural frequencies. Figure 4.14 shows the DTE for gear pair 1-2 and Figure 4.15 represents plots for the gear pair 3-4, both for varied

element length. The element length resulting in the lowest DTE for gear pair 1-2 is equal to 0.02 m ($2.9\text{ }\mu\text{m}$), while for gear pair 3-4, the optimum element length is equal to 0.03 m ($7\text{ }\mu\text{m}$). Worth noting is the overall change in shape of DTE 1-2 between the benchmark model and all other cases. The benchmark model plot shows one significant peak, while other plots show multiple peaks but with lower amplitudes. Both figures reveal shifts in first significant resonance peaks with the element length increase.

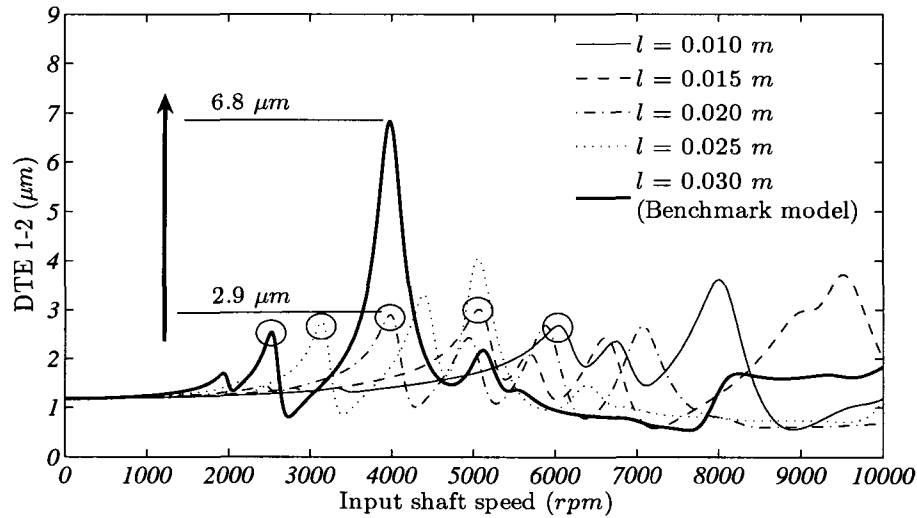


Figure 4.14: Gear pair 1-2 dynamic transmission error for varied element length. The largest amplitude of the DTE occurs at the element length of 0.03 m (Benchmark model) and is equal to $6.8\text{ }\mu\text{m}$. The lowest amplitude occurs at the element length of 0.02 m and is equal to $2.9\text{ }\mu\text{m}$. Also, the increase in the element length lowers the input shaft speed where first significant resonances occur (first significant resonance peaks for each element length are marked with circles).

The effect of the element length on dynamic forces on bearing 6 is investigated next. The dynamic radial force on bearing 6 is shown in Figure 4.16. A reduction in shaft lengths increases bearing dynamic forces. By increasing the elements length from 0.01 m to 0.03 m , a decrease in dynamic force from 1750 N to 600 N is attained. As shaft lengths are decreased, their stiffness increases, and as a result, bearing stiffness governs the system stiffness resulting in an increase in bearing force. Axial force plots are shown in Figure 4.17. Axial force exhibits very similar dependency on element length as the radial force, but with

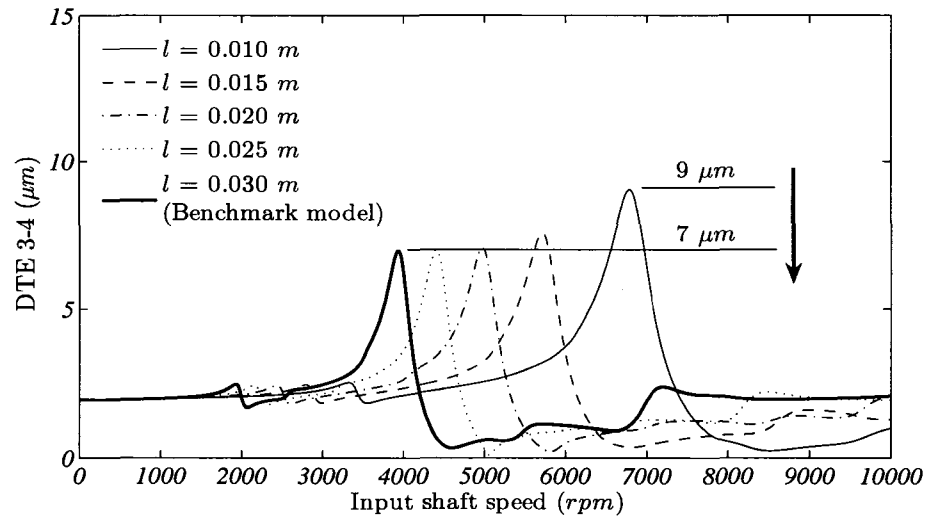


Figure 4.15: Gear pair 3-4 dynamic transmission error for varied element length. The largest amplitude of DTE occurs at the shaft element length of 0.01 m and is equal to 9 μm . The lowest amplitude occurs at the element length of 0.03 m and is equal to 7 μm .

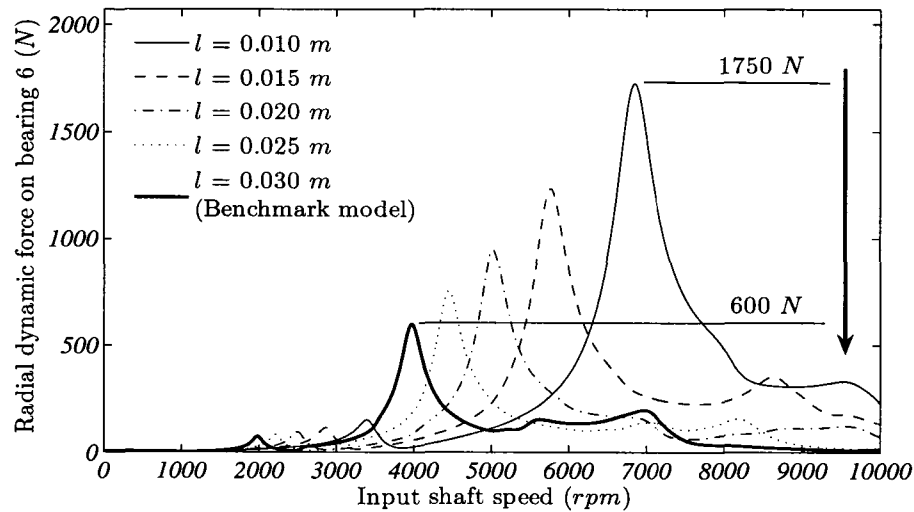


Figure 4.16: Radial dynamic force on bearing 6 for varied element length. As shaft length decreases, stiffness increases, and as a result, bearing node vibration becomes more dominant. The reduction from 1750 N to 600 N in dynamic force, as the element length is increased, is obvious in the figure. In addition, first significant resonance peaks are shifted to the right with a decrease in shaft length.

significantly smaller amplitudes. Here, a 200 N force reduction is obtained by increasing the element length from 0.01 m to 0.03 m .

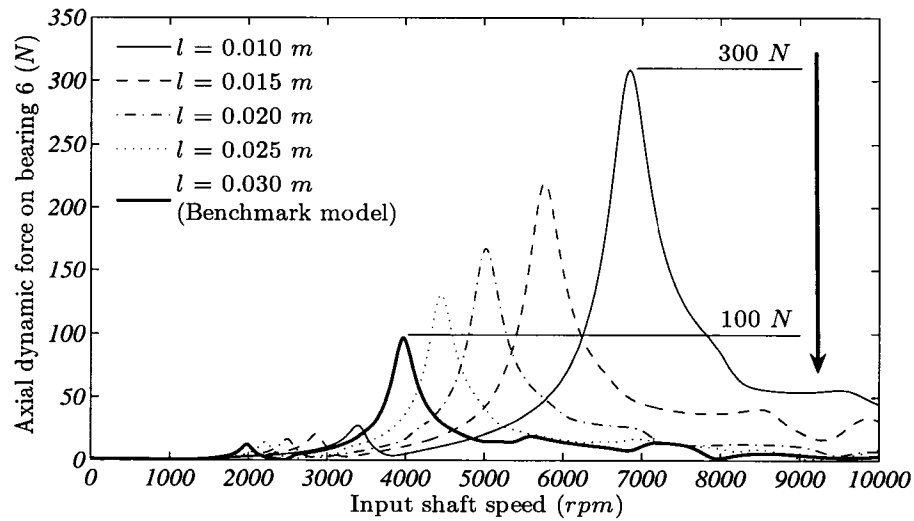


Figure 4.17: Axial dynamic force on bearing 6 for varied element length. An increase in the element length results in lower axial bearing forces. The reduction from 300 N to 100 N in bearing dynamic force, as the element length increases, is obvious in the figure.

4.2.4 Bearing Stiffness Effects

In contrast with the output shaft angle, shaft length has a significant influence on gearbox dynamic response. This is especially true for DTE 1-2, where a significant reduction is obtained just by reducing the length of each shaft from 0.18 m to 0.12 m . DTE 3-4 increases slightly for the same element length (0.02 m). As expected, a decrease in the element length causes a significant increase in bearing forces.

Next, the bearing stiffness influence on the systems dynamics is investigated. Each benchmark gearbox bearing stiffness matrix is multiplied by the stiffness coefficient (ς). Figure 4.18 shows DTE 1-2 for five bearing stiffness coefficient values. Initially, DTE amplitude increases with the increase in bearing stiffness. DTE 1-2 peaks at ς equal to one. With further increase in the bearing stiffness coefficient, a decrease in DTE 1-2 peak amplitude is shown. Once ς reaches a value of 10, the DTE does not change significantly with any further increase in ς . When ς reaches a value of 10 and higher, the peak amplitude of DTE 1-2 becomes equal to 4.8 μm . Figure 4.19 shows DTE 3-4 for varied bearing stiffness coefficient values. When compared to the previous figure (Figure 4.1), where with the initial increase in bearing stiffness there was an increase in DTE 1-2 amplitude, here, there is an immediate decrease in DTE 3-4 magnitude with the increase in bearing stiffness. The reason for this behaviour lies in the fact that the gear pair 3-4 is positioned closer to the bearings than the gear pair 1-2. As a consequence, bearing stiffness has a larger influence on gear pair 3-4 dynamic behaviour, while gear pair 1-2 behaviour is more influenced by shaft flexibilities.

Bearing stiffness coefficient effects on bearing 6 dynamic forces are presented next. Figure 4.20 shows the radial dynamic force on bearing 6. A very significant increase in bearing force (90 N to 630 N) is present for both extreme cases considered here. Also, the shaft speed where the two peaks occur shifts to the right with an increase in bearing stiffness. The benchmark model force peak amplitude is very close to the maximum amplitude ($\varsigma = 100$). Axial bearing force is plotted in Figure 4.21. In contrast with the previous figure, here the peak bearing force occurs at the $\varsigma = 0.1$, not at the maximum value of ς .

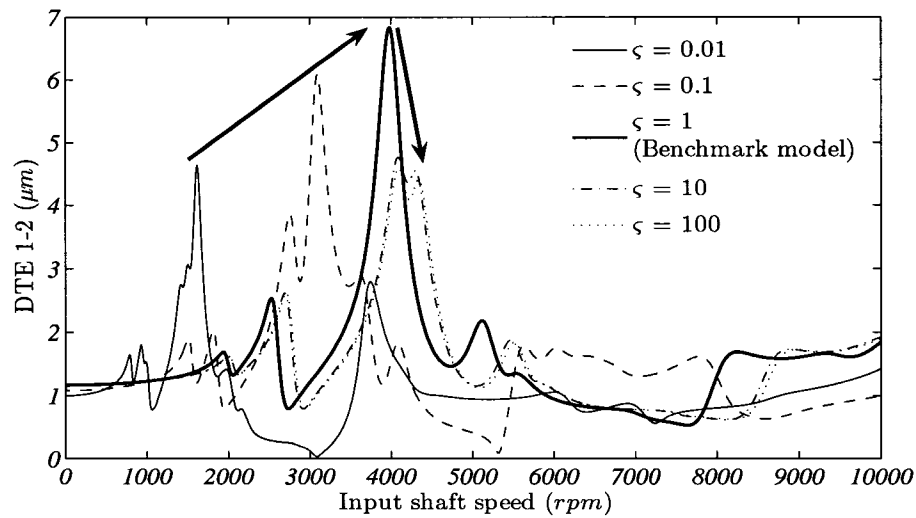


Figure 4.18: Gear pair 1-2 dynamic transmission error for varied bearing stiffness coefficient. A steady increase in DTE 1-2 comes as a result of an increase in the bearing stiffness coefficient (up-right arrow) up to a certain point. The benchmark model DTE 1-2 has the highest amplitude out of five cases considered. When the bearing stiffness coefficient increases beyond the benchmark model value, a decrease in the DTE amplitude is obvious (down arrow). DTE plots for ζ values of 10 and higher show very little changes because the system's stiffness becomes governed by shaft element stiffness.

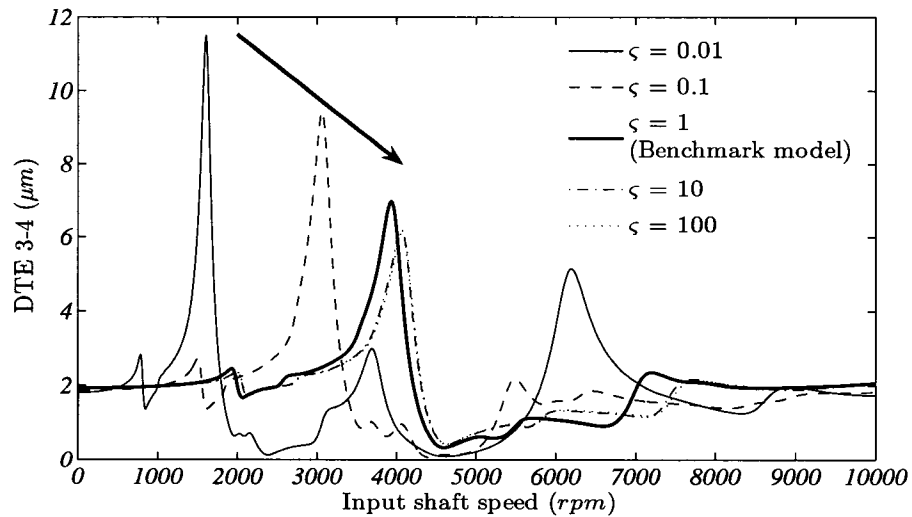


Figure 4.19: Gear pair 3-4 dynamic transmission error for varied bearing stiffness coefficient. First significant resonance peaks shift to the right with an increase in bearing stiffness. Also, with the shift, a decrease in DTE 3-4 peak amplitude is present (down-right arrow). All curves exhibit the same overall shape with one dominant resonant peak.

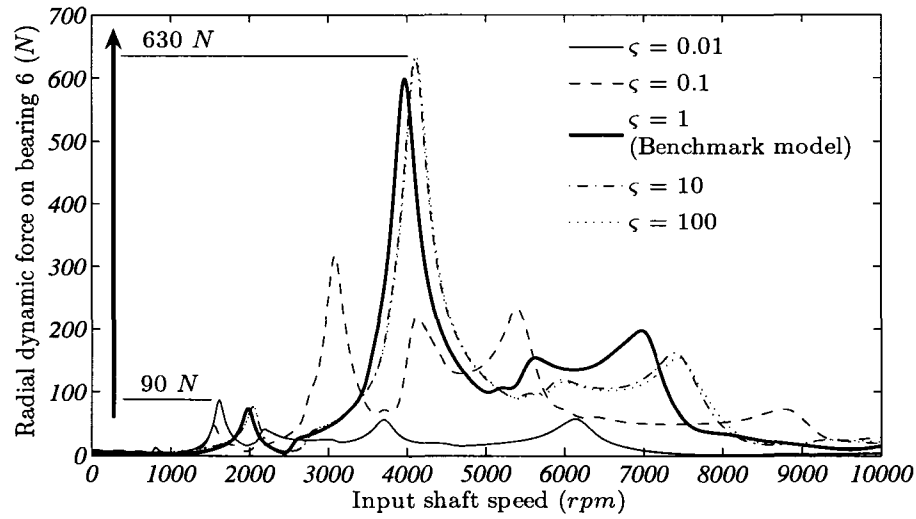


Figure 4.20: Radial dynamic force on bearing 6 for varied bearing stiffness coefficient. As expected, an increase in bearing stiffness causes an increase in bearing force. An increase in bearing force from 90 N to 630 N is present when the stiffness coefficient changes from its minimum value of 0.01 to its maximum value equal to a 100. Once the ζ reaches a value of 10, any additional increase in ζ has little influence on radial bearing force.

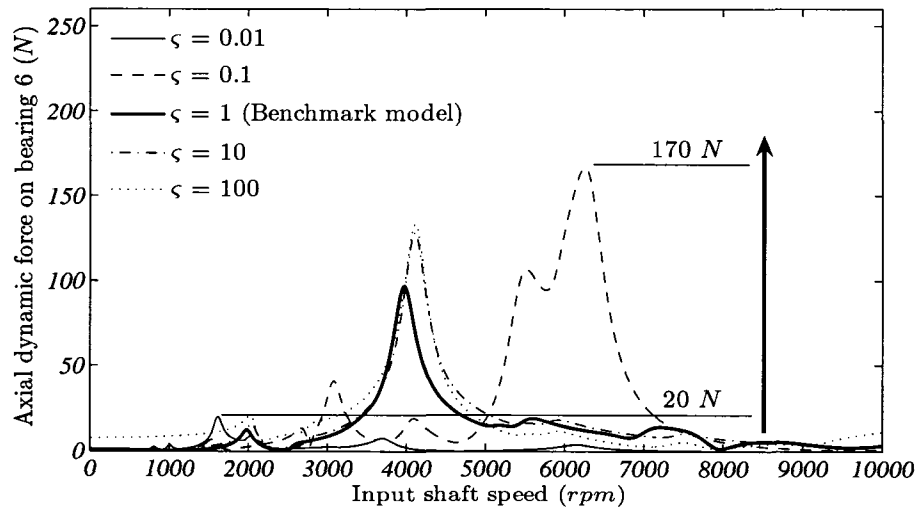


Figure 4.21: Axial dynamic force on bearing 6 for varied bearing stiffness coefficient. The peak amplitude of the bearing force increases with an increase in the bearing stiffness coefficient. The maximum bearing force (170 N) does not occur at the highest value of ζ , but it occurs at $\zeta = 0.1$. A very small value of bearing force (20 N) is possible if bearing stiffness remains low. However, low bearing stiffness causes too high of a value for DTE 3-4 (Figure 4.19).

4.2.5 Gear Pair Relative Position Effects

For this study, the position of both gear pairs is varied. Figure 4.23 presents the DTE 1-2 results for varying gear pair position. The legend entry (3-10,13-20) in this figure, and the rest of the figures in this subsection indicate that the gear pair 1-2 connects the shafts at nodes 3 and 10 and gear pair 3-4 connects the shafts at nodes 13 and 20 according to Figure 4.22. A decrease in DTE 1-2 peak amplitude is present when the position of the gear

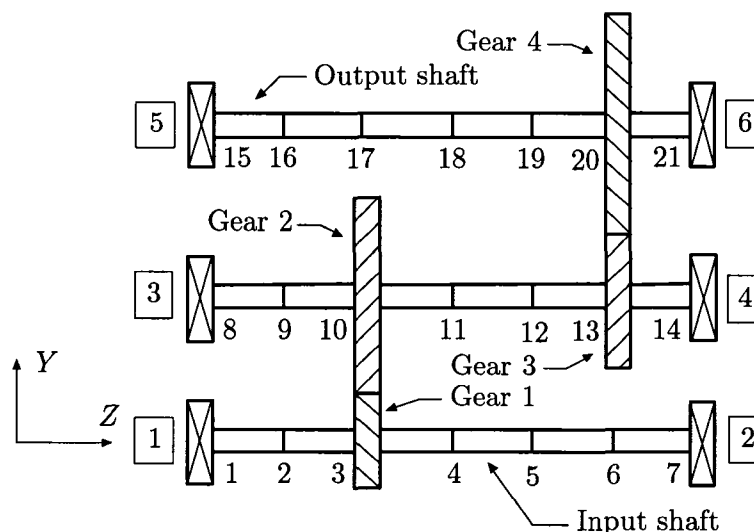


Figure 4.22: *Gearbox model layout.* Bearing numbers are enclosed in rectangles, while node numbers are not enclosed. In subsection 4.2.5 the axial position of both gear pairs was varied. This figure is used to assist in visualization of different axial positions for both gear pairs. For this study, a total of five different cases were considered. Initially, the position of gear pair 1-2 was kept constant (coupled nodes 3 and 10), while the gear pair 3-4 was moved to the left (coupled nodes 13 and 20, then nodes 12 and 19, and lastly, nodes 11 and 18). For the last two cases, both gear pairs were first offset to the left (gear pair 1-2 connected nodes 2 and 9, while gear pair 3-4 connected nodes 10 and 17), and then to the right (gear pair 1-2 coupled nodes 5 and 12, while gear pair 3-4 coupled nodes 13 and 20).

pair 1-2 is kept constant, while the gear pair 3-4 moves towards the centre of the shafts (first three cases in the figure). As both gear pairs are offset to either side (last two cases in the figure), peak DTE 1-2 amplitude increases. DTE 3-4 results are presented in Figure 4.24. DTE 3-4 peak amplitudes are larger than DTE 1-2 amplitudes in Figure 4.23 for all the cases considered. The best relative gear pair 3-4 position for the five cases considered is

the orientation where gear pair 3-4 connects nodes 13 and 20 and gear pair 1-2 connects nodes 3 and 10 (benchmark model). DTE 3-4 increases as a result of gear pair 3-4 moving away from bearing 6 (first four cases in the figure) because of the fact that the gear 4 node stiffness decreases as it moves away from bearing 6. In both figures (Figure 4.23 and Figure 4.24), the fourth case position results in the maximum amplitude for both DTEs. In this position both gear pairs are offset to the left (Figure 4.22), and the gear pair 3-4 excites the system with greater amplitude ($e_{34} > e_{12}$) than the gear pair 1-2. A combination of these two factors results in greater system vibrations when compared to all other cases.

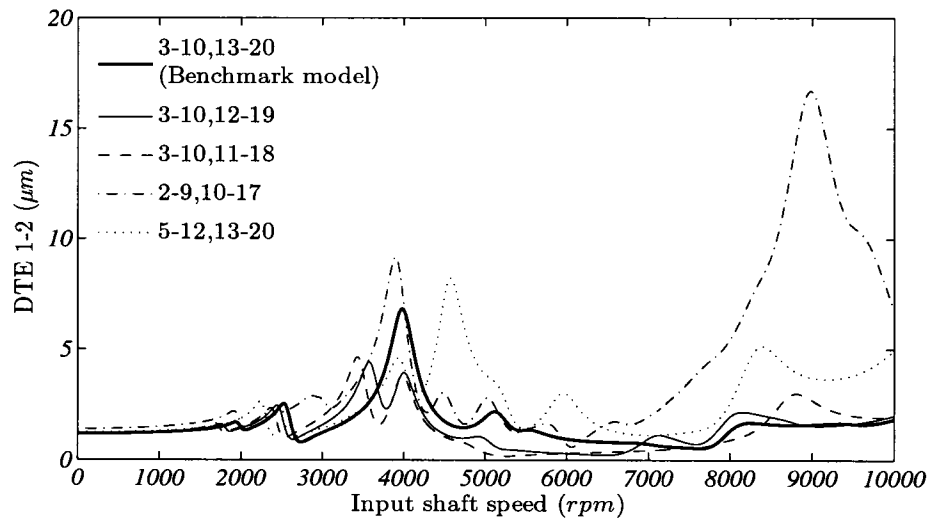


Figure 4.23: Gear pair 1-2 dynamic transmission error for varied gear pair position. The legend entry (3-10,13-20) indicates that the gear pair 1-2 connects the shafts at nodes 3 and 10 and gear pair 3-4 connects the shafts at nodes 13 and 20 according to Figure 4.22. In the first three cases, the gear pair 3-4 moves closer to the center of the shafts, while the gear pair 1-2 position remains fixed. This positioning direction has a positive effect on DTE 1-2 peak amplitude. The reason for the DTE decrease lies in the fact that as the gear pairs move towards shaft centres, they increase the overall stiffness of the system (gear meshes act as two very stiff springs supporting shafts at their centres) as long as the two transmission error excitations are not in phase. When both gear pairs are offset to the left or to the right (last two cases), DTE 1-2 peak amplitude increases. In this case, shafts are not supported in their centres, and the overall vibration increases.

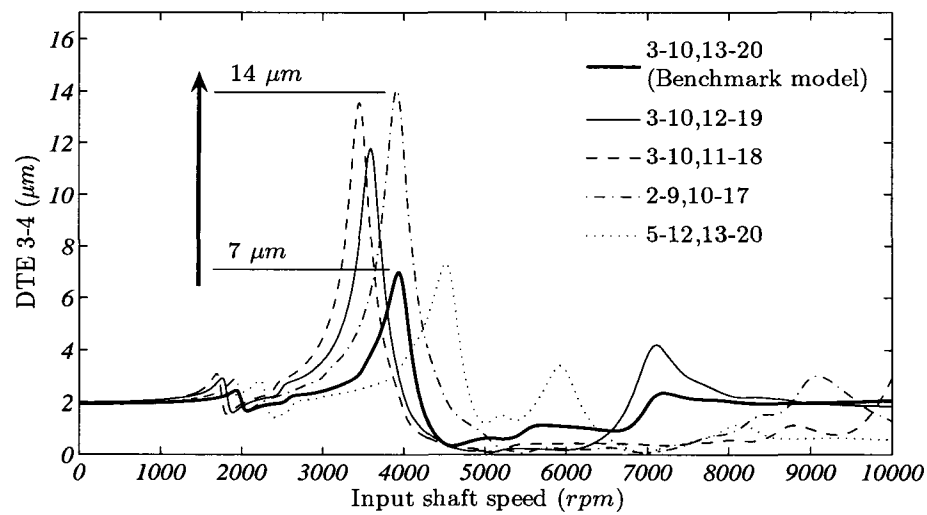


Figure 4.24: Gear pair 3-4 dynamic transmission error for varied gear pair position. The legend entry (3-10,13-20) indicates that the gear pair 1-2 connects the shafts at nodes 3 and 10 and gear pair 3-4 connects the shafts at nodes 13 and 20 according to Figure 4.22. The benchmark model orientation results in the minimal DTE 3-4 peak amplitude for the five cases considered. DTE 3-4 peak amplitude increases from $7\ \mu\text{m}$ to $14\ \mu\text{m}$ between the benchmark model orientation and the fourth case (2-9,10-17) orientation.

Bearing force results are presented next. Figure 4.25 includes plots of radial bearing force. Radial bearing force is minimized when both gear pairs are offset to the left (2-9,10-17). On the other hand, the bearing 6 force is maximized when both gear pairs are closest to the bearing 6 location (5-12,13-20), in which case, most of the energy is dissipated through bearings rather than shafts. This plot exhibits multiple resonance peaks instead of one dominant resonant peak present in other plots. Axial force plots are shown in Figure 4.26. Trends similar to those in Figure 4.25 are present here. The first dominant resonant peak is at 4000 *rpm* with the second significant peak around 8500 *rpm*. Amplitudes at the second resonance are higher than those at the first resonance, while the opposite is true for Figure 4.25.

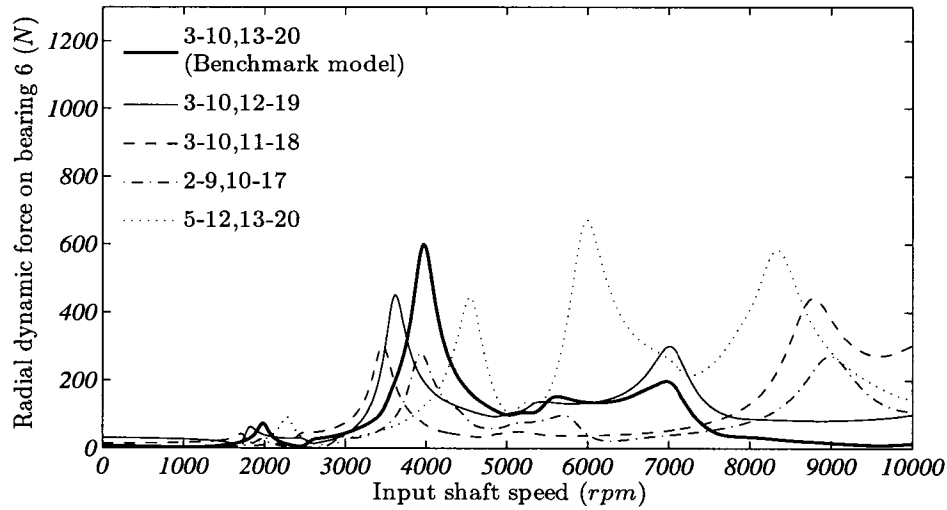


Figure 4.25: *Radial dynamic force on bearing 6 for varied gear pair position.* The legend entry (3-10,13-20) indicates that gear pair 1-2 connects the shafts at nodes 3 and 10 and gear pair 3-4 connects the shafts at nodes 13 and 20 according to Figure 4.22. As expected, the least favoured orientation with respect to the radial bearing 6 force is the last orientation shown in the figure (5-12,13-20). Here, both gear pairs are offset to the right, closest to the bearing 6 location. Plots for other cases show one dominant resonance peak, while in the last case, there are multiple significant resonance peaks.

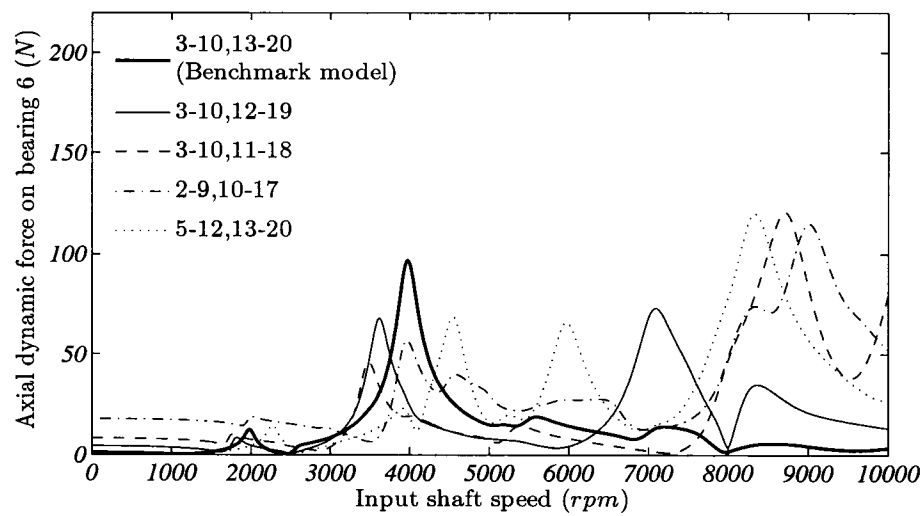


Figure 4.26: Axial dynamic force on bearing 6 for varied gear pair position. The legend entry (3-10,13-20) indicates that the gear pair 1-2 connects the shafts at nodes 3 and 10 and gear pair 3-4 connects the shafts at nodes 13 and 20 according to Figure 4.1. The relationship between different plots here is similar to the relationship shown in Figure 4.25, but with smaller amplitudes.

4.3 Discussion

Results presented in this chapter are summarized and briefly discussed:

- The output shaft angle does not significantly alter natural frequencies of the system, and as a result, there is little change in both DTEs and bearing 6 forces. The output shaft position angle has a small effect on DTE 1-2 amplitude near the two resonant peaks (Figure 4.10). DTE 3-4 is independent of the output shaft angle at all input shaft speeds (Figure 4.11). The radial dynamic force on bearing 6 is also independent of the output shaft angle (Figure 4.12), while the axial force shows very high dependency on the output shaft angle (Figure 4.13) at the input shaft speed around 8500 *rpm*.

- Shaft length has a significant effect on a system's dynamic response. With the decrease in element length, the system's stiffness increases, which results in an increase in natural frequencies. Both DTE peak amplitudes are affected by shaft element length (Figure 4.14 and Figure 4.15). Both radial and axial bearing forces increase significantly when element length decreases from 0.03 *m* to 0.01 *m* (Figure 4.16 and Figure 4.17).

- A bearing stiffness coefficient was introduced to perform bearing stiffness effect studies. All bearing stiffness matrices were multiplied by this factor to alter their properties. Both DTE peak amplitudes lessen (Figure 4.18 and Figure 4.19) as a result of the bearing stiffness factor increase. This trend continues until a certain point ($\varsigma = 10$) after which the bearing stiffness has no more influence on the system. From this point on, the system's stiffness is governed by shaft and gear teeth flexibilities. Radial and dynamic bearing 6 forces also increase with the increase in bearing stiffness (Figure 4.20 and Figure 4.21).

- The effect of gear pair relative position on both DTEs and bearing 6 forces was investigated next. The orientation that maximizes both DTEs uses gear pair 1-2 to connect nodes 2 and 9, and gear pair 3-4 to connect nodes 10 and 17 (Figure 4.23 and Figure 4.24). This position allows gear pair 3-4 excitation of the system that is closer to shaft centres resulting in larger vibrations. Both forces (radial and axial) on bearing 6 are maximized in

5-12,13-20 (Figure 4.25 and Figure 4.26) position, at which both gear pairs are positioned closest to bearing 6.

Chapter 5

Conclusions and Future Work

5.1 Summary

An analytical finite element model of a double-stage helical gear reduction has been developed and coded in MATLAB. The model includes linear time invariant helical gear mesh stiffness, flexible shafts and bearings, and a rigid housing. Each element is modelled using mass and stiffness matrices. In addition, an ANSYS partial tooth helical gear pair model has also been developed. The STE and mesh stiffness were the primary results obtained from the ANSYS model. Both of these parameters were then employed in the finite element model. The STE served as the internal excitation to the system, while the mesh stiffness value was assigned to a spring that coupled the two engaged gears. Eigen analysis was used to obtain the free response, while the modal summation technique was employed for the forced system's response. Modal damping was used instead of damping matrices. To verify the MATLAB natural frequency results, and to assist in the visualization of system's mode shapes, an equivalent finite element gearbox ANSYS model has also been constructed. An ANSYS model includes BEAM188, MASS21, COMBIN14, and MATRIX27 elements. Also, the multi-body model developed here was transformed into an equivalent torsional model to point out the shortcomings of the torsional model. The MATLAB model was then utilized to perform a limited number of parametric studies. For this purpose, a benchmark gearbox model similar to a gearbox designed for a HEV has been selected.

5.2 Conclusions

Natural frequency results from both models (ANSYS and MATLAB) show a very high degree of correlation. The shortcomings of the purely torsional model when compared to the torsional-translational were pointed out justifying the use of the latter model. The influence of the output shaft position angle, shaft length, bearing stiffness, and the position of both gear pairs on both DTEs and bearing 6 forces was investigated. Based on the above parametric studies the following can be concluded:

- Output shaft angle has a negligible effect on the DTEs and bearing forces. This is true for both amplitudes and natural frequencies.
- An increase in shaft length has mixed effects on the DTE, depending on the bearing stiffness value. On the other hand, a decrease in the shaft length results in an increase in bearing forces.
- Bearing stiffness increase causes an increase in bearing forces until a certain value of bearing stiffness. Further increase in bearing stiffness has no additional effect on bearing forces because the shaft stiffness becomes dominant.
- Gear pair positions have mixed effects on the DTE and bearing forces. DTE peak amplitudes are strongly dependent on gear pair positions. However, the peak bearing force amplitudes remain relatively independent of gear pair positions.

As presented above, several parameters have clear effects on the system's response. Conversely, the effect of the other parameters is not so evident. The approach developed in this thesis can be adopted and used to perform parametric studies during a preliminary design stage of simple gearbox systems. A number of gearbox configurations could be modelled and simulated assisting engineers with their final selection of the optimum gearbox layout. In addition, already existing gearbox systems with excessive noise and vibration levels can be modelled and analyzed helping reduce noise and vibration levels.

5.3 Future Work

The finite element model developed here could be extended to include flexible gear bodies, a non-linear bearing behaviour, and non-linear backlash effects. Models with flexible gear bodies have been developed and experimentally verified for single-stage spur gear reductions. No such experimentally verified model exists yet for multi-stage helical gear reductions according to the author's knowledge. Non-linear bearing models do exist, and their inclusion in the model would require the direct numerical integration solution technique. This is typically done in cases where the vibration through bearings and gearbox housings is of interest. For this purpose, an inclusion of flexible housing is also required and could be easily incorporated into the model developed here. Non-linear backlash effects would also have to employ the direct time integration solution technique.

References

- [1] ANSI/AGMA 2001-C95, *Fundamental rating factors and calculation methods for involute spur and helical gear teeth*, American Gear Manufacturers Association, 1995.
- [2] S. Adhikari, *Damping modelling using generalized proportional damping*, Journal of Sound and Vibration **293** (2006), 156–170.
- [3] W.J. Altenhof and N.G. Zamani, *Lecture Notes: Introduction to Finite Element Analysis*, FEA connection, Windsor, 2005.
- [4] A. Anderson and L. Vedmar, *A dynamic model to determine vibrations in involute helical gears*, Journal of Sound and Vibration **260** (2003), 195–212.
- [5] ANSYS, *User's Manual*, ANSYS, Inc., 2000.
- [6] S. Barone, L. Borgianni, and P. Forte, *Evaluation of the effect of misalignment and profile modification in face gear drive by a finite element meshing simulation*, ASME **126** (2004), 916–924.
- [7] S. Baud and P. Velex, *Static and dynamic tooth loading in spur and geared systems-experiments and model validation*, Journal of Mechanical Design **124** (2002), 334–346.
- [8] C.F. Beards, *Structural Vibration: Analysis and Damping*, Elsevier, 1996.
- [9] R.G. Budynas, C.R. Mischke, and J.E. Shigley, *Mechanical Engineering Design*, 7th edition, McGraw-Hill, New York, 2004.
- [10] T.K. Caughey and M.E.J. O'Kelly, *Classical normal modes in damped linear dynamic systems*, Journal of Applied Mechanics **32** (1965), 583–588.
- [11] Y-C. Chen and C-B. Tsay, *Contact ratios and transmission errors of a helical gear set with involute teeth pinion and modified circular arc teeth gear*, JSME International Journal **44** (2001), 867–874.

- [12] S.H. Choi, J. Glienicke, D.C. Han, and K. Ulrichs, *Dynamic gear loads due to coupled lateral, torsional and axial vibrations in a helical geared system*, Journal of Vibration and Acoustics **121** (1999), 141–148.
- [13] P.D. Dudley, *Dudley's Gear Handbook*, 2nd edition, McGraw-Hill, New York, 1968.
- [14] D.J. Ewins, *Modal Testing: Theory and Practice*, Research Studies Press Ltd., England, 1984.
- [15] A. Kahraman, K. Kienzle, M. Kubur, and D.M. Zini, *Dynamic analysis of a multi-shaft helical gear transmission by finite elements: Model and experiment*, Journal of Vibration and Acoustics **126** (2004), 398–406.
- [16] A. Kahraman, H.N. Ozguven, D.R. Houser, and J.J. Zakrajsek, *Dynamic analysis of geared rotors by finite elements*, Journal of Mechanical Design **114** (1992), 507–514.
- [17] A. Kahraman and P. Wagaj, *Influence of tooth profile modification on helical gear durability*, ASME **124** (2002), 501–510.
- [18] F.L. Litvin, J. Lu, D.P. Townsend, and M. Howkins, *Computerized simulation of meshing of conventional helical involute gears and modification of geometry*, Mechanism and Machine Theory **34** (1999), 123–147.
- [19] L. Liu and D.J. Pines, *The influence of gear design parameters on gear tooth damage detection sensitivity*, ASME **124** (2002), 794–804.
- [20] B.N. Norden, *On the compression of a cylinder in contact with a plane surface*, National Bureau of Standards **73-243** (1973).
- [21] H.N. Ozguven and D.R. Houser, *Mathematical models used in gear dynamics—a review*, Journal of Sound and Vibration **121** (1988), 383–411.
- [22] A. Parey and N. Tandon, *Spur gear dynamic models including defects: A review*, The Shock and Vibration Digest **35** (2003), 465–478.
- [23] S-J. Park and W-S. Yoo, *Deformation overlap in the design of spur and helical gear pair*, Finite Elements in Analysis and Design **40** (2004), 1361–1378.
- [24] J. Peeters, P. Sas, and D. Vandepitte, *Flexible multi-body model of a three stage planetary gearbox in a wind turbine*, ISMA (2004), 3923–3942.

- [25] J.S. Przemieniecki, *Theory of Matrix Structural Analysis*, McGraw-Hill, New York, 1968.
- [26] R. Singh and H. Vinayak, *Multi-body dynamics and modal analysis of compliant gear bodies*, Journal of Sound and Vibration **210**(2) (1998), 171–214.
- [27] S. Sirichai, *Torsional Properties of Spur Gears in Mesh using Nonlinear Finite Element Analysis*, Ph.D. thesis, Curtin University of Technology, 1999.
- [28] B.H. Tongue, *Principles of Vibration*, 2nd edition, Oxford University Press, New York, 2002.
- [29] J. Wang, *Numerical and Experimental Analysis of Spur Gears in Mesh*, Ph.D. thesis, Curtin University of Technology, 2003.
- [30] Y. Wang and I. Howard, *Finite element analysis of high contact ratio spur gears in mesh*, Journal of Tribology **127** (2005), 469–483.
- [31] Z. Wei, *Stresses and Deformations in Involute Spur Gears by Finite Element Method*, Master's thesis, University of Saskatchewan, 2004.

Appendix A

Involute Profile and Helix Macro ANSYS Code

```
/COM,*****
/COM,                INVOLUTE PINION PROFILE
/COM,*****

n=30                !Pinion number of teeth
m=2                 !Transverse module
w=15                !Face width
pa=20               !Transverse pressure angle
hangle=15           !Helix angle

/prep7
*afun,rad
pi=acos(-1)
x1=0
fi=pa*pi/180
g1=0.25
a1=1
nu=150
nu1=150
u=-(pi/4+(a1-g1)*tan(fi)+g1/cos(fi))
v=g1-a1
thmin=(u+(v+x1)/tan(fi))*2/n
thmax=((2+n+2*x1)**2-(n*cos(fi))**2)**0.5/(n*cos(fi))-(1+2*x1/n)*tan(fi)-pi/(2*n)
inc=(thmax-thmin)/nu
```



```

*do,i,1,(nu+1)
th=thmin+inc*(i-1)
x=(n*m/2)*(sin(th)-((th+pi/(2*n))*cos(fi)+(2*x1*sin(fi))/n)*cos(th+fi))
y=(n*m/2)*(cos(th)+((th+pi/(2*n))*cos(fi)+(2*x1*sin(fi))/n)*sin(th+fi))
k, ,x,y,,
*enddo

thmax2=2*u/n
inc=abs(thmax2-thmin)/nu1
*do,i,1,(nu1+1)
*if,i,eq,nu1+1,*exit
th=thmin+inc*(i-1) labc=(1+4*(((v+x1)/(2*u-n*th))**2))**0.5
pq=(g1/labc)+(u-n*th/2)
qp=2*(g1/labc)*(v+x1)/(2*u-n*th)+v+(n/2)+x1
x=m*(pq*cos(th)+qp*sin(th))
y=m*(-pq*sin(th)+qp*cos(th))
k, ,x,y,,
*enddo

finish

```

```

/COM,*****
/COM,                LEFT HAND HELIX CURVE
/COM,*****

/prep7
HA=Hangle*pi/180
radius=(m*n)/2
pitch=pi*radius*2*(1/tan(HA))
ncoils=0.25
tlen=pitch*ncoils
r=radius
p=pitch
n=ncoils
csys,0
pi=acos(-1)
*do,i,1,(4*n),1
csys,0
kpno=i+1000
x1=r*sin((i-1)*(pi/2))
y1=r*cos((i-1)*(pi/2))
z1=tlen*((i-1)/(4*n))
k,kpno,x1,y1,z1
x2=r*sin((i)*(pi/2))
y2=r*cos((i)*(pi/2))
z2=tlen*((i)/(4*n))
k,kpno+1,x2,y2,z2
csys,1
l,(i+1000),(i+1+1000)
*enddo
csys,0
wpave,0,0,w
wpstyle,,,,,,,,0
lsbw,1
finish

```

Appendix B

Beam Element Stiffness Matrix

$$[k_s] = \begin{bmatrix} \frac{12EI_y}{l^3(1+\phi_x)} & 0 & 0 & 0 & -\frac{6EI_y}{l^2(1+\phi_x)} & 0 & -\frac{12EI_y}{l^3(1+\phi_x)} & 0 & 0 & 0 & -\frac{6EI_y}{l^2(1+\phi_x)} & 0 \\ 0 & \frac{12EI_x}{l^3(1+\phi_y)} & 0 & \frac{6EI_x}{l^2(1+\phi_y)} & 0 & 0 & 0 & 0 & 0 & 0 & \frac{6EI_x}{l^2(1+\phi_y)} & 0 \\ 0 & 0 & \frac{EA}{l} & 0 & 0 & 0 & 0 & 0 & -\frac{EA}{l} & 0 & 0 & 0 \\ 0 & \frac{6EI_x}{l^2(1+\phi_y)} & 0 & \frac{(4+\phi_y)EI_x}{l(1+\phi_y)} & 0 & 0 & 0 & 0 & -\frac{6EI_x}{l^2(1+\phi_y)} & 0 & \frac{(2-\phi_y)EI_x}{l(1+\phi_y)} & 0 \\ -\frac{6EI_y}{l^2(1+\phi_x)} & 0 & 0 & 0 & \frac{(4+\phi_x)EI_y}{l(1+\phi_x)} & 0 & \frac{6EI_y}{l^2(1+\phi_x)} & 0 & 0 & 0 & \frac{(2-\phi_x)EI_y}{l(1+\phi_x)} & 0 \\ 0 & 0 & 0 & 0 & 0 & \frac{GJ}{l} & 0 & 0 & 0 & 0 & 0 & -\frac{GJ}{l} \\ -\frac{12EI_y}{l^3(1+\phi_x)} & 0 & 0 & 0 & \frac{6EI_y}{l^2(1+\phi_x)} & 0 & \frac{12EI_y}{l^3(1+\phi_x)} & 0 & 0 & 0 & \frac{6EI_y}{l^2(1+\phi_x)} & 0 \\ 0 & -\frac{12EI_x}{l^3(1+\phi_y)} & 0 & -\frac{6EI_x}{l^2(1+\phi_y)} & 0 & 0 & 0 & 0 & \frac{12EI_x}{l^3(1+\phi_y)} & 0 & -\frac{6EI_x}{l^2(1+\phi_y)} & 0 \\ 0 & 0 & -\frac{EA}{l} & 0 & 0 & 0 & 0 & \frac{EA}{l} & 0 & 0 & 0 & 0 \\ 0 & \frac{6EI_x}{l^2(1+\phi_y)} & 0 & \frac{(2-\phi_y)EI_x}{l(1+\phi_y)} & 0 & 0 & 0 & 0 & -\frac{6EI_x}{l^2(1+\phi_y)} & 0 & \frac{(4+\phi_y)EI_x}{l(1+\phi_y)} & 0 \\ -\frac{6EI_y}{l^2(1+\phi_x)} & 0 & 0 & 0 & \frac{(2-\phi_x)EI_y}{l(1+\phi_x)} & 0 & \frac{6EI_y}{l^2(1+\phi_x)} & 0 & 0 & 0 & \frac{(4+\phi_x)EI_y}{l(1+\phi_x)} & 0 \\ 0 & 0 & 0 & 0 & 0 & -\frac{GJ}{l} & 0 & 0 & 0 & 0 & 0 & \frac{GJ}{l} \end{bmatrix}$$

Vita Auctoris

Siniša Drača was born in 1978 in Rijeka, Yugoslavia. He graduated from Nikola Tesla High School in Belgrade, Yugoslavia in 1996. From there he went on to St. Clair College in Windsor, Ontario where he obtained a Mechanical Engineering Technology Diploma/Mould, Tool and Die Design Option in 2001. Soon after, he attended the University of Windsor where he obtained B.A.Sc. in Mechanical Engineering/Automotive Option in 2004. He is currently a candidate for the Master's degree in Mechanical Engineering at the University of Windsor and hopes to graduate in the Summer of 2006.